

1-1-2014

High-Performance Accelerometer Based On Asymmetric Gapped Cantilevers For Physiological Acoustic Sensing

Yating Hu
Wayne State University,

Follow this and additional works at: http://digitalcommons.wayne.edu/oa_dissertations

 Part of the [Biomedical Engineering and Bioengineering Commons](#), [Electrical and Computer Engineering Commons](#), and the [Mechanical Engineering Commons](#)

Recommended Citation

Hu, Yating, "High-Performance Accelerometer Based On Asymmetric Gapped Cantilevers For Physiological Acoustic Sensing" (2014). *Wayne State University Dissertations*. Paper 988.

**HIGH-PERFORMANCE ACCELEROMETER BASED ON ASYMMETRIC GAPPED
CANTILEVERS FOR PHYSIOLOGICAL ACOUSTIC SENSING**

by

YATING HU

DISSERTATION

Submitted to the Graduate School

of Wayne State University,

Detroit, Michigan

in partial fulfillment of the requirements

for the degree of

DOCTOR OF PHILOSOPHY

2014

MAJOR: ELECTRICAL ENGINEERING

Approved by

Adviser

Date

© COPYRIGHT BY
YATING HU
2014
ALL RIGHTS RESERVED

ACKNOWLEDGMENTS

Above all, I would like to express my great appreciation to my advisor Dr. Yong Xu. Beyond receiving excellent academic guidance from him, I am also deeply influenced by his personal integrity and expectations of excellence. Along the years, he serves as a role model for me as a researcher and educator, and inspires me on pursuing an academic career after graduation.

I would also like to express my sincere gratitude to other members of the dissertation committee, Dr. Mark Cheng, Dr. Amar Basu and Dr. Chin-an Tan for their support, guidance and helpful suggestions.

My sincere thanks also goes to my fellow labmates Dr. Qinglong Zheng for his help on the analytical model derivation; Hongen Tu for his help on prototype machining and assembling; Eric Kim for his help on explaining the mechanism of the physiological acoustics. Another special thanks goes to my collaborators Dr. Phillip Levy and his group members for their help on the arranging clinical tests of the heart sensors I developed.

I am forever indebted to my parents Wei Liu / Jingrun Hu. Their unwavering faith and confidence in me is what has shaped me to be the person I am today.

Finally, I thank the national science foundation for their generous support and Wayne State University for providing the facility to carry out my research.

TABLE OF CONTENTS

ACKNOWLEDGMENTS.....	II
LIST OF TABLES.....	VII
LIST OF FIGURES.....	VIII
CHAPTER 1 INTRODUCTION.....	1
1.1 MOTIVATION.....	1
1.2 OBJECTIVE.....	3
1.3 THESIS ORGANIZATION.....	5
CHAPTER 2 PIEZOELECTRIC ACCELEROMETER.....	7
2.1 INTRODUCTION.....	7
2.1.1 <i>Specifications of accelerometers.....</i>	<i>7</i>
2.1.2 <i>Accelerometers for physiological acoustic sensing.....</i>	<i>9</i>
2.2 DESIGN.....	20
2.2.1 <i>Asymmetric-gapped cantilevers structure.....</i>	<i>20</i>
2.2.2 <i>Energy aspect.....</i>	<i>25</i>
2.3 FEA SIMULATION.....	29
2.3.1 <i>Introduction.....</i>	<i>29</i>
2.3.2 <i>Model verification.....</i>	<i>30</i>
2.4 NOISE.....	32
2.4.1 <i>2.4.1 Thermal-mechanical noise.....</i>	<i>32</i>
2.4.2 <i>2.4.2 Thermal-electrical noise.....</i>	<i>34</i>
2.4.3 <i>Total noise.....</i>	<i>35</i>
2.5 READOUT CIRCUIT.....	37

2.5.1	<i>Voltage amplifier</i>	38
2.5.2	<i>Charge amplifier</i>	39
2.5.3	<i>Comparison of the lower cutoff frequency</i>	41
2.6	SUMMARY.....	42
CHAPTER 3 CONTINUOUS CARDIO-RESPIRATORY SOUND MONITORING		44
3.1	INTRODUCTION	44
3.1.1	<i>Heart sound</i>	44
3.1.2	<i>Fetal monitoring</i>	46
3.1.3	<i>Respiratory sound</i>	47
3.1.4	<i>Technology review</i>	49
3.1.5	<i>Challenges and prospect</i>	51
3.2	DESIGN	53
3.2.1	<i>Structure</i>	53
3.2.2	<i>FEA simulation</i>	54
3.3	CHARACTERIZATION	55
3.3.1	<i>Signal processing circuit</i>	57
3.3.2	<i>3.3.2 Resonant frequency</i>	60
3.3.3	<i>Sensitivity</i>	61
3.3.4	<i>Noise</i>	62
3.4	PRELIMINARY TESTS.....	67
3.5	SUMMARY.....	73
CHAPTER 4 LOW FREQUENCY VIBRATION SENSING AND BCG MONITORING		75
4.1	INTRODUCTION	75
4.1.1	<i>Ballistocardiograph (BCG) monitoring</i>	75

4.1.2	<i>Seismic monitoring</i>	76
4.2	DESIGN	77
4.2.1	<i>Structure</i>	77
4.2.2	<i>FEA simulation</i>	79
4.3	CHARACTERIZATION	81
4.3.1	<i>Resonant frequency and sensitivity</i>	82
4.3.2	<i>Noise</i>	84
4.4	PRELIMINARY TESTS	87
4.5	CONCLUSION	90
CHAPTER 5 A WIDEBAND VIBRATION ENERGY HARVESTER BASED ON A FOLDED ASYMMETRIC-GAPPED CANTILEVER		91
5.1	INTRODUCTION	91
5.2	DESIGN	94
5.2.1	<i>Structure</i>	94
5.2.2	<i>FEA simulation</i>	96
5.3	CHARACTORIZATION	100
5.4	PRELIMINARY TESTS	102
5.5	CONCLUSION	105
CHAPTER 6 FUTURE WORK		107
6.1	PIEZORELECTRIC ACCELEROMETER	107
6.2	CARDIO-RESPIRATORY SOUND MONITORING	107
6.3	BCG MONITORING AND SEISMIC SENSING	108
6.4	VIBRATION ENEGY HARVESTING	108
6.5	OTHER APPLICATIONS	109

REFERENCE	110
ABSTRACT	132
AUTOBIOGRAPHICAL STATEMENT.....	133

LIST OF TABLES

Table 2.1 Summary of commonly used MEMS accelerometers for physiological acoustic sensing.	14
Table 2.2 Summary of conventional large-size accelerometers for physiological acoustic sensing.	17
Table 2.3 The simulation flow chart.....	30
Table 2.4 Design parameters of the asymmetric gapped cantilever	31
Table 2.5 Analytical and simulation results for both ideal and real cases.....	31
Table 2.6 Geometric properties of bottom beam, top beam and proof mass for four-stage cascaded asymmetric-gapped cantilever.	36
Table 2.7 calculated noise level of the cascaded asymmetric-gapped cantilever in Table 2.6.	37
Table 3.1 Geometric and material properties of bottom beam, top beam and proof mass of the asymmetric-gapped cantilever.....	54
Table 3.2 Analytical and simulation results for both ideal and real cases.....	54
Table 4.1 The prototype design parameters.....	79
Table 5.1 Parameters of the three-stage folded asymmetric-gapped cantilever structure investigated in this paper.	95

LIST OF FIGURES

Figure 2.1 Comparison of the (a) conventional accelerometer (h is the cantilever thickness) and (b) new accelerometer design based on decoupled piezoelectric layer (asymmetric gapped cantilever).	21
Figure 2.2 Forces and bending moments applied to the cantilever. F_{n1} , F_{n2} , F_1 , F_2 , M_1 and M_2 are normal forces, shear forces and bending moments on bottom and top beams respectively, F is the force on proof mass in z direction, and D is the distance between top and bottom beams.	22
Figure 2.3 Two deformation modes of the asymmetrically-gapped cantilever.	23
Figure 2.4 Plot of efficiency η as a function of γ with different C ($\alpha = 11$)[86]	28
Figure 2.5 A cantilever structure based piezoelectric accelerometer could be modeled as a damped harmonic oscillator with a spring constant k , mass M and damping ratio r	33
Figure 2.6 The equivalent circuit of piezoelectric material	34
Figure 2.7 Input voltage noise spectral density of TI OPA129	37
Figure 2.8 Voltage amplifier mode circuit model	38
Figure 2.9 Charge amplifier mode circuit model	40
Figure 3.1 A schematic drawing of the operating principle of the stethoscope after [92]	50
Figure 3.2 The packaged device was mounted on a mechanical shaker. A commercial accelerometer was used to calibrate the acceleration.	56
Figure 3.3 Prototype compared with a penny	57
Figure 3.4 (a) Amplifier circuit design (b) Inside view of the prototype with the PCB board on the proof mass	60

Figure 3.5 Frequency response of the accelerometer under 1 g acceleration. A resonant frequency of 1100Hz and a quality factor of 80 were measured.....	60
Figure 3.6 Sensor positioned in x, y, z three directions.....	62
Figure 3.7 Noise in different environment (a) in lab; (b) in acoustic isolation room, sensor placed on chair; (c) in acoustic isolation room, sensor suspended in air.....	65
Figure 3.8 Airborne noise tested in the environment with 700Hz noise generated by speaker. The sensor is placed (a) on the table; (b) suspended in air	66
Figure 3.9 Sample waveforms of heart sound: (a) detected by our new accelerometer; (b) detected by an electronic stethoscope.....	69
Figure 3.10 Sample waveforms of lung sound: (a) detected by our new accelerometer; (b) detected by an electronic stethoscope.....	71
Figure 3.11 Sample waveforms of heart sounds of heart failure patient: (a) before treatment; (b) after treatment.....	73
Figure 4.1 Schematic of a low-frequency accelerometer based on a four-stage cascaded asymmetric-gapped cantilever structure.....	78
Figure 4.2 (a) The first resonant mode of a four-stage cascaded asymmetric-gapped cantilever; (b) the first resonant mode of single stage asymmetric-gapped cantilever; (c) the second and third resonant modes of the cascaded asymmetric-gapped cantilever.	81
Figure 4.3 Prototype device mounted on a shaker together with the reference accelerometer	83
Figure 4.4 Frequency response of the designed accelerometer.....	84
Figure 4.5 (a). Noise equivalent acceleration of the designed accelerometer. The initial measured NEA, the NEA scaled by the coherence and the theoretical noise floor are plotted for comparison. (b) Coherence between the two piezoelectric sensing beams.....	87
Figure 4.6 (a) A representative portion of the experimental BCG signal acquired by the low-frequency vibration sensor; (b) The corresponding heart sound signal with first heart sound (S1) and second heart sound (S2) denoted; (c) One BCG cycle was enlarged to show the details of the	

signal and compared with a theoretical BCG signal. The extrema of the BCG waveform are denoted with letters F, G, H, I, J, K, L, M and N.	89
Figure 5.1 Simulation of the bending mode and strain distribution of the PEH model in paper [181] (Figure 4). (a) Top view of the second resonant mode; (b) Side view of the second resonant mode.	93
Figure 5.2 Schematic of the wideband VEH based on a three-stage folded asymmetric-gapped cantilever structure	96
Figure 5.3 The simulation results of the first three resonant modes of the three-stage folded asymmetric gapped structure: (a) the first resonant mode; (b) the second resonant mode; and (c) the third resonant mode.	100
Figure 5.4 Frequency responses of the three stages of the folded cascaded structure.	102
Figure 5.5 The VEH prototype mounted on the ceiling air conditioning unit.....	103
Figure 5.6 The vibration spectrum of the ceiling air conditioning unit.....	104
Figure 5.7 The output voltage of a 2200 μ F capacitor charged by the prototype VEH under the vibration of a ceiling air conditioning unit. The inset plots representative output voltages of the piezoelectric layers in stages I, II and III before rectification.	105

CHAPTER 1 INTRODUCTION

1.1 Motivation

Accelerometers are extensively used in a wide range of markets such as military, industrial, energy, transportation and healthcare[1-3]. In industry, monitoring and controlling vibration in rotating machinery could decrease the unscheduled downtime, increase profit and prevent potential safety threaten accident. In mobile healthcare, accelerometers have been widely used for activity monitoring, posture detection, and fall detection for elderly people [4]. This thesis is particularly focused on the sensing of physiological acoustic signals on human body using accelerometers. The physiological acoustic signals include, but are not limited to, heart sounds, respiratory sounds and gastrointestinal sounds, which contain a rich reservoir of vital physiological and pathological information. Continuous or mobile monitoring of physiological sounds is expected to play important role in the emerging mobile healthcare field.

Because of its miniature size, easy installation and good response especially to high frequency vibrations[5, 6], accelerometer is an excellent choice for continuous physiological acoustic signal monitoring. Since its invention, numerous efforts have been spent on improving the performance of the accelerometer. Most accelerometers can be modeled as a spring-mass system[7]. Cantilever-based accelerometer, in which a cantilever functions as the spring, is one of the most widely used configurations due to its simplicity. When experiencing an acceleration, the seismic mass exerts a force on the sensing materials through the bending of the cantilever structure and converted to a measurable electrical signal. There are different types of sensing

materials such as piezoresistive and piezoelectric materials. Because the piezoelectric materials has many desired properties such as exceptional linearity, broad frequency range, high mechanical stiffness and unidirectional sensitivity[8, 9], we will focus on the piezoelectric cantilever based accelerometer in this thesis.

For the physiological acoustic signal measurement applications, there are more demanding requirements on the sensitivity/noise performance of accelerometers. While many improvements have been made on piezoelectric accelerometers, most of them employ a simple conventional cantilever structure by placing the piezoelectric layer close to the base and on the surface of the cantilever beam. As explained in Chapter 2, since the sensitivity is proportional to the distance between the neutral plane and the sensing layer, the conventional structure limits the sensitivity and resolution which makes it challenging to be used in many applications requiring high resolution. In this thesis, we present a unique piezoelectric accelerometer based on the asymmetric-gapped cantilever structure which exhibits significantly improved sensitivity. It comprises a top piezoelectric layer and a bottom mechanical layer. It is worth noting that the normal strain experienced by the piezoelectric layer is proportional to the distance between this layer and the neutral plane. For asymmetric-gapped cantilever, this distance could be much larger than it of the conventional cantilever as explained in Chapter 2. Thus, both the displacement and force sensitivity of the asymmetric-gapped cantilever could be improved by orders of magnitude compared with conventional ones with the same spring constant and length.

Because it is hard to design an optimized asymmetric-gapped cantilever with low resonant frequency, the cascaded structure based on the basic gapped cantilever is developed for low frequency sensing application such as seismometer and ballistocardiogram (BCG) monitor

as discussed in Chapter 4. Ridges are added to separate the original gapped beams into several stages and eliminated the undesired shear bending mode to achieve high sensitivity. In the experiment, a prototype was mounted at the bottom side of an office chair and successfully acquired high quality BCG data generated by the person sat on the chair.

Furthermore, from the energy perspective, the asymmetric gapped cantilever is also a more efficient design. For the conventional cantilever structure, even with optimization, only less than 37% of the bending energy is applied on the piezoelectric layer and contributes to the output signal [10]. The majority of mechanical energy can be concentrated on the piezoelectric layer, and the overall energy conversion efficiency can reach about 90%[11]. Therefore, it could also be used for designing high efficiency vibration energy harvester as explained in Chapter 5. What's more, in order to achieve a wide band energy harvesting ability, a folded gapped cantilever is designed to enable multiple resonant modes, which are dominated by pure bending of all stages, in a relative narrow bandwidth. The prototype is mounted on a ceiling air condition unit to harvesting the machinery vibration for the proof of concept test.

1.2 Objective

The asymmetric-gapped cantilever structure could significantly improve the performance for piezoelectric accelerometer. Therefore, the advantage of the structure is summarized in the thesis. A fully investigation of utilizing the designed sensor for cardio-respiratory sound monitoring is carried out. A prove of concept prototype is being tested to identify irregular heart sound of the heart failure patient in the hospital settings. Moreover, with improved cascaded structure developed particularly for low frequency sensing applications, the

sensor is able to detect physiological acoustic signal with much lower frequency components such as BCG signal. Last, the asymmetric gapped cantilever hold great potential for vibration energy harvesting because of its high energy conversion ratio. Therefore, folded gapped structure is developed to address the needs of harvesting vibration energy across a wide bandwidth.

The main objectives of this work are:

1. To investigate the advantage of utilizing the asymmetric-gapped cantilever for piezoelectric accelerometer.
2. To implement the gapped cantilever for cardio-respiratory sound monitoring and identify irregular heart sound in heart failure patient with proper signal processing techniques.
3. To investigate the advantage of utilizing the cascaded gapped cantilever for low frequency vibration sensing, and implement it for BCG measurement and characterization.
4. To investigate the advantage of utilizing the folded gapped cantilever for wide band vibration energy harvesting, and implement it for harvesting machinery vibration energy from ceiling air-condition unit.

1.3 Thesis Organization

In chapter 2, the basic design factors of piezoelectric accelerometer including piezoelectric materials selection, intrinsic noise, readout circuit, etc. are presented. The advantage of the asymmetric-gapped cantilever and the involved cascaded and folded structures are also discussed and summarized in chapter 2.

In the chapter 3 and 4, two specific applications utilizing the piezoelectric accelerometer based on the asymmetric-gapped cantilever are presented. In chapter 3, accelerometer used for continuous cardio-respiratory sound monitoring is designed. Preliminary tests are carried out on healthy individuals to verify the feasibility of the sensor. And further experiment is designed to utilize it on heart failure patient monitoring to identify irregular heart sound changing through treatment. In chapter 4, the accelerometer based on the cascaded structure for low frequency physiological acoustic sensing is designed. The prototype which is attached to the bottom of an office chair has successfully acquired BCG signal of the subject sitting on chair.

Chapter 5 utilizes the high energy conversion efficiency characteristic of asymmetric gapped cantilever for vibration energy harvester design. Furthermore, to enhance the vibration energy harvester's performance over a wide bandwidth, a folded gapped structure is developed to enable multiple vibration modes within a relative narrow frequency band. Finally, the designed energy harvester is utilized on an air condition unit for harvesting machinery vibration.

Chapter 6 summarizes the main contributions of the dissertation and gives suggestions for the potential work in the future.

CHAPTER 2 PIEZOELECTRIC ACCELEROMETER

2.1 Introduction

Accelerometer is a mechanical sensing element that consists of a proof mass attached to a mechanical suspension system. The acceleration, which causes the displacement of the proof mass, can be measured through the change on the sensing element. Based on the difference on the sensing element, the accelerometer could be classified as piezoresistive, piezoelectric and differential capacitive types, etc. Among them, the piezoelectric accelerometer has been a popular choice[12-14]. When under stretching/compression, the piezoelectric material generates electrical charge on the surface, which converts the mechanical signal to electrical signal and vice versa. Piezoelectric accelerometers are widely used for a large variety of applications: medical, consumer electronics, industrial and military.

2.1.1 Specifications of accelerometers

When choosing accelerometers for physiological acoustic sensing, we mainly consider the following technical specifications:

1) Size and weight

To minimize the inconvenience and uncomfortableness of wearing or carrying, it is desirable to have miniaturized sensors that have small size and light weight. In this regard, MEMS accelerometers have an edge over conventional large-size ones. It needs to be cautioned that the printed circuit board that hosts the MEMS chip, readout circuits, and power source (i.e., battery) will significantly increase the overall size of the system. Furthermore, a small mass is not favorable for achieving high sensitivity.

2) Minimum detectable acceleration, noise and sensitivity

The heart sounds typically generate accelerations at milli-gravity (mg) level. However, some subtle components have much lower amplitude. Lung sounds are generally much weaker than heart sounds (e.g., 0.1 mg). Whether or not an accelerometer is able to detect these sounds is determined by a specification called minimum detectable acceleration a_{\min} . If we assume that an acceleration is detectable when it can generate a voltage larger than the noise of the accelerometer, then we have the following relationship:

$$a_{\min} = \text{Noise voltage}/\text{Sensitivity} \quad (2.1)$$

It can be observed that to detect small acceleration, a high sensitivity is required. However, the ultimate noise floor of the accelerometer is determined by the thermo-mechanical noise [15]. It can be observed that the smaller the proof mass, the larger the minimum detectable acceleration. Therefore, in terms of minimum detectable acceleration, miniaturization is not favorable. This is a challenge faced by MEMS accelerometers.

3) Bandwidth

The majority energy of heart sounds exists between 10-400 Hz. Ballistocardiography signals are typically below 20 Hz. Lung sounds are mainly between 60 Hz and 2000 Hz, but tracheal sounds can be well above 2 kHz [16]. To detect these signals, accelerometers need to have appropriate bandwidth accordingly. The upper end of the bandwidth is typically limited by the natural frequency of the accelerometer:

$$f_0 = \frac{1}{2\pi} \sqrt{\frac{k}{m}} \quad (2.2)$$

For piezoelectric accelerometers, there is also a lower limit of measurement bandwidth set by the RC time constant of the piezoelectric material and readout circuit. Therefore, special attention needs to be paid when choosing piezoelectric accelerometers to detect low frequency vibrations. There is a tradeoff between the bandwidth and the sensitivity of the accelerometer when the mass is fixed. Choosing an accelerometer with a much wider bandwidth than needed is not suggested since the sensitivity is not optimized.

In addition, mass loading [17, 18] and sensitivity to air-borne noise [19] may need to be considered when selecting accelerometers.

2.1.2 Accelerometers for physiological acoustic sensing

Accelerometers used for physiological acoustic sensing can be divided into two categories: miniaturized MEMS accelerometers and conventional large-size accelerometers. A large variety of MEMS accelerometers are commercially available now. As the technology advances, the cost of MEMS accelerometers is decreasing steadily. Their small size and light weight are highly desirable for mobile healthcare. However, their capability to detect very small vibration is limited. On the contrary, conventional accelerometers have high sensitivity but are not convenient for wearable applications due to their large size and heavy weight.

Compared with the ones for activity monitoring or posture detection, MEMS accelerometers for physiological acoustic sensing need to have much better sensitivity or noise performance. A number of high-performance MEMS accelerometers have been used for the detection of heart sounds which have relatively large amplitude.

Castiglioni et al. attached ST LIS3L02AL, a triaxial MEMS capacitive accelerometer from STMicroelectronics, on the left clavicle to record seismocardiogram (SCG), which can be considered as low-frequency component of heart sounds [20]. This group later integrated ST LIS3L02DL, which has digital output interfaces, into textiles to make a wearable device for SCG detection [21, 22]. The prototype developed is named the MagIC system which incorporates ECG and respiration detection as well. This MagIC garment has been used for the 24-hour measurement of SCG in ambulant subjects [23]. ST LIS3L02DL has been used by Bryant et al. to develop an accelerometer-based chest-worn heart monitoring system [24]. Pandia et al. used a ST LIS3L02AL accelerometer to detect heart sound and developed algorithm to cancel motion artifact [25]. A LIS3 accelerometer was also used by Bombardini et al. to derive diastolic times and the diastolic/systolic time ratio from first and second heart sounds [26].

Urbaszek et al. used CMA 3000-A0, a 3-axis MEMS capacitive accelerometer from VTI technologies (now Murata Electronics, Oy, Vantaa, Finland) to detect heart sounds of a sheep [27]. In their study, a pressure sensor was implanted into the pulmonary artery of the sheep to measure blood pressure. They claimed that heart sound signal, combined with the blood pressure information, improves valve opening/closure detection [27]. KXM52-1050, a 3-axis accelerometer from Kionix, was used to monitor the daily activities of elderly people [28]. The acquired signals include heart sounds, respiration, posture and acceleration due to other behaviors. Bosch BMA180, a triaxial MEMS accelerometer, has been used for BCG measurement on head [29]. Imtiaz et al. used a 3-axis MEMS accelerometer, MMA7260QT from Freescale, to measure low frequency vibrations caused by heart beat (Seismocardiogram) [30].

One commercial product for continuous heart sound monitoring is Audicor® system from Inovise Medical, Inc. (Portland, Oregon), which provides the capability of recording both heart sounds and ECG simultaneously [31]. Their heart sound sensors were originally based on microphones, but later changed to accelerometers (most likely MEMS accelerometers).

There are a number of studies in which MEMS accelerometers are used for sensing physiological acoustic sounds other than heart signals. MMA7455L from Freescale has been used for sleep apnea study [32]. Note that MMA 7455L has a low resolution and may not be able to detect weak sound signals. In [32] it was used to measure snoring sounds, which have large amplitude. Knowles BU-7135 has been studied for bioacoustics sensing [19]. Kistler 8302A, a capacitive MEMS accelerometer, has been used to record respiratory mechanomyographic signals on dogs [33]. Kistler 8302A seems to have the best noise performance among the MEMS accelerometers reviewed: 25 μg over 10-100 Hz. However, it also has the largest dimension: 18 mm \times 17 mm \times 5 mm.

As mentioned previously, the reduction of mass leads to larger minimum detectable acceleration. Therefore, it is challenging to use MEMS accelerometers to capture some subtle physiological sounds, such as heart murmur, third heart sound (S3), fourth heart sound (S4) and lung sounds, with a high signal-to-noise ratio. Therefore, off-the-shelf or custom-designed large-size piezoelectric accelerometers have been used by many researchers. Actually, before MEMS accelerometers are available, conventional accelerometers have long been used for physiological acoustic sensing.

Siemens EMT25C (Siemens), a piezoelectric accelerometer with a weight of 15.4 gram and a radius of 14 mm, has been extensively used for physiological sounds monitoring [16, 34-50]. PPG (phonopneumography) sensor, a piezoelectric accelerometer developed by Technion Israel, is another popular choice for sensing lung sounds [51-59]. In addition, HP 21050 (Hewlett-Packard), with a weight of 52.2 gram and radius of 7 mm, has been used by many researchers to record heart, lung, and muscle sounds [60-65]. However, HP 21050 is a displacement sensor, not accelerometer.

Pasterkamp et al. compared the relative performance of four accelerometers for lung sound recording: HP 21050, Siemens EMT25C, PPG 201 sensor, and FYSPac2 (University of Brussels, Belgium) with three air-coupled microphones [66]. They found that accelerometers have similar maximum signal-to-noise ratio compared to air-coupled microphones, but have better performance at higher frequencies. Later, Siemens EMT25C accelerometer and PPG 201 accelerometer have been studied for lung sound recording using a bioacoustic transducer testing system [67]. It was found that PPG sensor has a broader bandwidth extending to 4000 Hz. Suzuki et al. also characterized three commercially available accelerometers for lung sound recording on the chest: B&K 4393, HP 21050, and Siemens EMT25C [68]. B&K 4393 is a miniaturized accelerometer with a weight of only 2.4 gram. However, it also has a low sensitivity of 4.8 mV/g.

Model 393C piezoelectric accelerometer from PCB Piezotronics was used to measure low-frequency cardiac vibrations, or seismocardiogram [69-72]. This accelerometer has a sensitivity of 1000 mV/g and a resolution of 0.1 mg over a bandwidth from 1 to 10000 Hz. However, it has a weight of 885 gram and a dimension of 57.2 mm (diameter) × 54.9 mm (height), not

appropriate for wearable applications. Brüel & Kjær 4381 piezoelectric accelerometer has been used to measure BCG on an ultralow frequency bed pendulum [73]. B&K 4381 has a weight of 43 gram and a dimension of 21 mm (diameter) × 23.5 mm (height). The noise is 0.02 mg over 0.1 Hz – 4800 Hz.

Rendon et al. used Endevco 752A12, a commercially available general purpose piezoelectric, to map vibrations on the neck and thorax caused by heart beats, breathing and snoring [74]. Endevco 752A12 has also been used by Morillo et al. to record heart sounds and respiratory sounds for sleep apnea screening [75]. Endevco 752A12 has excellent noise performance: <150 µg over 1-10 kHz bandwidth. It has a height of 23.6 mm and a weight of 13 gram. Endevco 752A12 is much lighter and smaller than PCB 393C. However, it is still not convenient for wearable applications.

Prisk et al. reported measurement of BCG in spaceflight using a MMA triaxial accelerometer (ERNO Raumfahrttechnik/Deutsche Aerospace) [76]. This accelerometer was specifically designed for space application and has a weight of 165 gram.

In addition to piezoelectric sensors, piezoresistive accelerometers have also been used. For instance, a 1971 paper reports the use of a “pixie” accelerometer (Endevco Ltd) based on semiconductor strain gauges for the detection of infant heart sounds [77]. However, piezoresistive accelerometers are generally not as sensitive as piezoelectric ones.

There are also a number of efforts at universities to develop custom-designed accelerometers for heart or lung sounds recording. FYSPac2 characterized by Pasterkamp et al. [66] was developed at the Laboratory of Physiology and Physiopathology, University of Brussels, VUB [17]. FYSPac2 has been used to study sound transmission in respiratory system [78]. In early

90's, Padmanabhan et al. developed a piezoelectric accelerometer for heart sound detection based on a dual-cantilever structure [79]. The accelerometer they developed weighed approximately 5 gram and had a resonant frequency around 1.1 kHz. The theoretical sensitivity is 125 mV/g. The developed sensors have been used to detect sounds caused by turbulent blood flow in coronary arteries with stenosis.

While the currently available accelerometers could meet the demand of most applications, it is still challenging to use them for physiological acoustic sensing where the acceleration is very small and ultra high sensitivity and resolution sensor is required. In my work, a high performance piezoelectric accelerometer based on an asymmetric-gapped structure is developed [80]. Even though similar structure is developed in some previous work, no systematically study has been done to optimize and utilize it to develop high sensitivity piezoelectric accelerometer[81]. For a prototype accelerometer developed for targeting lung and heart sound monitoring, it has a dimension of 35mm×18mm×7.8mm and a weight of 5 gram. Its resonant frequency is 1100 Hz and reaches a noise floor of 40 ng/√Hz above 200 Hz. Currently, the noise is dominated by the amplifier noise. By optimizing the design, the performance can be further improved.

Commonly used accelerometers for physiological acoustic sensing are summarized in Table 2.1 and Table 2.2. Note that some accelerometers, which are discontinued or lack of specifications, are not included in the tables.

Table 2.1 Summary of commonly used MEMS accelerometers for physiological acoustic sensing.

Accelerometer	Dimension	bandwidth	Noise	Applications

	and weight			
Bosch BMA180, Triaxial, switchable ranges and bandwidths	3 mm × 3 mm × 0.9 mm	10/20/40/75/15 0/300/600/1200 Hz	0.69 mg resolution over 10 Hz bandwidth with 2 g measurement range	BCG measurement on head[29]
Freescall MMA7260QT,	6 mm × 6 mm × 1.45 mm	(f_{-3dB}): 350 Hz (XY), 150 Hz (Z);	350 $\mu\text{g}/\sqrt{\text{Hz}}$ for 1.5 g measurement range	Measurement of Seismocardiogram [30]
Freescall MMA7455L, 3- axis, Digital Output Accelerometer	3 mm × 5 mm × 1 mm	62.5 or 125 Hz	15.6 mg (based on the sensitivity 64 counts/g)	Sleep apnea study [32]
STMicroelectro nics LIS3L02AL, triaxial MEMS capacitive	5 mm × 5 mm × 1.6 mm; 0.08 gram;	1.5 kHz	50 $\mu\text{g}/\sqrt{\text{Hz}}$ for 2 g measurement range	Heart sound, Seismocardiograph y and BCG detection [25] [20] [26]

accelerometer				
STMicroelectronics LIS3LV02DL, a triaxial MEMS capacitive accelerometer with digital output	4.4 mm × 7.5mm × 1mm;	10/40/160/840 Hz;	1.0/2.0/3.9/15.6 mg	Continuous measurement of SCG in ambulant subject for 24 hours [23].
VTI technologies (now Murata Electronics) CMA 3000-A01, 3-axis MEMS capacitive accelerometer	2 mm × 2 mm × 0.95 mm	200 Hz (Y axis)	300 µg/√Hz;	Heart sound detection at the chest of a sheep [27, 82]
Kionix, KXM52-1050 3-axis	dimension: 5×5×1.8m	(-3dB): 0-3000 Hz (x and y), 0-1500 Hz (z)	35 µg/√Hz (x and y) and 65 µg/√Hz	daily monitoring (including heart sounds) for solitary

accelerometer	m		(z) at 500 Hz	elderly people [28]
Kistler 8302A (2S1/10S1/20S1) Single axis capacitive accelerometer	Dimension: 18 mm × 17 mm ×5 mm; weight: 2.8 gram;	bandwidth (±5%): 0- 400/1000/1000 Hz;	(10-100 Hz): 25/125/250 μg	Respiratory Mechanomyographic Signals recording [33]

Table 2.2 Summary of conventional large-size accelerometers for physiological acoustic sensing.

Accelerometer	Dimension and weight	Bandwidth	Noise/Sensitivity	Applications
Brüel & Kjær 4381 piezoelectric accelerometer	21 mm (diameter) × 23.5 mm (height); Weight: 43 gram;	0.1-4800 Hz	0.02 mg over the bandwidth Sensitivity: 80 mV/g	BCG measurement on an ultralow frequency bed pendulum [73].

B&K 4393 piezoelectric accelerometer	diameter: 7.5 mm; height: 11 mm; Weight: 2.4 gram;	($\pm 10\%$ amplitude response): 0.1 Hz 16500 Hz.	Sensitivity: 4.8 mV/g	Lung sound recording [68]
Custom-designed accelerometer based on piezoelectric double-cantilever structure	Weight: 5 gram	resonant frequency: ~ 1.1 kHz	theoretical sensitivity: 125 mV/g	Detecting sounds of turbulent blood flow in partially occluded coronary arteries [79]
MMA triaxial accelerometer (ERNO Raumfahrttechnik/Deutsche Aerospace)	33 mm \times 87 mm \times 65 mm; Weight: 165 gram	0.1 to 100 Hz;	3 μ g	BCG measurement in spaceflight [76]

Endevco 752A12 piezoelectric accelerometer	Height: 23.6 mm Weight: 13 gram	bandwidth (±5%): 1- 10 kHz; 8000 Hz;	<150 µg over 1- 10 kHz bandwidth; Sensitivity: 100 mV/g;	Recording heart sounds and respiratory sounds for sleep apnea screening [74, 75]
S12-M1S5B; PRIMO Co	dimension: 10 mm diameter and 5.4 mm height;	Resonant frequency: 0.8 kHz- 1.2 kHz;	sensitivity: -35 dBv at 100 Hz;	Heart sound mapping on the chest to study propagation route [83]
PCB 393C piezoelectric accelerometer	diameter: 57.2 mm; height: 54.9 mm; Weight: 885 gram;	(±5%): 0.025 to 800 Hz;	0.1 mg over 1- 10000 Hz; Sensitivity: 1000 mV/g	Measurement of low-frequency cardiac vibrations or seismocardiography on the chest wall [70] [69]
PPG sensor	Coin-size	3-dB frequency response: 75 Hz to 2,000		lung sound sensing [51-59]

		Hz, [55]		
Siemens EMT 25C	Weight:15.4 g; height:13 mm; diameter: 28 mm;	100-1200 Hz (a roll-off of -15 dB/octave beyond 1200 Hz) [16]	80 mV/g [50]	Various physiological sounds monitoring [16, 34-49].
Our work	Weight: 5 gram; dimension: 35mm×18mm ×7.8mm;	resonant frequency: ~1.1 kHz	40 ng/√Hz above 200 Hz Sensitivity: 870 mV/g (before amplification)	Heart and lung sound monitoring [84]

2.2 Design

2.2.1 Asymmetric-gapped cantilevers structure

Fig. 2.1(a) shows the basic structure of a conventional accelerometer: a proof mass suspended by one cantilever beam. A piezoelectric layer is integrated on the surface of the cantilever beam. Fig. 2.1(b) shows the schematic structure of the accelerometer based on

asymmetrical gapped cantilever. It comprises a top piezoelectric beam ($w_2 \times t_2 \times l$), a bottom mechanical beam ($w_1 \times t_1 \times l$) and a proof mass or lever ($w_{pm} \times t_{pm} \times l_{pm}$). The distance between middle planes of top and bottom layers is D .

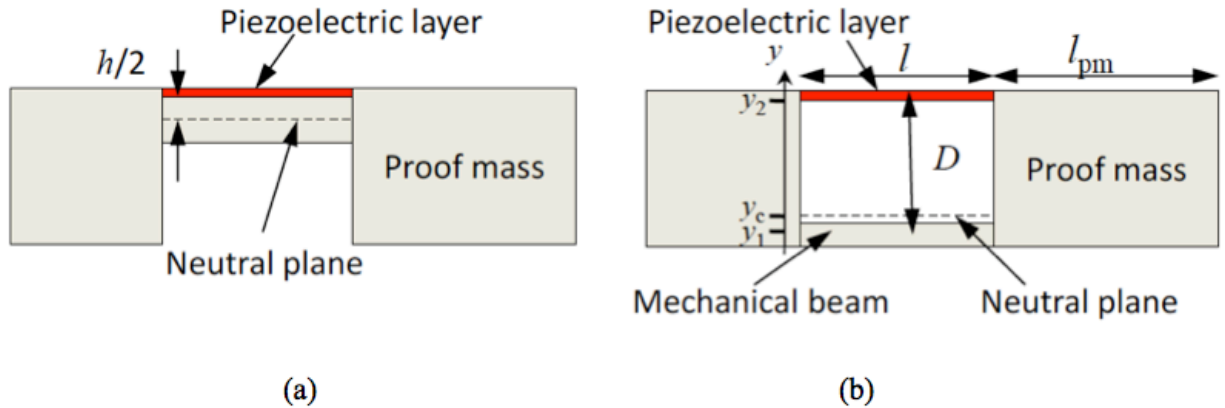


Figure 2.1 Comparison of the (a) conventional accelerometer (h is the cantilever thickness) and (b) new accelerometer design based on decoupled piezoelectric layer (asymmetric gapped cantilever).

To analyze the asymmetric gapped cantilever, an imaginary cut is assumed between cantilever beams and proof mass as shown in Fig. 2.2.

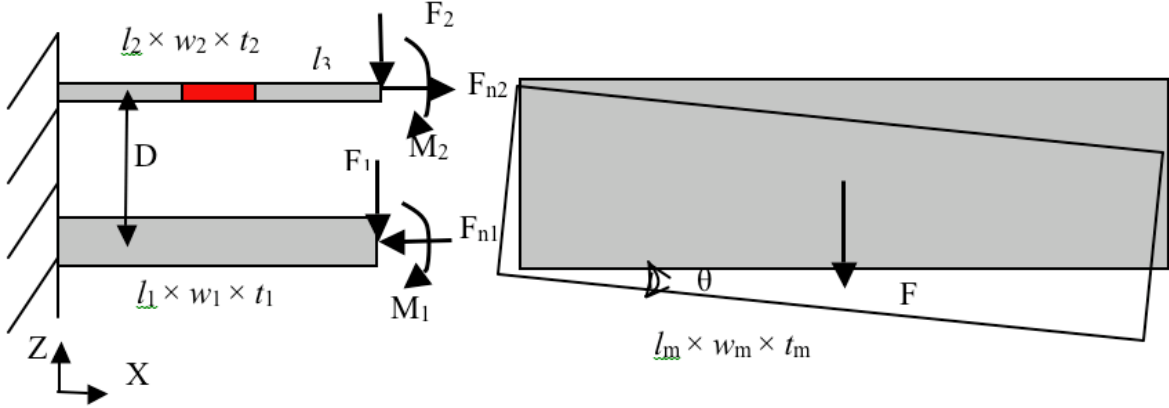


Figure 2.2 Forces and bending moments applied to the cantilever. F_{n1} , F_{n2} , F_1 , F_2 , M_1 and M_2 are normal forces, shear forces and bending moments on bottom and top beams respectively, F is the force on proof mass in z direction, and D is the distance between top and bottom beams.

Based on force and bending moment equilibriums, the following conditions need to be satisfied[11]

$$F_{n1} - F_{n2} = 0 \quad (2.3)$$

$$F_1 + F_2 - F = 0 \quad (2.4)$$

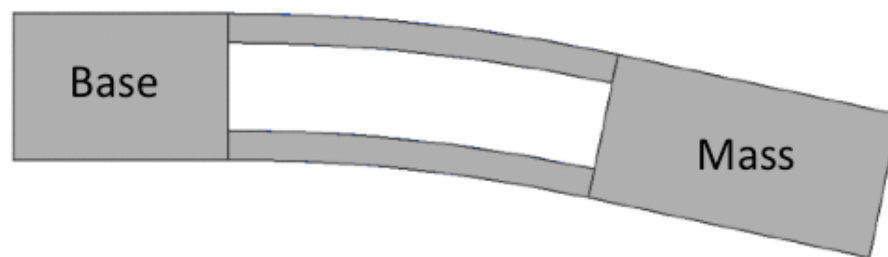
$$M_1 + M_2 + F_{n1} \frac{D}{2} + F_{n2} \frac{D}{2} - F \frac{l_{pm}}{2} = 0 \quad (2.5)$$

$$z_1 = z_2 \quad (2.6)$$

$$\theta_1 = \theta_2 = \theta \quad (2.7)$$

$$D\theta = \left(\frac{F_{n1}}{E_1 A_1} + \frac{F_{n2}}{E_2 A_2} \right) l = \theta \quad (2.8)$$

It is worth noting that the deformation of the asymmetric gapped cantilever can be decomposed into pure bending (rotational movement) and shear modes. (translational movement) as shown in Fig. 2.3. Since the plane assumption is not valid in this case, conventional Euler-Bernoulli beam theory cannot be applied here. New analytical model has been developed for the asymmetrical gapped cantilever [85-88].



(a) Pure bending (rotational movement)

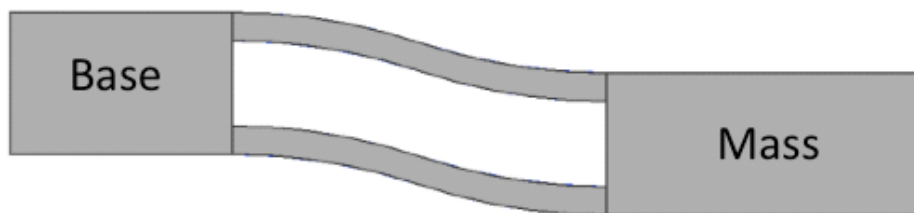


Figure 2.3 Two deformation modes of the asymmetrically-gapped cantilever.

The effective neutral plane of the asymmetrical gapped cantilever for pure bending mode is

$$y_c = \frac{E_1 w_1 t_1 y_1 + E_2 w_2 t_2 y_2}{E_1 w_1 t_1 + E_2 w_2 t_2} \quad (2.9)$$

where y_1 and y_2 are the vertical positions (please refer to Fig. 2.1 (b)), E_1 and E_2 are Young's moduli of the bottom and top beams, respectively. The bending rigidities for pure bending and S-shape bending R_p and R_s are given by

$$R_p = E_1 \left(\frac{w_1 t_1^3}{12} + (y_1 - y_c)^2 w_1 t_1 \right) + E_2 \left(\frac{w_2 t_2^3}{12} + (y_2 - y_c)^2 w_2 t_2 \right) \quad (2.10)$$

$$R_s = E_1 \frac{w_1 t_1^3}{12} + E_2 \frac{w_2 t_2^3}{12} \quad (2.11)$$

The spring constants of the two modes are:

$$k_p = \frac{4R_s}{l^3} \frac{1}{\alpha^2 \beta} \quad (2.12)$$

$$k_s = \frac{12R_s}{l^3} \quad (2.13)$$

where $\alpha = (l+l_{pm})/l$ and $\beta = R_s/R_p$. Then, the total effective spring constant can be expressed as

$$k_E = \left(\frac{1}{k_p} + \frac{1}{k_s} \right)^{-1} = \frac{12R_s}{l^3} \frac{1}{3\alpha^2 \beta + 1} \quad (2.14)$$

Based on Rayleigh-Ritz method [89], the resonant frequency is

$$f_0' = \frac{1}{2\pi} \sqrt{\frac{R_s}{ml^3} \frac{12(3\alpha^2\beta + 1)}{(3\alpha^2\beta + 1)^2 + 3\alpha^2\beta^2(\alpha - 1)^2}} \quad (2.15)$$

The normal strain experienced by the top piezoelectric beam is:

$$\varepsilon_2 = \frac{ma(l + l_{pm})(y_2 - y_c)}{2R_p} \quad (2.16)$$

where a is the acceleration applied. It can be clearly observed that the sensitivity is proportional to $y_2 - y_c$, the distance between the top piezoelectric beam and the neutral plane of the asymmetrical gapped cantilever. This distance is approximately equal to the height of the gap for asymmetrical gapped cantilevers. In comparison, for the conventional cantilever, this distance is only about half of the cantilever thickness ($h/2$) as shown in the Fig. 2.1 (a). If the spring constants of the two designs are the same, the sensitivity of the new design will be $D/(h/2)$ times of the conventional cantilever. Since D can be much larger than $h/2$, the sensitivity of the new design will be orders of magnitude higher than the conventional one.

2.2.2 Energy aspect

The advantage of the new structure can also be explained from the energy perspective. We will examine this from the perspective of the sensitivity and the minimum detectable acceleration in this session. The output signal of the sensor is

$$V^2 = \left(\frac{Q}{C}\right)^2 \quad (2.17)$$

If the strain is uniform, the relationship between charge and energy stored in the piezoelectric layer can be expressed as

$$\frac{Q^2}{2C} = E_e \quad (2.18)$$

From equation (2.17) and (2.18), the voltage sensitivity can be derived as

$$\left(\frac{V}{a}\right)^2 = \frac{2}{Ca^2} E_e \quad (2.19)$$

And the minimum detectable acceleration can be derived as

$$a_{min} = \frac{\sqrt{2k_B T \frac{\eta}{\pi C} \ln\left(\frac{f_2}{f_1}\right)}}{\sqrt{\frac{2E_e}{Ca^2}}} = \sqrt{\frac{2k_B T \eta \ln\left(\frac{f_2}{f_1}\right)}{\pi E_e / a^2}} \quad (2.20)$$

Based on the equation 2.19 and 2.20, it could be concluded that the voltage sensitivity is proportional to the total energy store in the piezoelectric layer E_e , and the minimum detectable acceleration a_{min} is inversely proportional to the square root of E_e . Therefore, in order to improve sensitivity and resolution, it is desirable to allocate as much energy as possible for strain sensing from the total energy applied. Note that the vibration energy is distributed in different parts of the asymmetric gapped cantilever with different forms. However, what is effective in generating output voltage is only the energy stored in the top sensing layer in the form of normal strain. Here we defined the energy efficiency η as the ratio of the energy stored by normal strain of the top sensing layer to the total mechanical energy, which can be calculated in two steps.

First, the ratio of the pure-bending energy to the total energy can be calculated from spring constants, which is [11, 88]

$$\eta_1 = \frac{k_s}{k_p + k_s} = \frac{1}{1/3\alpha^2\beta + 1} \quad (2.21)$$

The pure bending energy is further distributed in both top and bottom beams. The percentage of pure bending energy stored in the top sensing layer in the form of normal strain is

$$\eta_2 = \frac{E_2 w_2 t_2 (y_2 - y_c)^2}{R_p} = (1 - \beta)(1 - \gamma) \quad (2.22)$$

where $\gamma = (y_c - y_1)/D = d_1/D$. Therefore, the total percentage of the vibration energy used for strain sensing is

$$\eta = \eta_1 \eta_2 = \frac{(1 - \beta)(1 - \gamma)}{1/3\alpha^2\beta + 1} \quad (2.23)$$

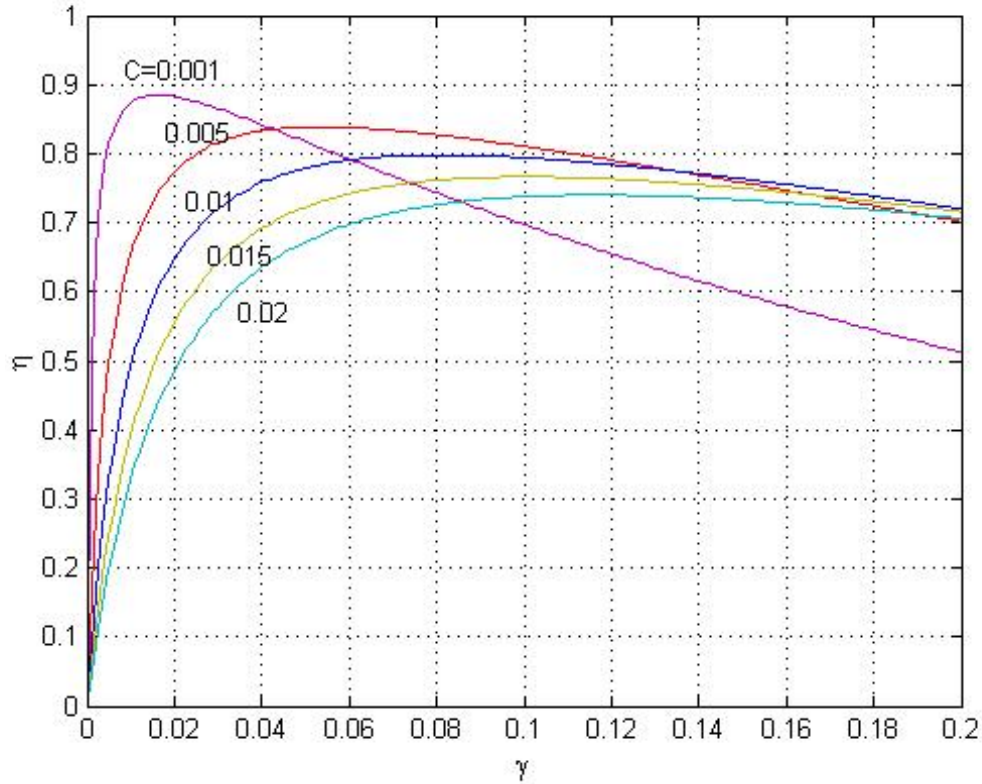


Figure 2.4 Plot of efficiency η as a function of γ with different C ($\alpha = 11$)[86]

The optimal γ that results in the maximum efficiency is

$$\gamma_0 = \frac{1}{1 + \sqrt{1 + \frac{1}{C} + \frac{1+C}{C^2(3\alpha^2 + 1)}}} \quad (2.24)$$

where $C = t_1^2/12D^2$. The plot of efficiency η as a function of γ with different C is presented in Fig. 2.3. Once γ_0 has been decided, we can easily find the distance between neutral plane and top piezoelectric beam d_2 , and other related parameters such as w_1 , w_2 and t_2 .

In conventional piezoelectric cantilever, there is typically 30-40% of the total mechanical energy stored in the piezoelectric layer in the form of normal strain, contributing to the output signal. In comparison, the asymmetrical gapped cantilever allows 87% or even higher percentage of the mechanical energy to be used for piezoelectric sensing.

2.3 FEA simulation

2.3.1 Introduction

Even though the basic physical principles could be used to analyze the behavior of the mechanical systems theoretically, it is prohibitively difficult to solve the equations of a complex structure or boundary conditions. In many cases, in order to approach a theoretical solution, some approximations are made to simplify the problem. For example, in the analysis of the asymmetrical gapped cantilever above, the proof mass is assumed rigid and the mass of the beam is neglected. Therefore, several numerical methods are developed to further verify the theoretical models or to analyze the complicated structure, which are extremely hard to be get theoretical solution.

Finite Element Analysis is one of such approach. By breaking a complex mechanical structure down into a large number of simple analogue finite elements, the computer is able to solve the individual element with its loads and boundary condition applied. Thus the FEA approach translates a complicated problem into a “sum” of many simpler problems. It is worth noting that the finer the breaking down (meshing) is, the more accurate the final result is. However, due to the large amount of calculation during problem solving, the number of elements is always limited by the computer’s capability. With reasonable fine meshing, the finite element

analysis could offer a close enough prediction on the system behavior such as force, heat response and fluid flow property. The simulated result could be used as a guideline for designing engineering product.

In order to verify the theoretical model of asymmetrical gapped cantilever developed above, we use COMSOL FEA software 4.3a to carry out a numerical simulation of the structure and compare the two results. The simulation flow is summarized in Table 2.3:

Table 2.3 The simulation flow chart

Pre-processing	Choose solver type	Post-processing	Plot selected results
	Set model geometry		Error analysis
	Set material property		Export results
	Set boundary condition		
	Set load condition		
	Meshing		
	Set solving parameters		

2.3.2 Model verification

In order to verify the analytical model developed above, we examine the corresponding FEA simulation model for two different cases in this session: 1) Ideal condition asymmetric-gapped cantilever; 2) Real condition asymmetric-gapped cantilever.

In the first case, the FEA model preserve all the assumptions made during analytical derivation: 1) the Young's modulus of the proof mass is set to be very high so that the

deformation of the proof mass could be neglected; 2) the density of the beams is set to be very low so that the mass of the beams could be neglected. On the other hand, the real condition cantilever is also simulated in case 2 to verify the assumptions made is valid and do not change the behavior of the real cantilever by much. In the static analysis, a 10 m/s^2 acceleration is applied in vertical direction on the proof mass. The dimension of a specific design of the asymmetric gapped cantilever is presented in Table 2.4 The comparison of analytical and simulation results for both ideal and real cases is presented below in Table 2.5.

Table 2.4 Design parameters of the asymmetric gapped cantilever

	Length	Width	Thickness
Top beam	$15 \mu\text{m}$	$7 \mu\text{m}$	$3 \mu\text{m}$
Bottom beam	$15 \mu\text{m}$	$90 \mu\text{m}$	$8 \mu\text{m}$
Proof mass	$1500 \mu\text{m}$	$250 \mu\text{m}$	$110 \mu\text{m}$

Table 2.5 Analytical and simulation results for both ideal and real cases

	Analytical	Simulation (ideal)	Difference (%)	Simulation (real)	Difference (%)
Spring constant (N/m)	1.06e+03	1.15e+03	8.5	1.08e+03	2

Resonant frequency (Hz)	3.10e+04	2.93e+04	5.5	2.87 e+04	7.4
----------------------------	----------	----------	-----	-----------	-----

We could see that the simulation results agree well with the analytical model. The error is within 10%. In the real case, the spring constant and resonant frequency is slightly higher than the ideal case as expected because it takes consideration of the bending of the proof mass.

2.4 Noise

Noise is another critical factor to consider in the development of piezoelectric accelerometers. To understand the noise source will help the designer to further lower the noise floor and improve the minimum detectable acceleration of the sensors. This is particularly important for small signal applications such as seismic vibration detection at a frequency range from 0.001Hz to 100Hz. Even though in most cases, the overall noise is determined by the noise from the electronics such as amplifier, with the continuous development of low noise IC, the noise of the electronics could be small enough that the overall noise is dominated by the two fundamental noises of the piezoelectric accelerometer: the thermal-mechanical noise and the thermal-electrical noise. In this session, we will discuss all these three noises.

2.4.1 Thermal-mechanical noise

The origin of the thermal-mechanical noise is based on the well-known mechanism of Brownian Motion[15]. A cantilever structure based piezoelectric accelerometer could be modeled as a damped harmonic oscillator as shown in Fig. 2.5.

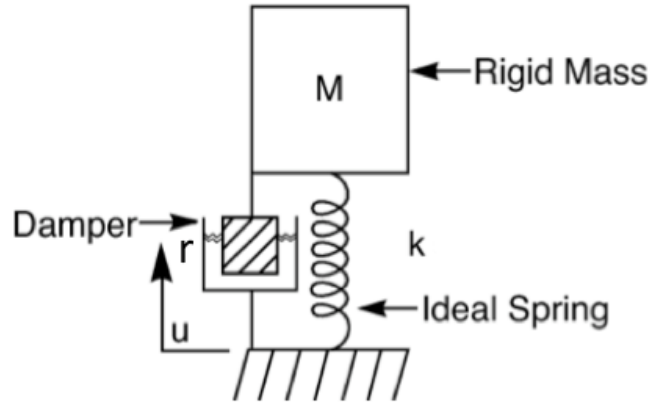


Figure 2.5 A cantilever structure based piezoelectric accelerometer could be modeled as a damped harmonic oscillator with a spring constant k , mass M and damping ratio r .

Analogous to Johnson noise of a resistor, a mechanical spring-mass system always experiences a white noise force given by[90]

$$F_{th}^2/\Delta f = 4k_B T r \quad (2.25)$$

where $r = \omega_0 m/Q$ is the equivalent damping coefficient of the oscillator, k_B is the Boltzmann's constant, T is the absolute temperature. And Q is the quality factor of the harmonic oscillator.

Therefore, for f at all $f \ll f_0$ (resonant frequency), the acceleration spectral density of the thermal-mechanical noise a_{nm} is expressed as [90]

$$a_{nm} = \sqrt{\frac{4k_B T \omega_0}{mQ}} \quad (2.26)$$

And the corresponding voltage spectral density v_{nm} is[90]

$$v_{nm} = \sqrt{\frac{4k_B T \omega_0 Q_T^2}{mQ C^2}} \quad (2.27)$$

where Q_T is the charge sensitivity and C is the capacitance of the piezoelectric transducer.

In most cantilever-based accelerometers, the thermo-mechanical noise determines the lowest noise floor and is independent on the transduction mechanism, sensor structure, and readout circuits. Because it exists at the input of the sensor, increasing the sensor sensitivity will correspondingly increase the thermo-mechanical noise level as well. However, by optimizing the sensor design to lower other larger noises, the sensor could reach the thermo-mechanical noise dominant range. And this would be the highest resolution the accelerometer could achieve.

2.4.2 Thermal-electrical noise

Thermal-electrical noise is the intrinsic noise of piezoelectric material and depends on its loss factor η , which is inverse of the quality factor of the piezoelectric material[90]. Therefore, we have the following equivalent circuit model in Fig. 2.6 where the conductivity is assumed to be 0.

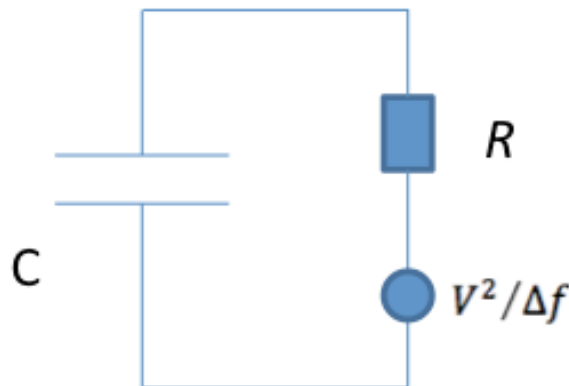


Figure 2.6 The equivalent circuit of piezoelectric material

The equivalent noise resistor R , due to the dielectric loss, leads to a Johnson noise that is a function of the loss factor η : [90]

$$R = \frac{1}{\omega C(\eta + \frac{1}{\eta})} \quad (2.28)$$

For most piezoelectric material, the loss factor is in the range from 0.014 to 0.017. So R could be simplified as $R = \frac{\eta}{\omega C}$. By submitting equation (2.28) to the general Johnson noise expression $v = \sqrt{4k_B TR}$, the voltage spectral density of the thermal-electrical noise a_{ne} is expressed as[90]

$$v_{ne} = \sqrt{\frac{4k_B T \eta}{\omega C}} \quad (2.29)$$

And the corresponding acceleration spectral density a_{ne} is[90]

$$a_{ne} = \sqrt{\frac{4k_B T \eta C}{\omega Q_T^2}} \quad (2.30)$$

The thermal-electrical noise is generally larger than thermal-mechanical noise in the piezoelectric transducer. This is particularly true in the low frequency range because the thermal-electronic noise is inversely proportional to the frequency with a $1/f$ noise type. With the development of the lower noise IC, some piezoelectric accelerometers already enter the thermal-electrical noise dominant range.

2.4.3 Total noise

By including the electronic noise of the amplifier, the total acceleration noise spectral density at the input of the readout circuit amplifier can be derived as [90]

$$a_n = \sqrt{4k_B T \left(\frac{\omega_0}{mQ} + \frac{\eta C}{\omega Q_T^2} \right) + \left(\frac{e_n C}{Q_T} \right)^2} \quad (2.31)$$

And the total voltage noise spectral density is [90]

$$v_n = \sqrt{4k_B T \left(\frac{\omega_0 Q_T^2}{C^2 m Q} + \frac{\eta}{\omega C} \right) + e_n^2} \quad (2.32)$$

Here a practical example of the noise analysis of the piezoelectric accelerometer based on a four-stage asymmetric-gapped cantilever structure is given to illustrate the theory above. The dimension of the cantilever is shown in Table 2.6. In the noise calculation, the amplifier OPA 129 from Texas Instrument is used as an example of the read out circuit. Its input voltage noise spectral density is shown in Fig. 2.7 below. The calculated result shows that the amplifier noise is dominant by an order of amplitude below 10Hz. As shown in Table 2.7, the electronic noise and thermal-electrical noise become comparable as the frequency increases. The thermal-mechanical noise stays the same through the frequency spectrum and is the lowest noise level. This example also theoretically demonstrated the ability of accelerometer based on the asymmetric-gapped cantilever structure to reach Nano gram resolution.

Table 2.6 Geometric properties of bottom beam, top beam and proof mass for four-stage cascaded asymmetric-gapped cantilever.

Dimension	Top sensing	Bottom mechanical	Proof mass
t (mm)	0.508	1.0	5.1
w	1.8	16	65(84.5)
l	10×4	10×4	110.5

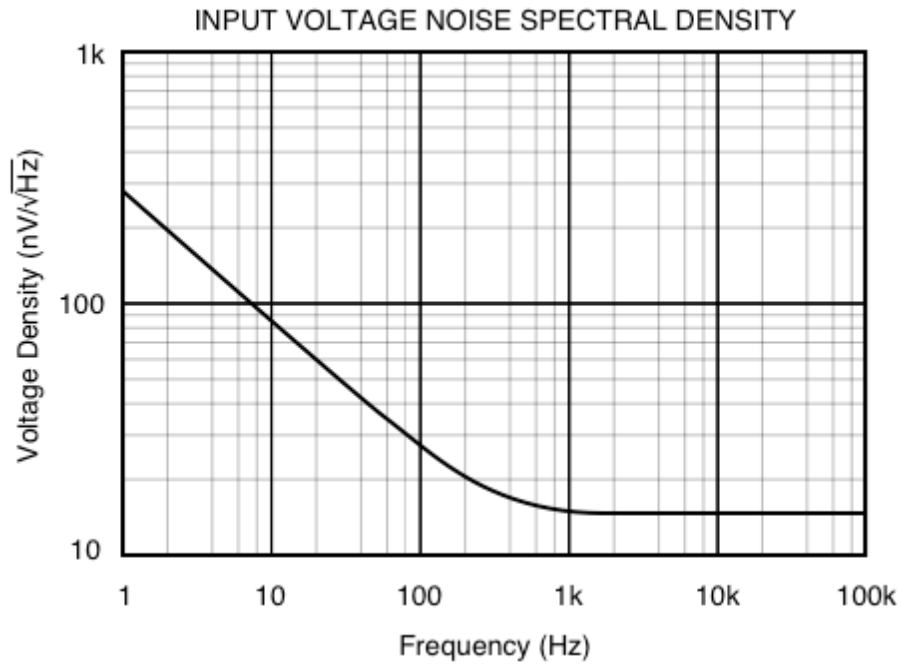


Figure 2.7 Input voltage noise spectral density of TI OPA129

Table 2.7 calculated noise level of the cascaded asymmetric-gapped cantilever in Table 2.6.

Noise	0.01 ~10Hz bandwidth	10 Hz	100 Hz	1000Hz
Thermal Mechanical Noise	0.9ng	0.9 ng/√Hz	0.9 ng/√Hz	0.9 ng/√Hz
Electrical Thermal Noise	45ng	12 ng/√Hz	3.8 ng/√Hz	1.2 ng/√Hz
Amplifier Noise	130ng	13 ng/√Hz	4.5 ng/√Hz	2.7 ng/√Hz
Total noise	137ng	18 ng/√Hz	5.9 ng/√Hz	3.0 ng/√Hz

2.5 Readout circuit

Charge amplifier and voltage amplifier are two common readout circuits for high impedance piezoelectric transducers. In this session, we will discuss the key features of

piezoelectric transducers using these two types of readout circuit including signal to noise ratio (SNR), output voltage and bandwidth.

2.5.1 Voltage amplifier

Voltage amplifier is widely used in signal processing circuit to amplify weak voltage signals. Because the piezoelectric transducer has very high capacitance, the amplifier output is decided by the amount of capacitance seen by the sensor, and the connect cable capacitance needs to be considered for the voltage amplifier design. Fig. 2.8 shows the voltage amplifier mode circuit model and the piezoelectric transducer is modeled as a charge source with a shunt capacitor C_p and resistor R_p .

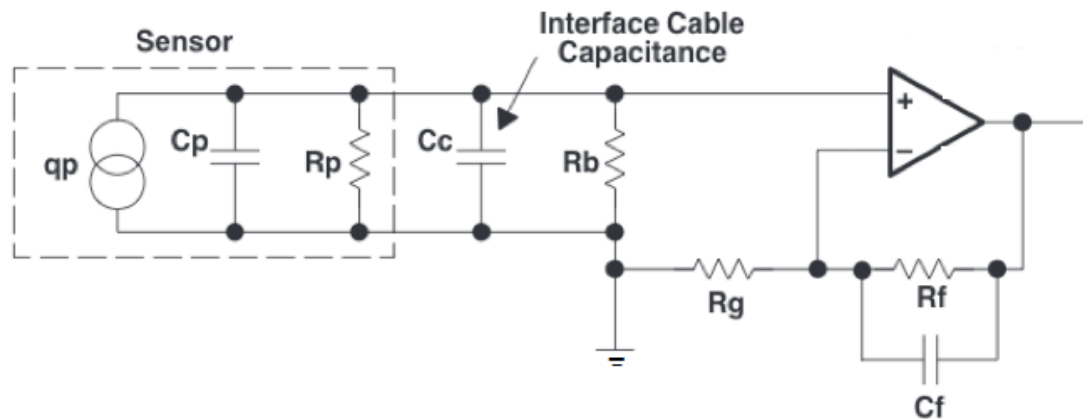


Figure 2.8 Voltage amplifier mode circuit model

The signal at the output of the voltage amplifier can be derived as

$$V_0 = \frac{qp}{C_p + C_c} \left(1 + \frac{R_f}{R_g} \right) \quad (2.33)$$

Since the noise at the output of the amplifier is $V_{0-n} = v_n \left(1 + \frac{R_f}{R_g}\right)$ where v_n is the voltage noise at the input of the amplifier that is derived in session 2.4, the signal to noise ratio SNR is

$$SNR = \frac{V_0}{V_{0-n}} = \frac{qp}{v_n(C_P + C_C)} \quad (2.34)$$

If $C_P \gg C_C$, $SNR = \frac{qp}{v_n C_P} \cdot \frac{C_P}{(C_P + C_C)} \cong \frac{S_v a}{v_n}$. The voltage sensitivity S_v is critical in achieving a high SNR.

If $C_P \ll C_C$, $SNR \cong \frac{qp}{v_n C_C}$. The charge sensitivity becomes critical in achieving a high SNR.

Therefore, only when the capacitance of the interface cable is much smaller than it of the piezoelectric transducer, the voltage amplifier is suited as the readout circuit to achieve a high SNR. In practice, this could be translated to the distance between the voltage amplifier and the transducer needs to be minimized.

2.5.2 Charge amplifier

The charge amplifier is a current integrator to amplify signals from a capacitive nature source. It transfers the input charge to smaller feedback reference capacitor and produces a lifted voltage equal to the voltage across the reference capacitor. Fig. 2.9 shows the charge amplifier mode circuit model and the piezoelectric transducer is modeled as a charge source with a shunt capacitor C_p and resistor R_p .

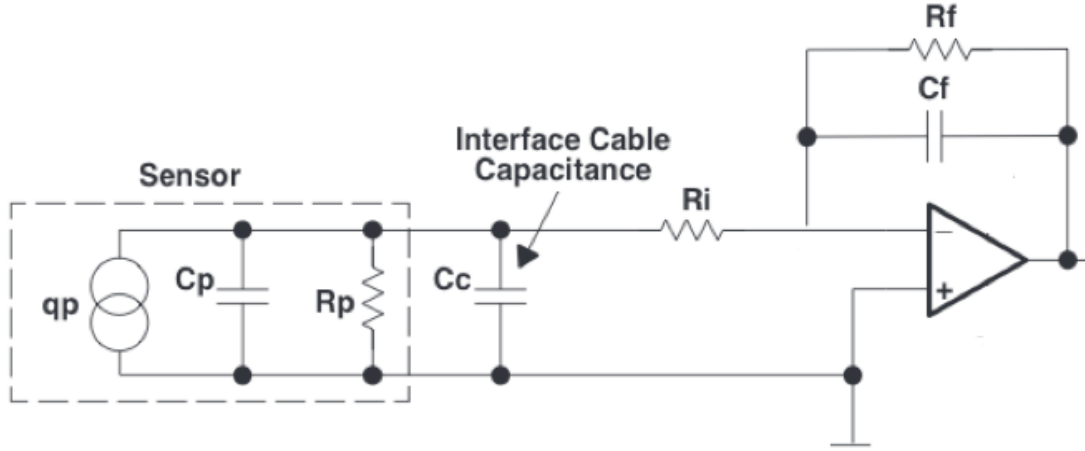


Figure 2.9 Charge amplifier mode circuit model

The signal at the output of the charge amplifier can be derived as

$$V_0 = \frac{qp}{C_f} \quad (2.35)$$

Since the noise at the output of the charge amplifier is $V_{0,n} = v_n \left(1 + \frac{C_p}{C_f}\right)$ where v_n is the voltage noise at the input of the amplifier that is derived in session 2.4, the signal to noise ratio SNR is

$$SNR = \frac{V_0}{V_{0,n}} = \frac{qp}{v_n(C_p + C_f)} \quad (2.36)$$

If $C_p \gg C_f$, $SNR \cong \frac{S_v a}{v_n}$. It can be concluded that the voltage sensitivity is still critical for the charge amplifier design. From the material point of view, what matters is the piezoelectric voltage coefficient g (Vm/N). It is worth noting that even though the SNR is inversely proportional to the capacitance of the piezoelectric transducer, it does not necessarily indicate that a piezoelectric material with a smaller capacitance will yield a better SNR if the assumption

$C_p \gg C_f$ is invalidated. Since the SNR is independent of the interface cable capacitance, the charge amplifier could be used in the circuit that the amplifier is far away the transducer and the interface cable capacitance is high.

2.5.3 Comparison of the lower cutoff frequency

The lower cutoff frequency of the voltage amplifier in Fig. 2.8 is

$$f_{L_V} = \frac{1}{2\pi R_p(C_p + C_c)} \quad (2.37)$$

The lower cutoff frequency of the charge amplifier in Fig 2.9 is

$$f_{L_C} = \frac{1}{2\pi R_f C_f} \quad (2.38)$$

In order to make a fair comparison of the lower cutoff frequency of the voltage amplifier and the charge amplifier, the output voltage and the output offset voltage are kept the same.

$$v_0 = \frac{qp}{C_p + C_c} \left(1 + \frac{R_f}{R_g} \right) = \frac{qp}{C_f} \quad (2.39)$$

$$v_{out_off} = I_B R_p \left(1 + \frac{R_f}{R_g} \right) = I_B R_f \quad (2.40)$$

From the equation (2.39) and (2.40), we could derive that

$$f_{L_V} = f_{L_C} \quad (2.41)$$

Therefore, the voltage amplifier and the charge amplifier perform the same on the lower cutoff frequency.

2.6 Summary

In this chapter the systematically study of gapped cantilever based accelerometer is carried out. First, the operation principle of accelerometers and specifications that are important for mobile healthcare is discussed. Next, accelerometers, including both commercial products and research prototypes, which have been reported in literatures for physiological acoustic sensing is reviewed. While accelerometers have great potential for physiological acoustic signal monitoring, the state of the art accelerometers do not have high enough sensitivity and resolution to capture the detailed information for diagnostic purpose.

Therefore, in the following session, the accelerometer based on an innovative asymmetric gapped cantilever, where the top sensing layer and the bottom mechanical lay is separated by a gap, is introduced. To explain the structure, the analytical model is first derived. Unlike conventional cantilever, the asymmetric gapped cantilever has both pure bending and shear bending. The shear bending should be minimized since it does not contribute to the output signal. The optimization of the structure is then discussed from the energy point of view. A parameter η is defined as the ratio of the bending energy on the sensing beam to the total energy in the whole structure. An optimized design can be achieved by increasing η .

The FEA simulation is then carried out to verify the analytical model by using the software Comsol version 4.3. Two cases are studied in the simulation: Ideal condition where the proof mass is assumed to be rigid and real condition where the proof mass is not rigid. It is observed that the simulation result agrees with the analytical model calculation closely.

Finally, the signal processing circuit for piezoelectric accelerometer is also discussed. The performance of two types of amplifiers are compared: charge amplifier and voltage amplifier. The noise floor, which determine the resolution of accelerometer, is discussed in detail particularly. Which in many cases the amplifier noise plays a dominant role in the overall noise, the piezoelectric transducer could enter a thermal mechanical noise dominant range sometimes with an optimized design.

In conclusion, a large variety of accelerometers have been used for physiological acoustic sensing. This chapter discussed different critical aspects of accelerometers for this application. In particular, the accelerometer based on an asymmetric gapped cantilever design is proposed and verified by FEA simulation. Compared with the accelerometer based on the conventional cantilever, the new design yield better sensitivity and resolution.

CHAPTER 3 CONTINUOUS CARDIO-RESPIRATORY SOUND MONITORING

3.1 Introduction

The cardio-respiratory signal is one of the physiological vital signs to assess a person's health [91-93]. Auscultation of the chest wall sounds which include both heart and lung sounds is a noninvasive, traditional and effective way to capture and diagnose many cardiovascular and respiratory diseases. A variety of critical information is included or can be derived from this signal such as heart sounds, heart rate, lung sound and even blood pressures, etc.)

3.1.1 Heart sound

Heart sounds are generated by the beating heart and the flow of blood through the heart. These auditory vibrations reflect the heart condition through its intensity, frequency, quality, and duration [94]. The recording of heart sound is called phonocardiography (PCG). There are several other terminologies related to heart sound monitoring such as seismocardiography (SCG), which refers to the measurement of chest vibration induced by heart beats. In some sense, SCG can be considered as the low-frequency components of heart sounds.

Typical signals to look for in the normal heart sound are the first heart sound (S1) and the second heart sound (S2). These two sounds are related to closure of the mitral and tricuspid valves. In a patient with heart diseases, a variety of additional signals are presented, such as heart murmurs, S1 split, S2 split, the third heart sound (S3) and the fourth heart sound (S4).

While electrocardiographic (EKG) method is a popular tool in heart examination in hospital nowadays, there are some heart diseases which are difficult to diagnose through EKG signal such

as the structural abnormalities in heart valves. This kind of defects is not reflected on the electronic signal of the heart, but causes changes in vibration/acoustic signals. In such cases, heart sounds provide important diagnostic information.

Therefore, heart sound monitoring could offer significant clinical value. One application is to monitor the congestive heart failure development through S3 in the patient heart sound [95-97]. S3 reflects heart features such as decreased cardiac output, reduced ejection fraction and elevated end-diastolic pressures that commonly occur in heart failure. However, the weak intensity, short duration and low frequency (typically in the range 10-70Hz) characteristics of the third heart sound make it very difficult to be captured and identified by human ears through traditional auscultation devices such as stethoscopes. This also results high diagnosis disagreement among physicians. However, this problem can be addressed by utilizing highly sensitive accelerometers and computer aided method to capture and identify S3 more effectively [95, 97, 98].

Detection of coronary artery disease from heart sounds has been investigated [65, 99, 100]. Coronary artery disease occurs when the coronary arteries are thickened or narrowed by deposited plaques. It is hypothesized that the occluded arteries lead to restricted blood flow which accordingly generate characteristic turbulent sounds [99].

There have been many efforts on extracting blood pressure from heart sounds [101-106]. If successful, this will provide a noninvasive method to continuously measure blood pressure, making significant impact on the management of cardiovascular diseases. For example, Zhang et al. proposed that the timing of the second heart sound is related to aortic blood pressure [104]. Imtiaz et al. measured SCG using a MEMS accelerometer and tried to find a correlation between

SCG and systolic blood pressure [30]. The reflected wave transit time (RWTT) extracted from arterial acceleration signals was found to be strongly coupled with the systolic blood pressure [107].

There are many other parameters can be extracted from heart sound. For example, changes in the left ventricular function have been correlated the changes of heart sounds or SCG [72]. Bombardini et al. derived diastolic times and the diastolic/systolic time ratio from first and second heart sounds recorded by an accelerometer [26]. More detailed discussion of clinical significance of heart sounds can be found in [31].

3.1.2 Fetal monitoring

By picking up the acoustic signal of the fetus transabdominally, accelerometers can also be used to monitor the heart beats/sounds or movements of fetus. Because the strength of the acoustic signal generated from the fetus depends on the week of the gestation and the weight of the fetus, the signal can be too weak to be detected in early gestation. The phonocardiography (PCG) method normally becomes viable after the 30th week of gestation, and in some cases, as early as in the 28th week [108].

Compared with the traditional cardiotocography (CTG) based on the ultrasonic techniques, the acoustic based fetal PCG has the following advantages. First, enabled by accelerometers, it is a lost-cost, easy-to-carry-out fetal surveillance method, which is especially desirable in developing countries. One of such application is to detect fetal congenital heart diseases [109]. In [109], Kovacs et al. presented a signal processing method for murmur discovery from fetal PCG, and demonstrated its potential as a screening technology for the discovery of congenital

heart disease through the cardiac murmurs[108]. Another advantage of fetal PCG is that the acoustic measurement is totally passive and suitable for long term and safe use.

There are also two major challenges for acoustic based fetal PCG. First, because the fetal heart sound is very weak and contains mainly low frequency components (35-110Hz) [110], the acoustic sensor such as accelerometer needs to be designed with a very high sensitivity in the low frequency range to provide a reliable recording for detailed sound analysis. The second challenge is to develop a robust signal processing method to extract useful information in fetal heart sound from the contaminated signal mixed with the maternal heart sound, digestive system artifacts, etc.

Fetal movement is another immediate indicator of fetus's wellbeing. The spontaneous movement reflects the early development of the fetus's central nervous system. For example, study has shown that decreasing in fetal movement is associated with fetal distress and placental dysfunction [111]. Moreover, the defection such as chromosome abnormalities, anencephaly, and cerebral malformations could also cause abnormal fetal movement[112].

Fetal movement can be captured by placing a small acoustic sensor on the mother's abdomen. An ambulatory accelerometer-based fetal activity monitor (AFAM) for continuous fetal movement monitoring, and the detection and quantitatively characterization of fetal movements has been developed [113, 114].

3.1.3 Respiratory sound

The specific sound caused by friction of air against the lining of the airways through the lung fields is known as lung sound or respiratory sound. It is a fairly weak acoustic signal with a

vibration amplitude less than 10 μm . The intensity, spectrum, and dynamics of lung sound provide critical information in diagnosing respiratory diseases such as asthma, tuberculosis, bronchitis and influenza [115-118]. For example, the median frequency (F50) of the lung sound was higher in asthmatic patients (239 Hz) than in healthy individuals (206 Hz)[116, 118, 119]. Another example is to detect flow obstruction during bronchial provocation testing for young patients since it does not require maximal breathing effort[119].

Because of its miniature size and low cost, accelerometer is a great tool for continuous respiratory sound monitoring. It has been widely used to detect wheezing sounds for asthma and chronic obstructive pulmonary disease [48, 51, 53, 54, 58]. Other applications such as monitoring of regional ventilation by chest surface acoustical topography in the critical care could also be made possible with continuous multisite recording of respiratory sounds. Sleep apnea study has also been carried by attaching an accelerometer on the suprasternal notch of subjects to measure respiratory and snoring sounds [75]. Bucklin et al. also reported the development of a sleep apnea screening technique based on a MEMS accelerometer [120]. The continuous respiratory sound monitoring will also play important roles in the operation room, by providing prompt information in situations of airway complications such as bronchial intubation, pulmonary edema and tube malfunctioning [121-123].

Besides monitoring respiratory sounds alone, the combined information acquired through simultaneous monitoring of respiratory function, cardiac function, as well as activity level could together help greatly with certain disease diagnosis. For instance, Mann et al. developed an accelerometer-based system for the detection of chronic obstructive pulmonary disorder (COPD) by simultaneous monitoring respiratory and activity signals [124].

More comprehensive discussion of clinical applications of lung sound monitoring can be found in [93].

3.1.4 Technology review

The following session gives a brief introduction of the technology used for cardio-respiratory signal detection and the challenges of continuous monitoring of these signals. As we observed in the hospitals, the most common tool for acquiring the heart and lung sounds is the stethoscope. Since its inventory in France in 1816 by René Laennec, it remains simply conduits for sound conduction between the body surface and the ears. The modern stethoscope could be categorized into two types: acoustic and electronic. The patient's heart and lung sound transmit from a chest piece, via air-filled hollow tubes, to the listener's ears. Because it relies on the mechanical structure which is frequency dependent to amplify the weak cardio-respiratory sound, the chest piece normally consists of two sensing side: a diaphragm to transmit higher frequency sounds and a bell to transmit low frequency sounds. Still, it is a less than ideal acoustic instrument because of the colored transmission of sounds[119]. Unlike acoustic stethoscopes, the electronic stethoscope uses transducer such as microphone to pick up the sound amplified by the air chamber as shown in figure 3.1. Some other technics include placing a piezo-electric crystal within foam behind a thick rubber-like diaphragm, or using an electromagnetic diaphragm with a conductive inner surface to form a capacitive sensor[119].

Despite the fact that electronic stethoscope has enabled PC-based analysis, which could interpret the cardiologic, and respiratory signals according to related algorithms, the stethoscope

still suffers from several drawbacks. First, the difference in the sizes and the shapes of coupling chambers could affect the overall frequency response. Secondly, the stethoscope suffers from ambient noise interference heavily. For instance, to record the signals, the stethoscope typically needs to be held against the skin by hands. This will lead to friction noise and make the detection of weak acoustic signals, such as lung sounds, more challenging. What's more, the stethoscope is only suitable for intermittent auscultation due to its bulky size.

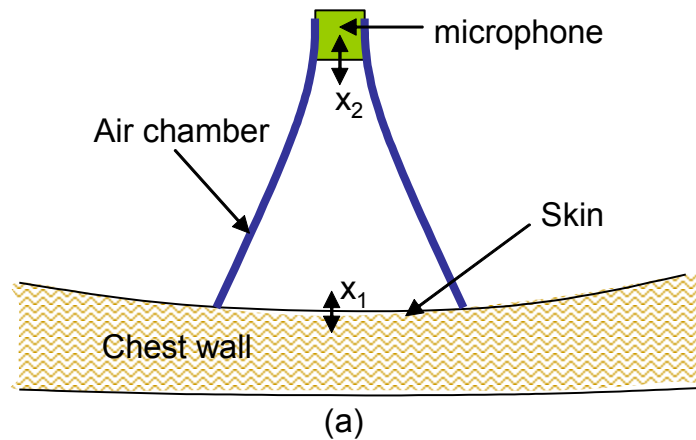


Figure 3.1 A schematic drawing of the operating principle of the stethoscope after [92]

Another approach of detecting heart/lung sounds is based on the accelerometer which is a spring mass system[66, 67, 92, 125]. Compared with the stethoscope, the miniaturized accelerometer can be taped on the chest wall for a more convenient and continuous cardio-respiratory monitoring. However, because it is in direct contact with the skin and does not have an air chamber to couple and amplify the acoustic signal, the accelerometer itself needs to have a very high sensitivity. There have been many efforts in the development of accelerometer based acoustic sensors for heart/lung sound monitoring. Some researchers have used off-the-shelf accelerometers to detect heart/lung sounds. However, these off-the-shelf sensors are either too

bulky or not sensitive enough to capture the details of heart sounds, let alone lung sounds. The accelerometer with the resolution of over $1\mu\text{g}/\text{Hz}^{1/2}$ is required for such measurement. As discussed earlier, the lack of continuous lung sound monitoring is mainly due to the immaturity of the sensor technology in this field. Therefore, the development of a sensitive accelerometer could potentially open doors to various clinical and healthcare applications.

In this chapter, an ultra sensitive piezoelectric accelerometer is proposed to address this issue. It could provide a platform for heart failure patient remote monitoring, continuous asthma monitoring, the assessment of drug effectiveness for pain management in cancer patients, etc. [126-133]. What's more, its miniature size also makes it a perfect candidate for vital sign monitoring among the remote military personnel.

3.1.5 Challenges and prospect

There are a number of technical challenges the accelerometer-based mobile monitoring systems are facing. The first challenge is motion noises and artifacts. Compared with microphones, accelerometers are more sensitive to motion noises and artifacts. Some algorithms have developed to remove motion artifacts. For example, Pandia et al. reported a method that effectively extracts heart sound signals from accelerometer data overwhelmed by motion artifacts [25]. Friction noise, which can be generated between the sensor and the skin or between clothes and the sensor, is more detrimental than motion noise. There are a number of methods to reduce or prevent friction noise including employing low friction noise wire and coating super slippery film on the sensor surface. Alternatively, the sensors can be fixed to cloth to minimize friction.

For mobile or wearable applications, the power source is always a challenge. Currently, battery is still the main power source for accelerometer-based mobile health monitors. There are numerous efforts on developing energy scavenging methods to power wireless sensors without the battery [134-136]. The practical power harvested is typically at microwatt (μW) level. However, most accelerometer-based monitoring systems consume power above milliwatt (mW) level. The majority of the power is consumed by the readout circuits and wireless transmission of data. Low-power electronics is an active research topic currently. However, it is worth noting that there is a tradeoff between the power and the noise of the readout circuits. An amplifier with lower power typically has a higher noise level. Since wireless transmission of data consumes significant amount of power, it is beneficial to integrate on-chip signal processing or storage capabilities.

A key question in this field is probably whether or not clinical relevant information can be extracted from acoustic/vibration signals captured by the accelerometers. There are currently many contradictory conclusions in the literature. For example, the clinical value of GI sounds has been challenged by a few researchers [137, 138]. This is probably due to one or more of the following issues: (1) the sensor is not good enough to capture some subtle signals that contain useful information; (2) the signal captured is corrupted by noises; and (3) there are not satisfactory models that associate the acoustic signatures with specific diseases or clinical conditions.

To further advance this field, we believe that more sensitive sensors need to be developed to capture subtle signals. In addition to MEMS sensors, conventional accelerometers will play

important roles as well. For the conventional accelerometers, the battery and readout circuits can be integrated on the proof mass. Therefore, the overall size of conventional accelerometers still can be kept small enough for wearable applications. Noise reduction/cancellation algorithms and hardware need to be further investigated.

We also envision that various sensors will be integrated with accelerometers to enable multiple-parameter monitoring. For instance, ECG electrodes and oximeter can be integrated with wearable accelerometers to simultaneously detect ECG, blood oxygen, and PCG.

One major obstacle that prevents the wide acceptance of wearable healthcare is probably the inconvenience of wearing the sensor on a daily basis. One approach to address this issue is to integrate sensors to garments, such as the MagIC system [21, 23]. However, smart garments will not be as convenient as regular garments in the foreseeable near future. Therefore, un-obtrusive monitoring, such as BCG monitoring on chairs or beds, probably can be more easily accepted by patients or consumers.

3.2 Design

3.2.1 Structure

The piezoelectric accelerometer is based on an asymmetric-gapped cantilever which is composed of a bottom mechanical layer and a top piezoelectric layer separated by a gap as shown in Fig. 2.1(a). As discussed in chapter 2, because the mechanical strain experienced by the top piezoelectric layer is proportional to the distance between the top beam and the neutral plane, the sensitivity is greatly increased in the gapped cantilever structure case. A meso scale prototype is designed and the respective geometric and material properties are listed in Table 3.2.

Following the theoretical model in chapter 2, a resonant frequency of 1100Hz and an average normal strain of 5.23×10^{-5} on the top piezoresistive beam (with 1 g vertical acceleration) are calculated.

Table 3.1 Geometric and material properties of bottom beam, top beam and proof mass of the asymmetric-gapped cantilever.

	Bottom beam	Top beam	Proof mass
Length (mm)	4	4	20
Width (mm)	15	2	15
Thickness (mm)	0.7	0.127	3
Young's modulus (GPa)	69	66	69
Density (kg/m ³)	2700	7700	2700

3.2.2 FEA simulation

Finite element simulation is also carried out to verify the analytical calculations. The comparison result is summarized in Table 3.2. The simulation agrees well with analytical model with errors less than 10% for both ideal and real cases.

Table 3.2 Analytical and simulation results for both ideal and real cases

	Analytical	Simulation (ideal)	Difference (%)	Simulation (real)	Difference (%)

Normal strain	5.23×10^{-5}	5.35×10^{-5}	2	5.27×10^{-5}	1
Resonant frequency (Hz)	1100	1175	7	1148	4

3.3 Characterization

The packaged piezoelectric accelerometer is placed on a mechanical shaker (Labworks, ET-126B) and characterized by comparing the output with a commercial accelerometer (Model 752A13, Endevco) as shown in Fig. 3.2. The dimension of the accelerometer under characterization is given in section 3.2.1. The overall weight for the packaged sensor is only 5 gram with the size of $35\text{mm} \times 18\text{mm} \times 7.8\text{mm}$ ($l \times w \times t$). Figure 3.3 show a picture of the packaged prototype compared with a penny.



Figure 3.2 The packaged device was mounted on a mechanical shaker. A commercial accelerometer was used to calibrate the acceleration.

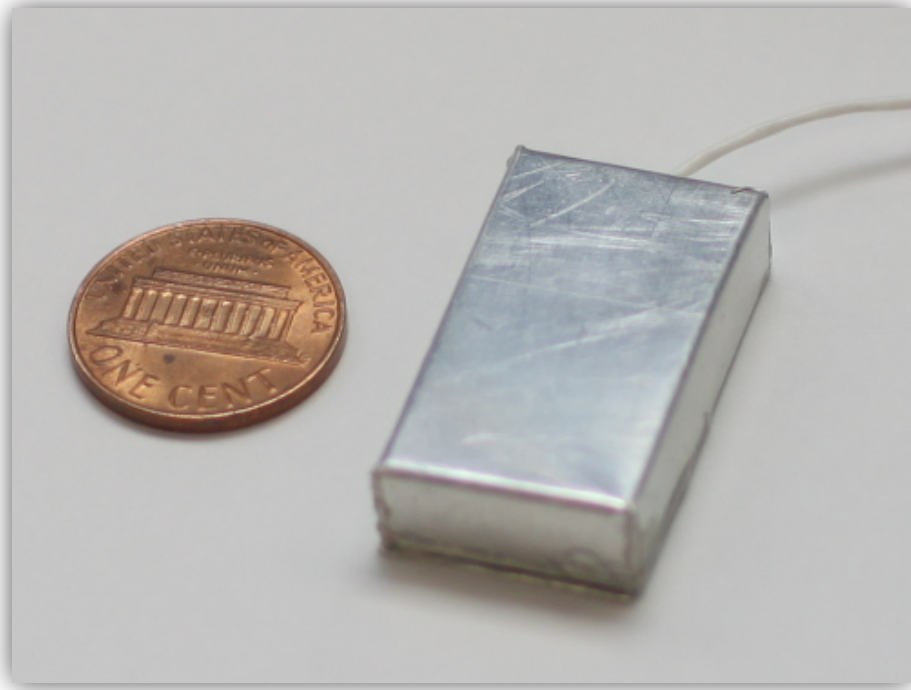


Figure 3.3 Prototype compared with a penny

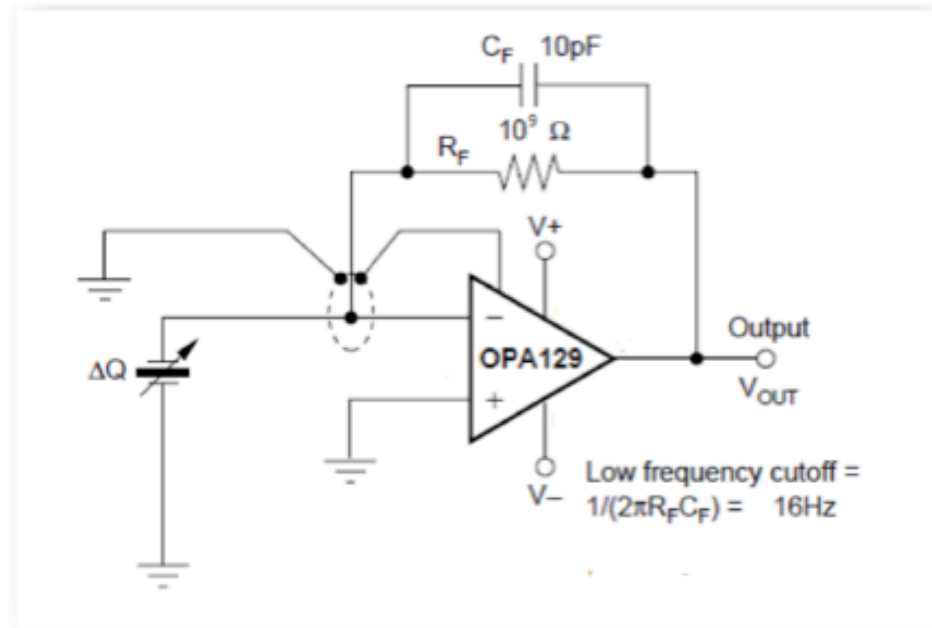
3.3.1 Signal processing circuit

As we discussed in session 2.5.1, charge amplifier is usually used for amplifying the signal from high capacitance source such as piezoelectric transducers. OPA 129 from Texas Instrument (TI) is an ultra-low bias current monolithic operational amplifier. It uses an advanced geometry dielectrically-isolated FET (Difet[®]) inputs to eliminate isolation-junction leakage current and reduce the input bias current by a factor of 10 to 100. The ultra-low current helps to reduce voltage drift and saturation which makes it a perfect candidate for amplifying high impedance signal. Therefore, a charge amplifier circuit employing OPA 129 is designed with a 1G ohm feedback resistor and 10pf feedback capacitor as shown in Fig. 3.4 (a). This circuit

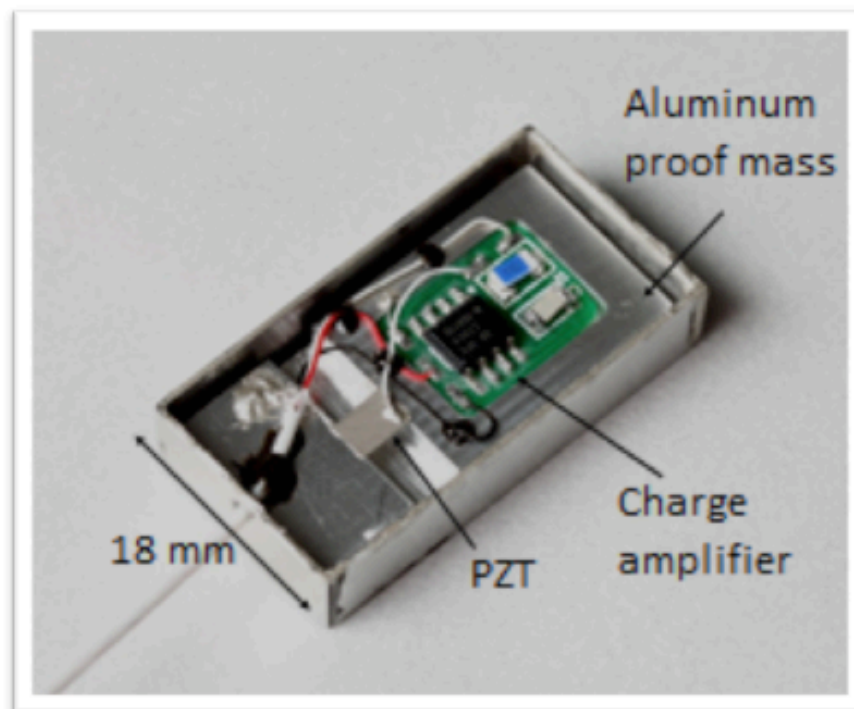
yields a low cutoff frequency of 16Hz which is satisfactory for heart and lung sound monitoring. Since the input capacitance of the piezoelectric transducer is about 1nf , the gain is estimated to be about 100.

Another important issue to note is the input guarding for ultra-low input bias current op amps. Without proper input guarding, the leakage current on the surface of circuit board is possible to exceed the input bias current of the amplifier or even 100 times higher. Therefore, we designed a guard trace to completely surround the input terminals and other circuitry connecting to the inputs of the op amp to minimize the surface leakage.

What's more, to avoid noise generated by the triboelectric effects (friction-generated charge), the PCB board with the circuit on is placed on the proof mass of the cantilever structure and shielded in the aluminum package as shown in Fig. 3.4 (b). Finally, the output of the amplifier is recorded by a 12-bit data acquisition board (National Instrument NI 4461) and further read onto computer through NI Labview software.



(a)



(b)

Figure 3.4 (a) Amplifier circuit design (b) Inside view of the prototype with the PCB board on the proof mass

3.3.2 Resonant frequency

The frequency response of the accelerometer is shown in Fig. 3.5. The accelerometer has a resonant frequency of about 1100Hz, which is higher than the heart sound frequency range.

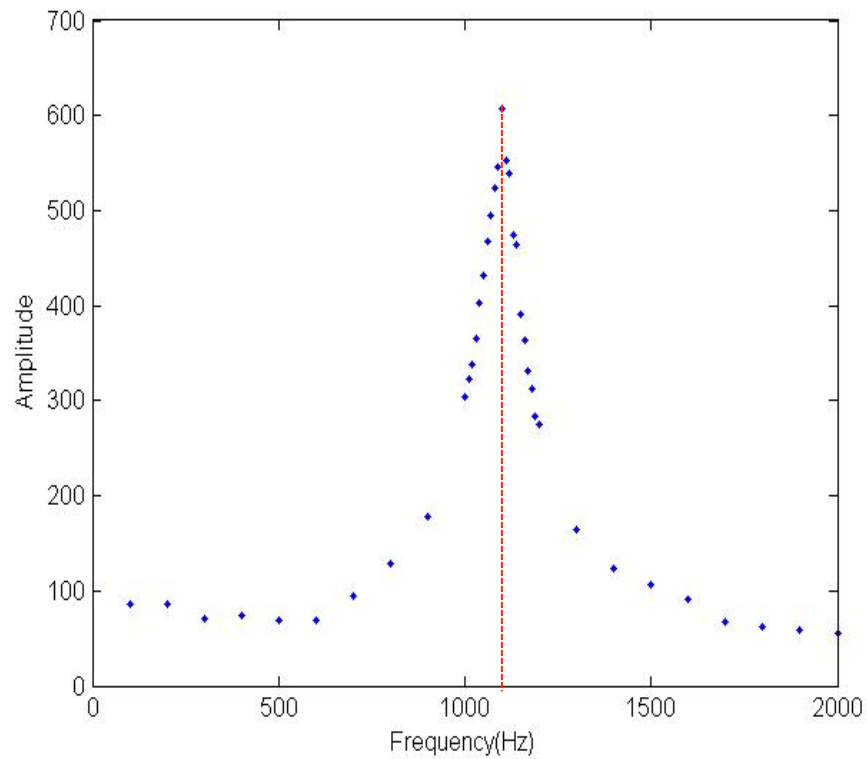


Figure 3.5 Frequency response of the accelerometer under 1 g acceleration. A resonant frequency of 1100Hz and a quality factor of 80 were measured.

3.3.3 Sensitivity

Since the packaged prototype is rectangular shape, the sensitivities are measured in x, y and z three axis as shown in Fig 3.6. While the usable sensitivity in z direction should be as high as possible, the sensitivity in the other two directions should be minimized to reduce the airborne noise. By placing the prototype on the mechanical shaker and characterized using a commercial accelerometer (Model 752A13, Endevco), the sensitivities in three axis are measured as 64.5V/g in z axis, 11.6V/g in y axis and 5.1V/g in x axis. The z axis sensitivity is dominant as desired. Since the voltage sensitivity at the input of the amplifier could be expressed as

$$S_{in} = \frac{d_{31}E_2\varepsilon_2A}{Cg} = 0.538 \text{ V/g}$$

Considering the 100× amplifier gain, the theoretical sensitivity at the output of the amplifier is 53.8 V/g which is slightly lower than the experimental value 64.5V/g in z axis. This discrepancy could be caused by the following reasons. First, the actual capacitance of the piezoelectric sheet might be reduced during the assembling which would result in a higher amplifier gain. Secondly, the actual piezoelectric coefficient might vary slightly from the product datasheet which is pretty common for piezoelectric materials because it is hard to control the consistency of the manufacturing condition. Also, the shielding aluminum box might resonant and amplify the vibration slightly.

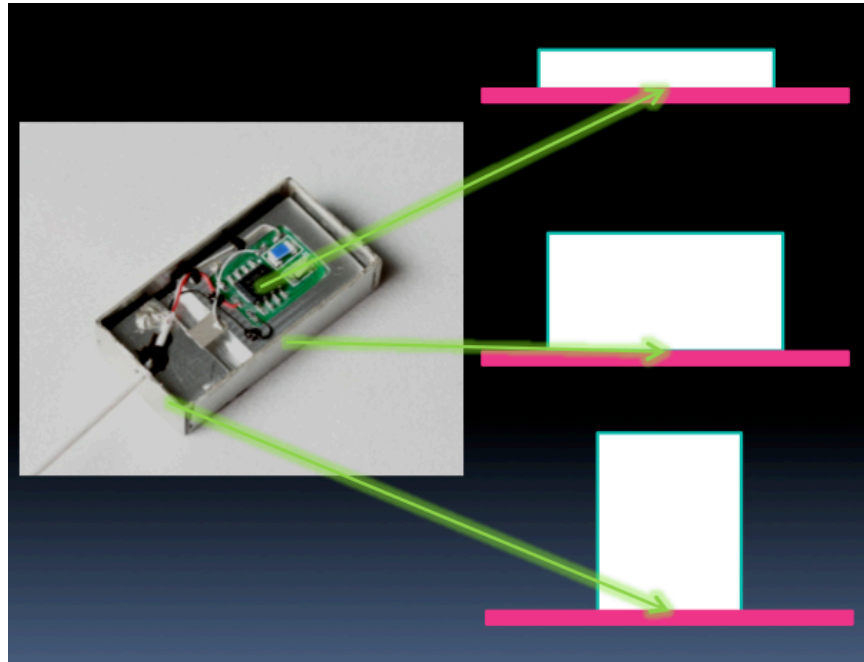


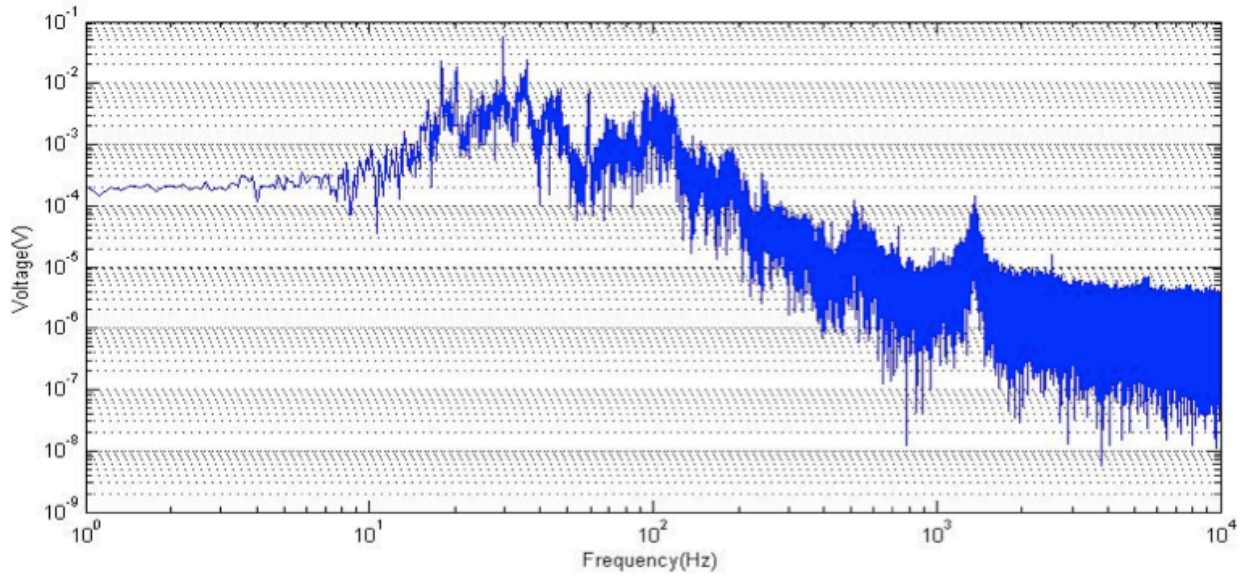
Figure 3.6 Sensor positioned in x, y, z three directions.

3.3.4 Noise

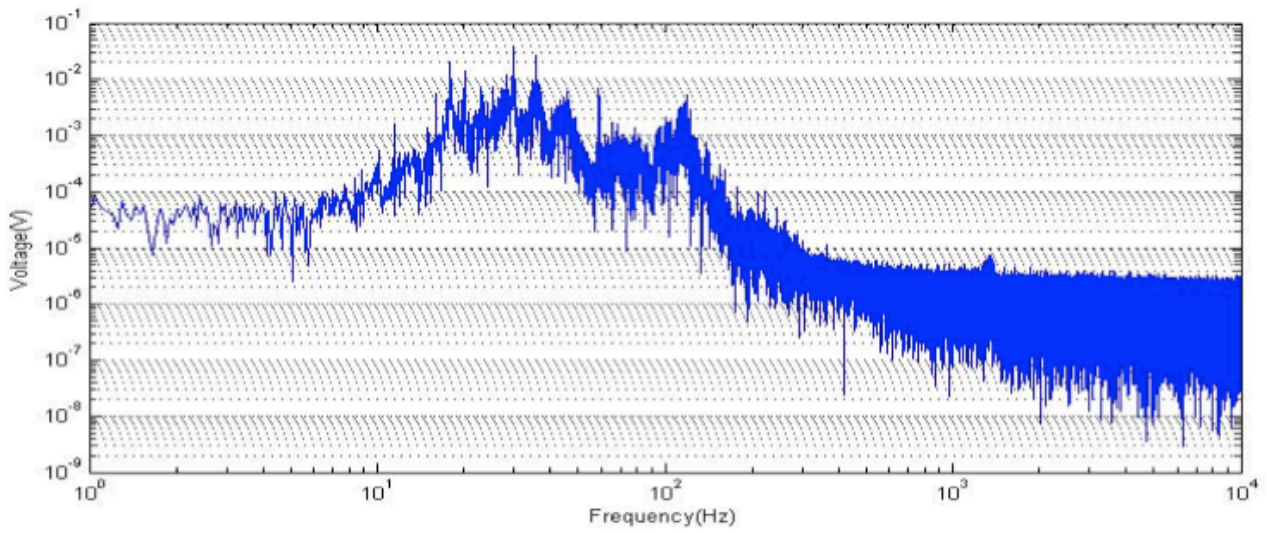
Noise is another critical issue for piezoelectric transducers. As discussed in session 2.4, there are three basic noise sources for piezoelectric accelerometers: amplifier noise, thermal electrical noise and thermal mechanical noise. In the real application, however, the noise sources are much broader. The mechanical vibration from the environment, if not isolated, is also a significant noise source to the transducer. What's, for a particular application such as heart sound monitoring, all other irrelevant vibration including breathing sound, talking, body movement and clothes friction are all considered as noise source and needs to be minimized.

In order to measure the noise level at the real operation environment as well as the true basic intrinsic noise level of the designed accelerometer, three experiments are carried out. The sensor is placed in regular lab table, in acoustic isolation room table and in acoustic isolation

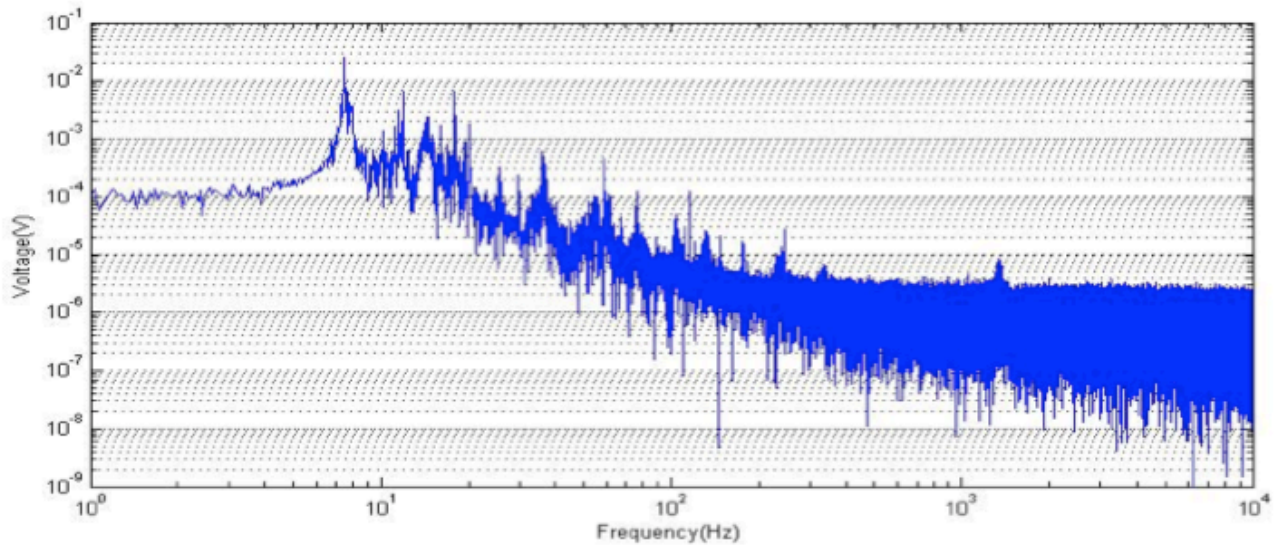
room suspended on a wire. And the respective noise power spectrum is shown in Fig. 3.7 (a), (b) and (c). As we can tell in Fig. 3.7(a), the overall noise level is the highest among the three figures. There are a lot of random noise peaks at low frequency range. And a significant peak at the resonant frequency 1100Hz. This is mainly due to the various noise sources in the testing environment such as power line, room fans, engine sounds, people talking, etc. To minimize most of the acoustic noise from the surrounding, the sensor is placed on the table in the acoustic isolation room. As shown in Fig 3.7(b), the overall noise level is lower and the peak at the resonant frequency is much smaller. However, there is still a lot of low frequency noise below 100Hz. This is mainly due to the mechanical vibration noise transmitted through the table such as building vibration. To further reduce these noises, the sensor is suspended on an elastic wire in the acoustic isolation room. As shown in Fig 3.7(c), the noise level between 10Hz and 100Hz is reduced significantly. The noise spectrum density is estimated at $3\mu V/\sqrt{Hz}$. This is still not the intrinsic noise level because of the low frequency background noise could not be totally isolated. Further noise cancellation mechanism could be employed in the signal processing to reduce the common mode background noise to reach the intrinsic noise level.



(a)



(b)

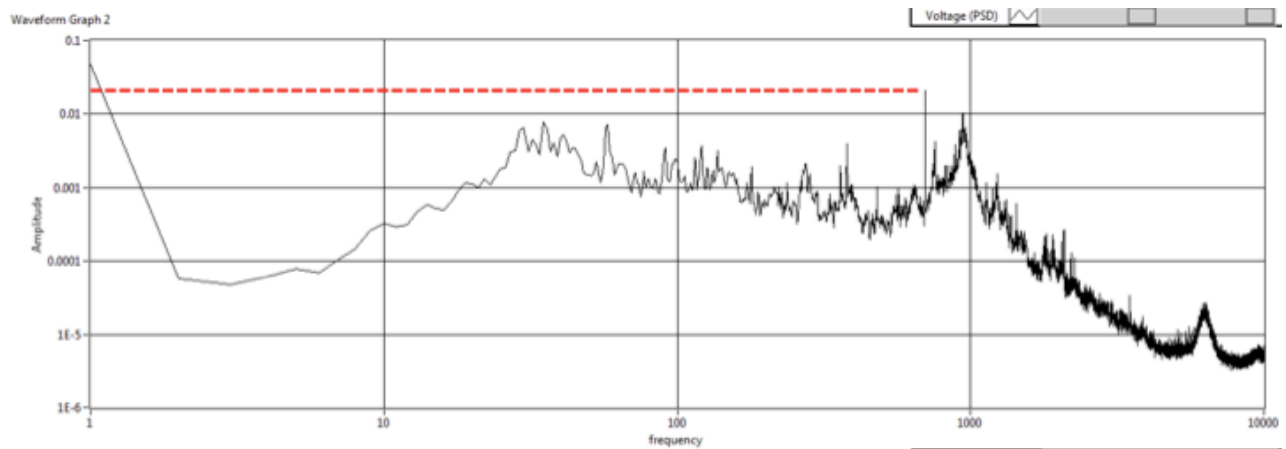


(c)

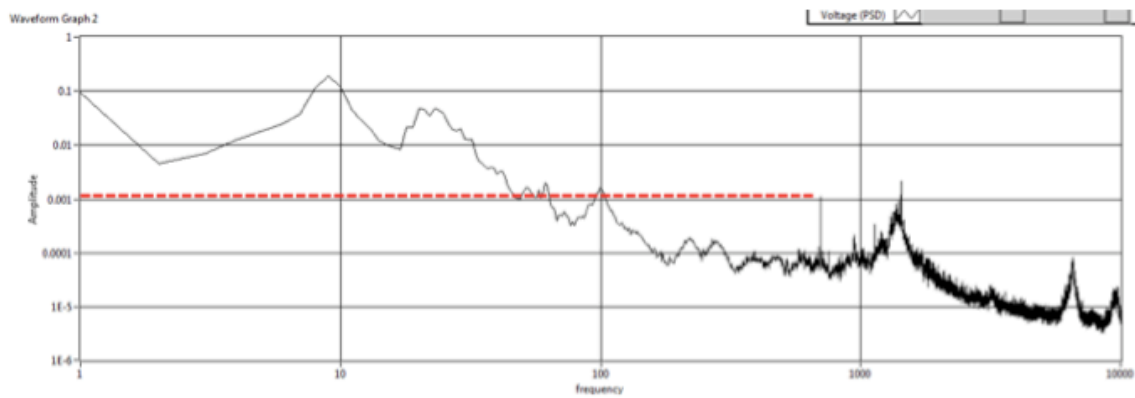
Figure 3.7 Noise in different environment (a) in lab; (b) in acoustic isolation room, sensor placed on chair; (c) in acoustic isolation room, sensor suspended in air.

Another kind of noise for the packaged prototype is the airborne noise transmitted through the aluminum package. In the heart sound monitoring, the only useful signal is transmitted through the side of the package which is attached to the skin/clothes. Therefore, it is undesirable if other sides of the package couple the airborne noise into the sensor. To test whether the package of the sensor introduces a significant level of airborne noise, the following comparison experiment is carried out. By using a speaker set at 700Hz output as a constant noise source, the sensor is first placed on the same table as the speaker, and then suspended in the air keeping the distance from the speaker unchanged. The result is shown in Fig. 3.8. The peak at 700Hz shows the responsive sensitivity of the sensor to the speaker signal. As we see, the signal amplitude transmitted through table is about 30 times higher than through air which means the

packaged sensor is much more sensitive to the signal transmitted through the contact surface than airborne noise.



(a)



(b)

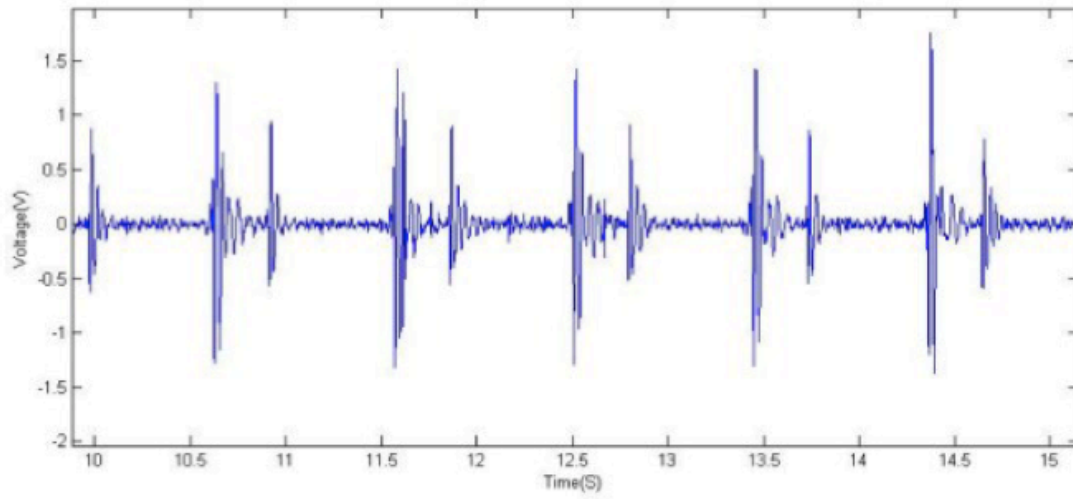
Figure 3.8 Airborne noise tested in the environment with 700Hz noise generated by speaker. The sensor is placed (a) on the table; (b) suspended in air

3.4 Preliminary tests

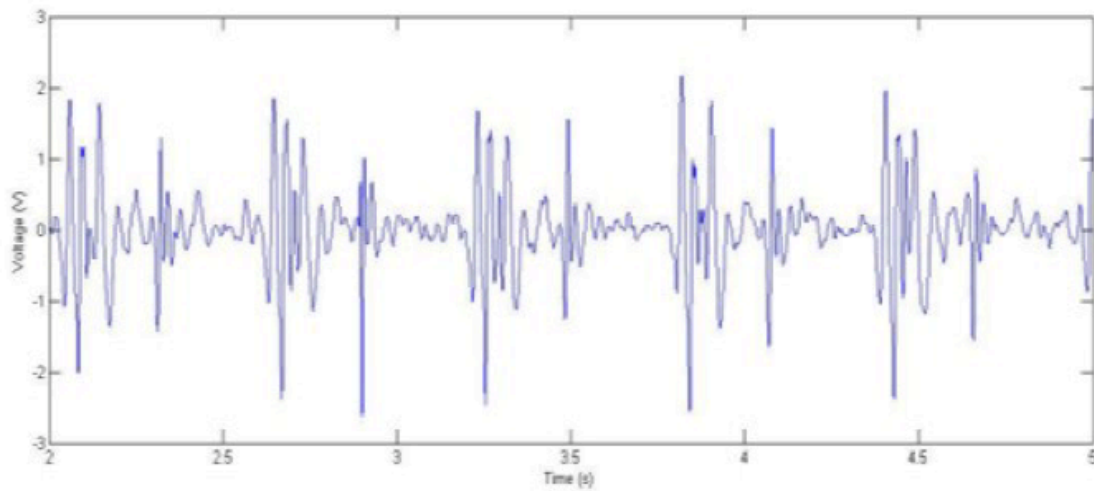
Preliminary tests for recording both heart and lung sounds are carried out on healthy volunteers and heart failure patients in a regular laboratory environment. The data from the sensor is transferred to a PC through data acquisition board (NI USB 6210) and further processed by LabVIEW[®] and MATLAB[®]. The sampling rate is set at 2 kHz for heart sound monitoring and 4 kHz for lung sound monitoring. A comparison is made between the asymmetrical gapped accelerometer and a high-end electronic stethoscope (3M Littman 3200) in detecting heart and lung sounds. For both accelerometer and stethoscope data, a filter with a bandwidth from 20 Hz to 500 Hz is applied to extract the heart sound and a filter with a bandwidth from 350 Hz to 1000 Hz is applied to extract the lung sound. The device location is chosen to be the 5th intercostal space to the left just lateral to the sternum (right AV auscultation) for cardiac signal detection and a right anterior intercostal space above the level of the 3rd rib for respiratory signal detection.

Figure 3.9 shows the visible differences in signal quality between the asymmetrical gapped accelerometer and the electronic stethoscope in cardiac sound detection. The signal-to-noise ratio of the designed sensor is about two times higher. Fig. 3.10 plots the lung sounds recorded by our sensor and the electronic stethoscope for regular gentle breathing. Note that lung sounds are much weaker than heart sounds and thus are more difficult to detect, especially for a gentle breathing. As can be observed in Fig. 3.10 (b), the lung sound can hardly be distinguished in the signals captured by the stethoscope. In comparison, the lung sound can be clearly detected by our sensor. It is also worth noting that these measurements were carried out in a regular laboratory environment full of air-borne noises. It can be observed that our sensor is

not very sensitive to air-borne noise. This preliminarily demonstrated that the designed accelerometer has satisfactory performance in monitoring heart and lung sound.

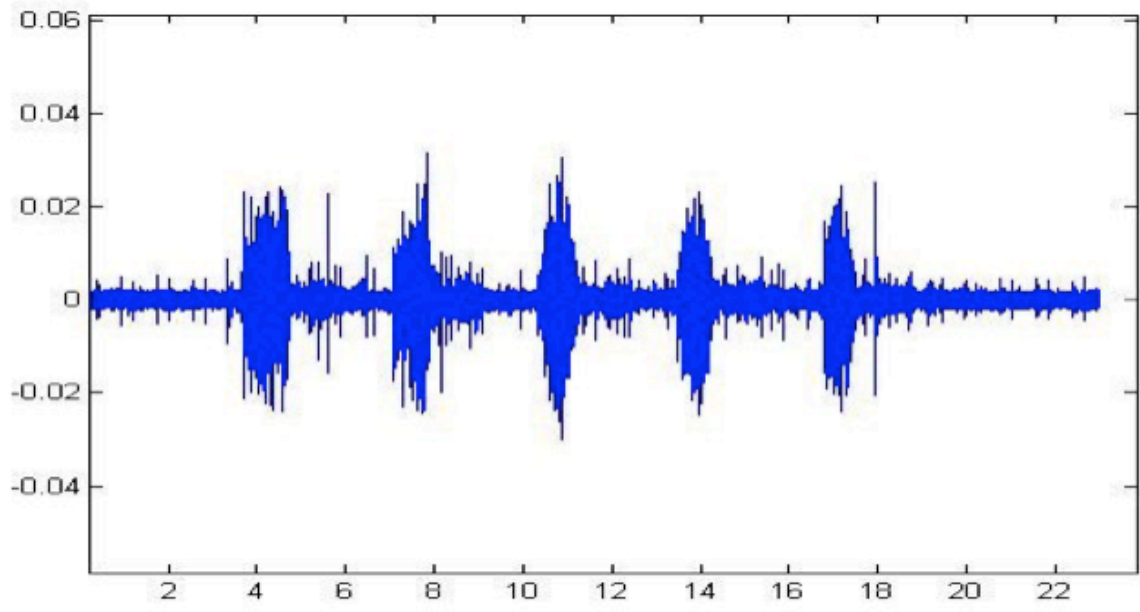


(a)

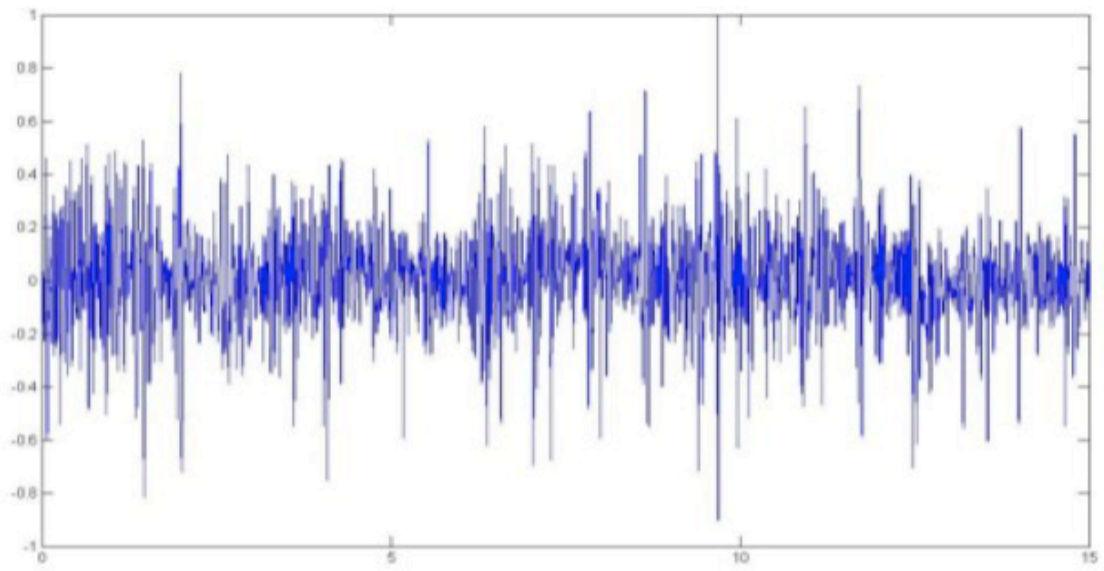


(b)

Figure 3.9 Sample waveforms of heart sound: (a) detected by our new accelerometer; (b) detected by an electronic stethoscope.



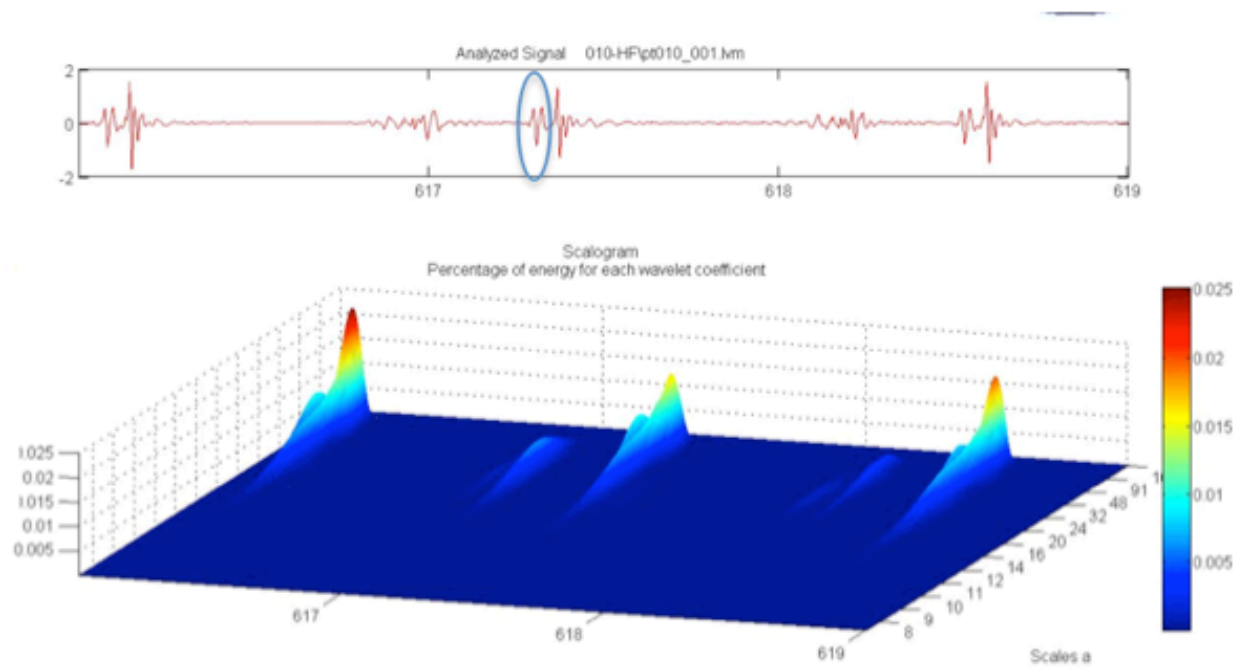
(a)



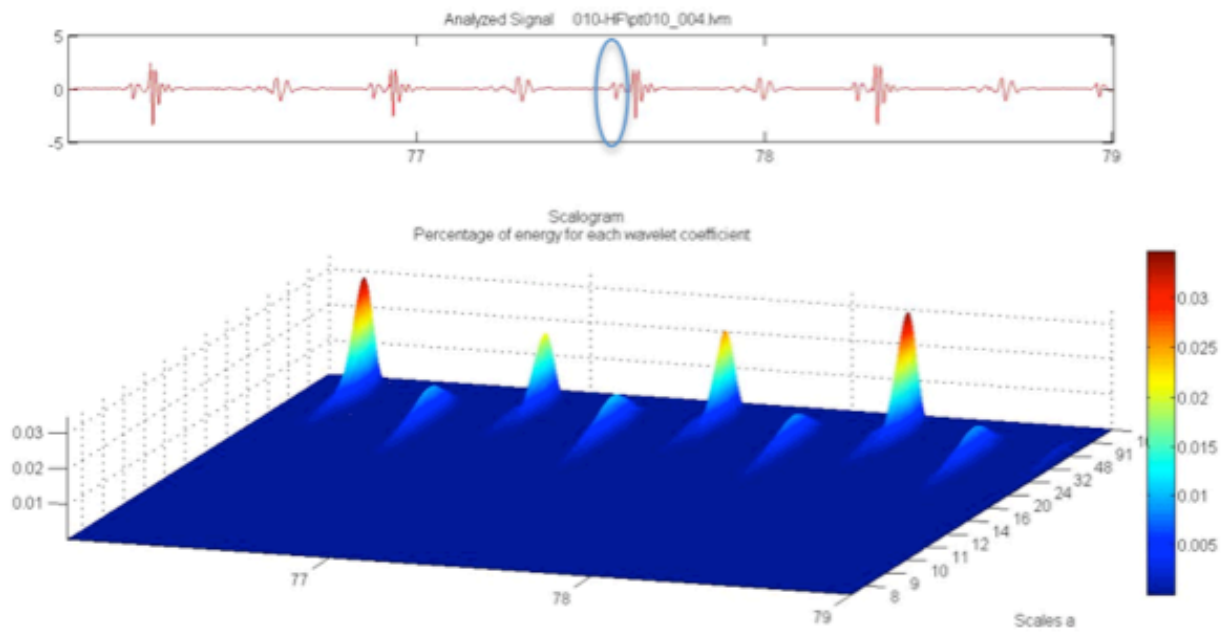
(b)

Figure 3.10 Sample waveforms of lung sound: (a) detected by our new accelerometer; (b) detected by an electronic stethoscope.

In order to demonstrate the clinical information the sensor could potential provides, it is used to record the heart sounds of heart failure patient before and after receiving treatment. The comparison heart sounds are presented in Fig. 3.11. Besides the time domain waveform, a wavelet analysis is also presented to show the frequency components of the heart sounds. Unlike healthy people who only have two heart sounds S1 and S2 within one heart beat cycle, heart failure patient also has the third heart sound S3 which is normally diminished during the recovery. Therefore, S3 could be used as a signature signal for evaluating the heart failure development. In Fig. 3.11 (a), the S3, which is marked with blue circle, is more prominent compared with the corresponding signal in Fig. 3.11 (b). This change could also be seen on the wavelet analysis graph. This result could be explained by the fact that the heart function has been improved after receiving the treatment. From the proof of concept experiment, we demonstrated the potential of such heart sound measurement being used to evaluate the heart failure recovery and the effectiveness of the treatment.



(a)



(b)

Figure 3.11 Sample waveforms of heart sounds of heart failure patient: (a) before treatment; (b) after treatment

3.5 Summary

Meso scale piezoelectric accelerometer based on gapped cantilever structure is developed in this chapter. It is designed to for the purpose of continuously recording cardio and respiratory sound which could provide critical clinical information. The theoretical design is further verified by the finite element simulation. The machined prototype is successfully characterized, and the experimental result agrees well with analytical and simulation result. Moreover, a comparison test is carried out by using the developed accelerometer and the commercial digital stethoscope to monitor heart sound on a healthy individual simultaneously. The result shows that the developed accelerometer yields a much better signal to noise ratio. The sensor is also briefly tested on heart failure patient to acquire comparison heart sounds before and after treatment in order to demonstrate its potential for evaluating heart failure recovery process.

There are also a few remaining tasks to be addressed in the future work. For example, the mass loading effect should be studied and considered in the future design for coupling the physiological acoustic source more effectively to the sensor. Noise corruption is another important issue to be addressed. For example, the friction noise between the sensor surface and the clothes could be reduced by applying either low friction film or super high friction gel on the sensor surface. What's more, removing artifact noises such as speaking sound, body movement through advanced signal processing techniques is also critical for recovering useful information

in the acquired signal. Finally, more quantitative analysis on categorizing different information in heart sound also needs to be further studied.

CHAPTER 4 LOW FREQUENCY VIBRATION SENSING AND BCG MONITORING

4.1 Introduction

Low-frequency vibration sensors are of great interest for various applications such as structural health monitoring, landslide monitoring, earthquake monitoring, oil exploration, and biomedical monitoring[139-142]. There are already many sensors developed to detect low-frequency vibrations by measuring displacement, velocity or acceleration [12, 139, 143-145]. They are light in weight, built compactly and can save the power consumption of measuring instrument.

However, there is a design tradeoff between the weight of the sensor and its minimum detectable acceleration. Some researchers developed light weight MEMS accelerometers with limited resolution[146-148]. While others try to decrease the noise floor by using a large size and heavy weight system. For example, the vibration sensor comprised of a cylindrical shape with 65 mm diameter, 70 mm height, and 800 gm weight is developed to achieve higher resolution.

Therefore, an opportunity exists for a lightweight accelerometer with low noise floor at low frequency to be developed. In this chapter, an accelerometer based on cascaded structure is designed and tested for this purpose.

4.1.1 Ballistocardiograph (BCG) monitoring

Ballistocardiograph (BCG) refers to the measurement of the repetitive human body displacement caused by the heart beat and blood ejection [149]. BCG provides some valuable information about cardiovascular function, such as the contractility of myocardia [150].

Compared with other technologies, the main advantage of BCG is that it can provide an unobtrusive way to monitor the heart condition since sensors do not need to be in direct contact with the human body. In this sense, it is more convenient to use than wearable sensors. Historically, BCG was measured using large-size equipment such as a swing bed or table [151]. Recently, piezoelectric films, which function as force sensors, have been embedded in chairs to detect BCG signals [152]. A modified commercially available weight scale has been used to acquire BCG [153].

Accelerometers have also been used for BCG measurement. For example, He et al. used a 3-axis MEMS accelerometer (Bosch BMA180) to measure BCG on head [29]. Prisk et al. reported the measurement of 3D BCG using a 3D accelerometer during a space flight [76]. It was reported that the greatest BCG acceleration was about 7 mg in the head to foot direction. The acceleration along the dorso-ventral axis is about 4.3 mg. The majority energy of BCG signal is in the infrasound range. Therefore, accelerometers for BCG need to have good performance at low frequency band. It is also possible to detect BCG by attaching an accelerometer to a chair or bed, thus enabling un-obtrusive cardiovascular monitoring.

4.1.2 Seismic monitoring

Accelerometers also provide the high quality seismic measurement to evaluate the viability of new wells in oil and gas industry. While the traditional geophones are widely used in the industry, its performance rolls off at frequency below 10Hz[141]. In comparison, low frequency accelerometers are light in weight, more compact and consume less power. Moreover, their small distortion in phase spectrum and linear response in low frequency band are greatly desired in ground motion measurements as well. By utilizing a high performance low frequency

accelerometer, the wasted cost of locating and drilling nonproductive wells could potentially be reduced.

4.2 Design

4.2.1 Structure

A low-frequency vibration sensor based on a cascaded asymmetric-gapped cantilever structure has been developed. The basic asymmetric-gapped cantilever has been previously demonstrated for high-performance accelerometers [86, 154]. Such a structure is able to increase the sensitivity and improve the energy efficiency significantly [85, 155]. However, one limitation is that the gapped cantilever tends to have a high spring constant which is not desired for low frequency sensing. The effective spring constant of the basic asymmetric-gapped cantilever can be estimated by the following formula:

$$k \approx \frac{4E_2 A_2 d_2^2}{l(l + l_{pm})^2} \quad (4.1)$$

For low-frequency vibration sensing, the spring constant needs to be reduced to achieve a high sensitivity. Based on Eq. (45), this in theory can be accomplished by reducing the cross sectional area of the sensing beam A_2 . Practically, this will make the manufacturing or fabrication of the sensor challenging and pose reliability issues. Alternatively, we can increase the cantilever length l . However, this will make the shear deformation of the asymmetric-gapped cantilever dominant and reduce the energy efficiency. To address this issue, we developed a

simple but effective cascaded asymmetric-gapped cantilever to lower the spring constant while maintaining the dominance of pure bending. A design based on a four-stage cascaded gapped cantilever is schematically illustrated in Fig. 4.1. Both the top and bottom beams are divided into two splits placed apart from each other to subdue the undesirable torsional and lateral movements.

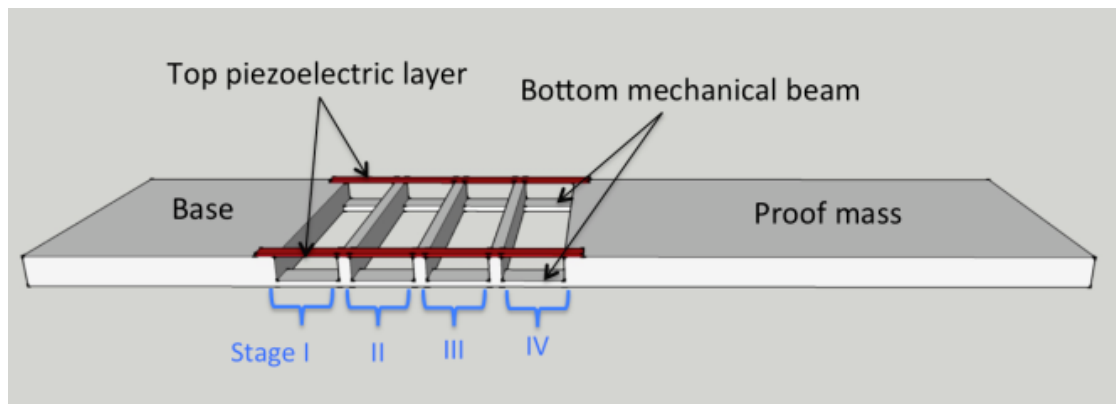


Figure 4.1 Schematic of a low-frequency accelerometer based on a four-stage cascaded asymmetric-gapped cantilever structure.

To simplify the analytical model, we neglect the shear bending of the cantilever, the deformation of the proof mass and the supporting ridges, the mass of the beams and supporting structures, and assume the mass is concentrated at the center of the proof mass. With these simplifications, the resonant frequency is approximately:

$$f_0 = \frac{1}{2\pi} \sqrt{\frac{k_P}{m}} \quad (4.2)$$

It is expected that the real resonant frequency will be lower than the value predicted by Eq. (4.2) because of the simplifications.

The voltage sensitivity can be calculated by

$$S_V = \frac{V}{a} = \frac{\lambda d_{31} E_2 t_2}{\epsilon_3 \epsilon_0} S_2 \quad (4.3)$$

where λ is the ratio of effective piezoelectric beam length and the total length, d_{31} is the transverse piezoelectric coefficient, ϵ_3 is the relative dielectric constant of PZT in direction 3, S_2 is the normal strain given by Eq. (4.3).

For a specific design with the parameters summarized in Table 4.1, the estimated theoretical resonant frequency is 109Hz, and the voltage sensitivity is 12.1V/g.

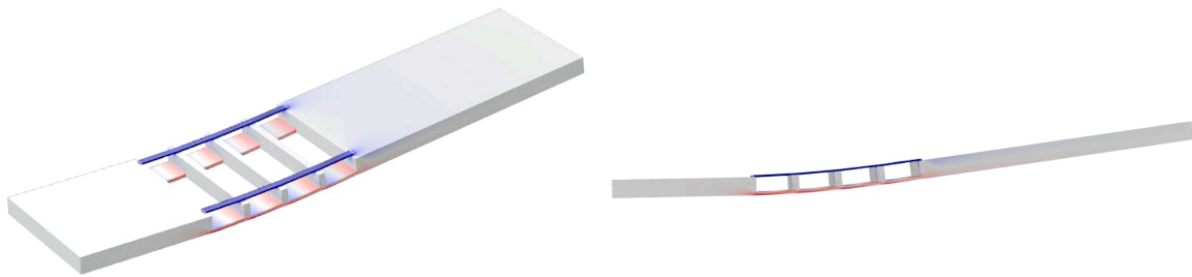
Table 4.1 The prototype design parameters

	Top beam	Bottom beam	Proof mass
Length (mm)	10	10	72
Width (mm)	4	18	39
Thickness (mm)	0.5	1	5.1
Material	PZT	Aluminum	Aluminum
Young's modulus (GPa)	66	69	69
Density ($\times 10^3$ kg/m ³)	7.8	2.7	2.7

4.2.2 FEA simulation

Finite Element Analysis (FEA) simulation was carried out to study the performance of the cascaded asymmetric-gapped cantilever using COMSOL 4.3a. For the design specified in Table

4.1, the simulated resonant frequency and voltage sensitivity are 88 Hz and 9.9 V/g respectively assuming perfect bonding between the piezoelectric beams and the aluminum substrate and ridges. As expected, the resonant frequency from FEA simulation is lower than the value calculated from Eq. (4.2). In order to illustrate the advantage of using the cascaded structure in low-frequency sensing, a single stage gapped cantilever with the same resonant frequency is also simulated for comparison. Fig. 4.2 (a) and (b) show the bending shapes of the first resonant mode of both structures. As observed in Fig. 4.2 (a), the cascaded structure is dominated by pure bending which is the desired bending shape. In contrast, the deflection of the single stage structure in Fig. 4.2 (b) is dominated by shear bending which does not generate output voltage effectively. Fig. 4.2 (c) also shows the second and third resonant modes of the cascaded cantilever at 403 Hz and 620 Hz, respectively, which are far away from the fundamental mode due to the split beams.



(a)

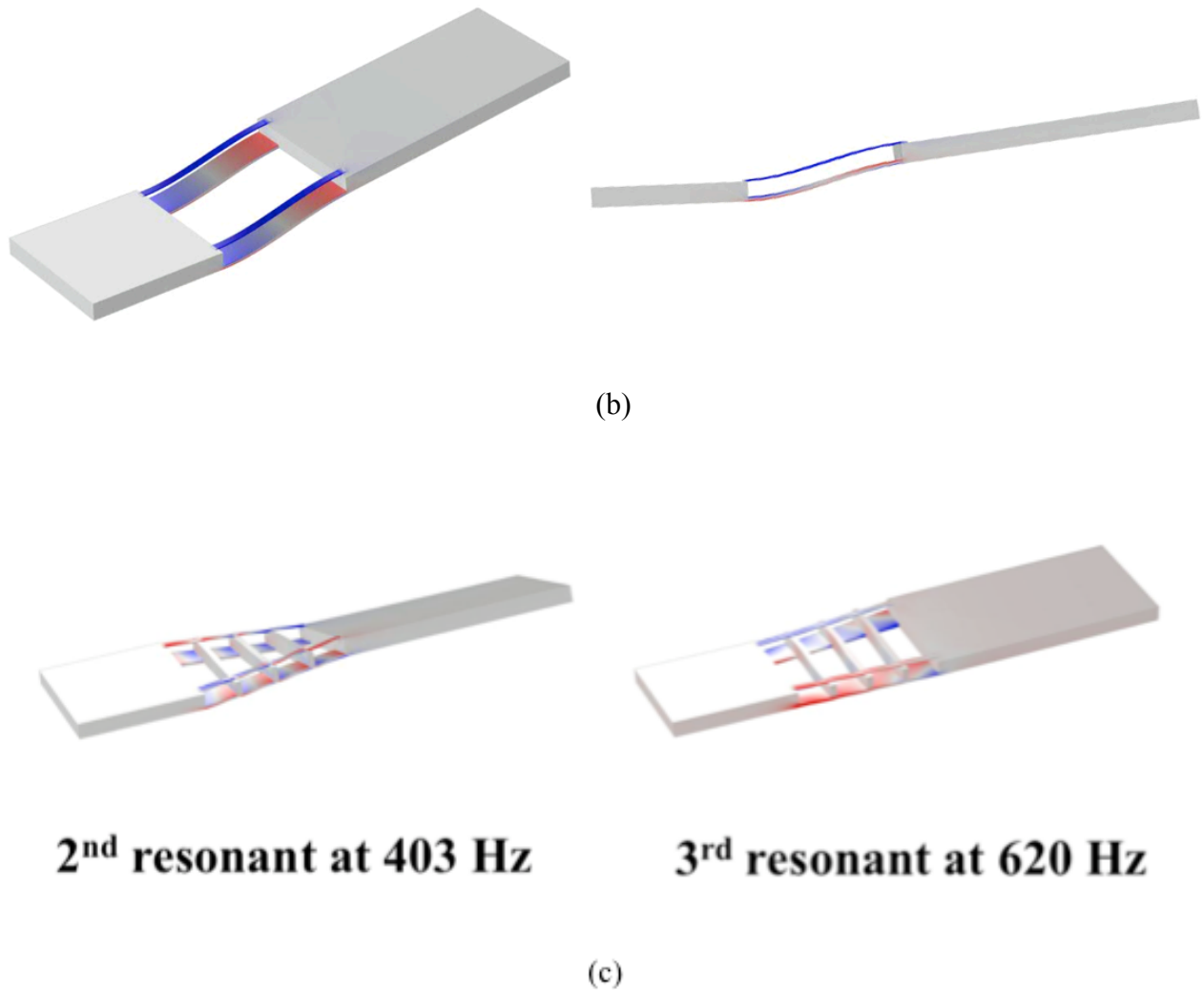


Figure 4.2 (a) The first resonant mode of a four-stage cascaded asymmetric-gapped cantilever; (b) the first resonant mode of single stage asymmetric-gapped cantilever; (c) the second and third resonant modes of the cascaded asymmetric-gapped cantilever.

4.3 Characterization

A prototype device with the design specified in Table 4.1 was constructed and characterized. An aluminum piece was machined to form the proof mass, bottom mechanical beams and the supporting ridges of the device. Ceramic PZT (Lead zirconium titanate) sheets (Piezo Systems,

#PSI-5A4E), which function as strain sensing element, were bonded to the machined aluminum substrate using adhesive epoxy (3M DP-100-CLEAR). Note that the epoxy has a much lower Young's modulus compared with PZT and aluminum. For the frequency response measurement, the device was mounted on a mechanical shaker (Labworks, Inc ET-126B-1) together with a reference accelerometer (Endevco, Model 4416B) to calibrate the acceleration as shown in Fig. 4.3. The output voltage of PZT sheets was recorded using a data acquisition board (National Instrument, USB 6210) with a sampling rate of 2000Hz as the vibration frequency swept from 10 Hz to 130 Hz.

4.3.1 Resonant frequency and sensitivity

The acquired experiment data was plotted in Fig. 4.4 and fitted with the transfer function of a second order system. The fitted resonant frequency f_0 and the quality factor Q are 53.6 Hz and 20, respectively. The low frequency sensitivity (before any amplification) is estimated to be 8.4 V/g. Note that the experimental resonant frequency is lower than the original simulation result. We believe that it is mainly because the epoxy layer between the PZT and aluminum has a much lower Young's modulus and thus reduces the resonant frequency [156]. To verify this hypothesis, we studied a revised FEA model with a 100 μm thick epoxy layer with 0.3 GPa Young's modulus added at all contact areas between PZT and aluminum. The simulated resonant frequency and the voltage sensitivity of the new model are 57 Hz and 8.9 V/g, which are much closer to the experimental values. This illustrates that the epoxy layer does have a significant impact on the sensor performance.

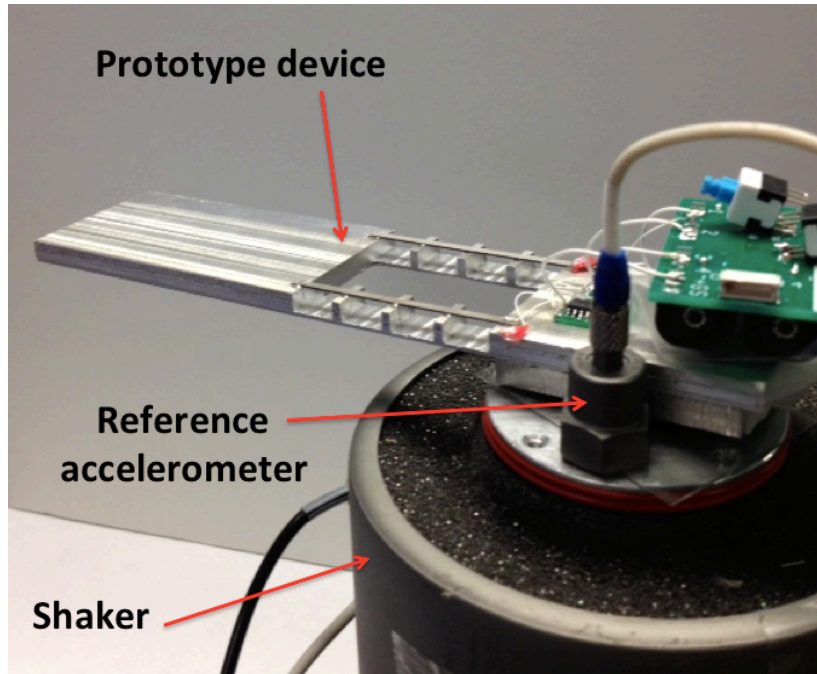


Figure 4.3 Prototype device mounted on a shaker together with the reference accelerometer

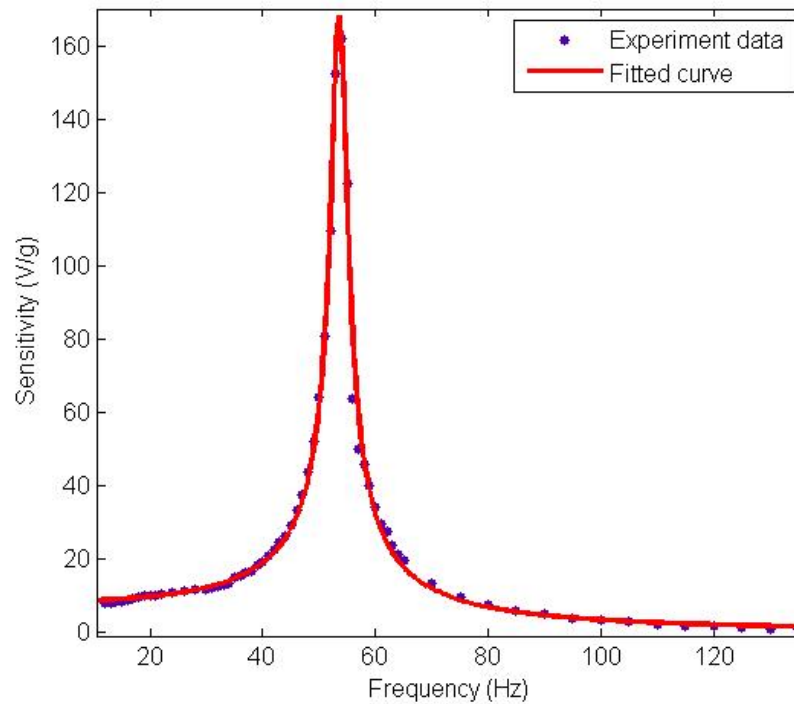


Figure 4.4 Frequency response of the designed accelerometer.

4.3.2 Noise

The noise floor, which determines the minimum detectable acceleration, is a critical parameter for the detection of weak vibrations. To measure the noise floor, two identical charge amplifiers using TI opa129 were constructed to amplify the output of the two piezoelectric beams. The feedback resistor and capacitor of the charge amplifier are $1\text{G}\Omega$ and 50 pF , respectively, yielding a lower 3dB frequency of 3.2Hz . There are mainly three noise sources for the piezoelectric accelerometer: the amplifier noise, the thermal-mechanical noise and the dielectric noise of the piezoelectric material. Considering these three noise sources, the noise equivalent acceleration is calculated by [90]

$$a_n = \sqrt{4k_B T \left(\frac{2\pi f_0}{mQ} + \frac{\eta}{2\pi f S_V^2 C} \right) + \left(\frac{e_n}{S_V} \right)^2} \quad (4.4)$$

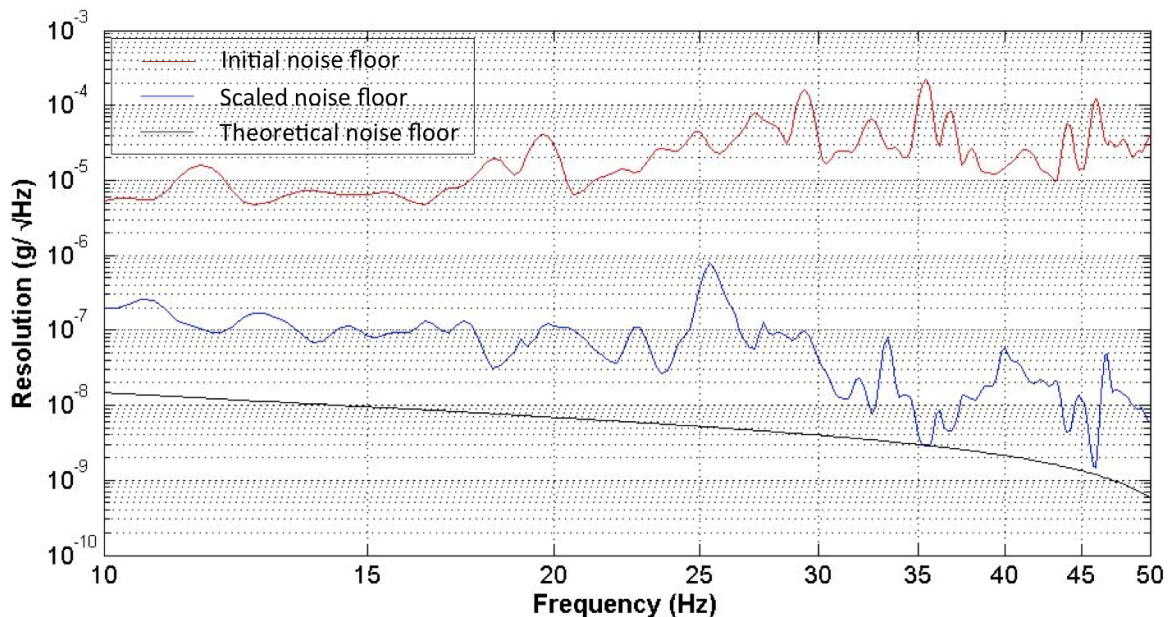
where k_B is Boltzman's constant, $T = 300$ °C is the temperature, $m = 40$ g is the proof mass, $f_0 = 54$ is the resonant frequency, $Q = 20$ is the quality factor of the harmonic oscillator, f is the vibration frequency, $C = 3.1$ nF is the capacitance of the transducer, $\eta = 0.02$ is the loss angle of the PZT [12], e_n is the noise spectrum density of the TI opa 129 amplifier and $S_V = 8.4$ V/g is the transducer's voltage sensitivity. Note that the amplifier noise is the dominant noise source in the low frequency range for this specific design. Based on Eq. (4.4), the theoretical noise equivalent acceleration is calculated and plotted in Fig. 4.5 (a).

The voltage noise spectrum of the accelerometer was measured using a NI-USB 6210 data acquisition board. The noise equivalent acceleration (NEA) was obtained by dividing the voltage noise spectrum by the fitted voltage sensitivity. In order to reduce the background noise interference from the environment, the sensor was wrapped with foams and placed on a vibration isolation table. However, the background seismic noise is still well above the theoretical noise floor of the sensor as shown in Fig. 4.5 (a). Therefore, we employed a coherence scaling method to cancel the background noises [157]. This method takes advantage of two identical sensors exposed to the same background stimuli. The basic assumption is that the external noises generate coherent outputs on both sensors whereas the intrinsic noises generate un-correlated outputs. A much lower NEA can be calculated by removing the coherent component from the original signal [157].

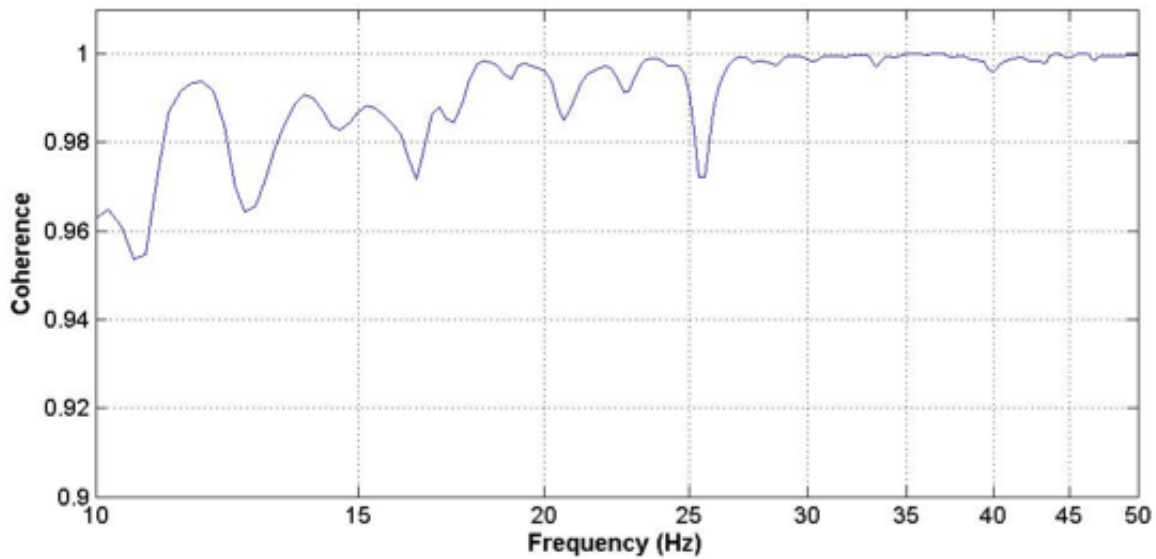
Since the two top sensing beams were designed to be identical and should vibrate in the same

mode below the resonant frequency, they were taken as the two inputs for the scaling method. As shown in Fig. 4.5(b), the coherence of two piezoelectric beams is above 0.95 between 10 Hz and 50 Hz. Therefore, significant portions of the original NEA are correlated background noise and can be removed effectively by this method. The scaled NEA in Fig. 4.5 (a) is much lower than the original measured NEA. However, the outputs of two PZTs also have un-coherent external noises which cannot be cancelled by this method. Therefore, the scaled NEA is still higher than the theoretical noise floor. The dips on the scaled NEA curve actually provide better approximation of the intrinsic noise floor. For example, at 35 Hz, the scaled NEA reaches the theoretical intrinsic value. The dip at 46 Hz is close to the intrinsic noise as well.

One possible source of un-correlated noises at the low-frequency range could be drifting noise of amplifier circuits. With a better electronic design, we believe that the drifting noise can be significantly reduced.



(a)



(b)

Figure 4.5 (a). Noise equivalent acceleration of the designed accelerometer. The initial measured NEA, the NEA scaled by the coherence and the theoretical noise floor are plotted for comparison.

(b) Coherence between the two piezoelectric sensing beams

4.4 Preliminary tests

The prototype device was evaluated for a real low-frequency sensing application: ballistocardiograph (BCG) monitoring. BCG is a non-invasive technique for assessing the cardiac function. It measures the movements of the body caused by the momentum of blood in the arterial system due to cardiac contraction [150, 158]. Because the BCG signal is relatively

weak compared with electrocardiogram or heart sound and the power is mainly below 20 Hz, recording BCG requires a low-frequency accelerometer with ultra-high sensitivity. In this experiment, the sensor was mounted under the seat frame of a regular office chair to monitor the BCG signal of the subject sitting on it. A heart sound sensor was attached to the subject's chest to monitor the heart sound simultaneously [154]. The recorded BCG signal was filtered by a 20 Hz low pass filter in LabVIEW. Fig. 4.6 (a) shows a representative portion of the BCG measurement. The BCG signal can be clearly identified and further verified by the corresponding heart sound signal in Fig. 4.6 (b). One representative BCG cycle in Fig. 4.6 (c) was enlarged to show the details of the signal and compared with a theoretical BCG signal [159, 160]. The extrema of the BCG waveform are denoted with letters F, G, H, I, J, K, L, M and N which matches the theoretical BCG waveform and its components very well. These components of BCG waveform contain important information on the cardiac activity. For example, it could be used for measurement of systolic force (F) and minute cardiac force (MF) [161]. Studies also suggest that BCG can be used as a low-cost prescreening device in cardiology practice or clinical settings to avoid performing more expensive and time-consuming diagnostic techniques and as an unobtrusive technology for the management of cardiovascular disease at home [150, 158].

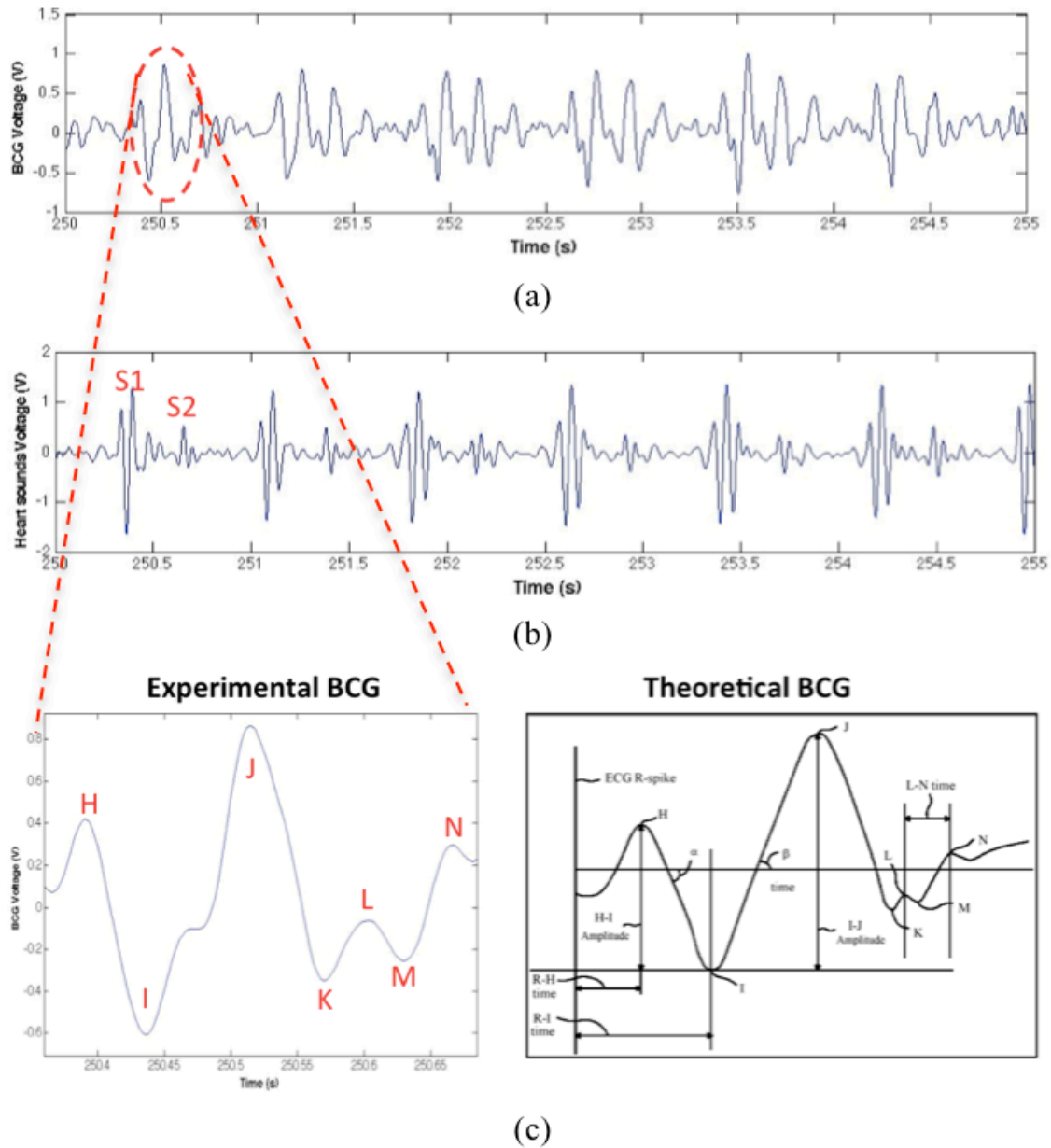


Figure 4.6 (a) A representative portion of the experimental BCG signal acquired by the low-frequency vibration sensor; (b) The corresponding heart sound signal with first heart sound (S1) and second heart sound (S2) denoted; (c) One BCG cycle was enlarged to show the details of the signal and compared with a theoretical BCG signal. The extrema of the BCG waveform are denoted with letters F, G, H, I, J, K, L, M and N.

4.5 Conclusion

A low-cost and high-performance low frequency vibration sensor based on a cascaded asymmetric-gapped cantilever structure has been successfully demonstrated. The cascaded structure effectively reduces the spring constant and increases the sensitivity, while simultaneously minimizing the shear bending of the cantilever. A proof-of-concept prototype was constructed and tested. With a proof mass weight of 40 g, the sensor achieved an NEA close to theoretical value at 35 Hz. In the experiment, the coherent background noise was reduced significantly using the coherence method. The prototype sensor has successfully acquired clear BCG signals.

In the future research, more study will be carried out to eliminate the low-frequency drifting noise of amplifiers to reach the theoretical noise floor. New bonding methods such as solder bonding will be investigated as well.

CHAPTER 5 A WIDEBAND VIBRATION ENERGY HARVESTER BASED ON A FOLDED ASYMMETRIC-GAPPED CANTILEVER

5.1 Introduction

With recent advances in low power electronics, harvesting useful energy from the ambient environment to power wireless sensors has attracted a lot of interests. Among different approaches, vibration energy harvesting is a popular choice since ambient mechanical vibration is ubiquitous. By converting vibration energy into electricity, a VEH can serve as a continuous power source to replace batteries in various wireless sensing applications. Currently most VEHs (typically a spring-mass system) are designed to operate at one resonant frequency, leading to a narrow operating bandwidth. However, ambient vibration is normally wideband and time-varying. This makes the vibration energy harvesting very challenging because the VEH's performance drops sharply when the frequency of ambient vibration deviates from VEH's resonant frequency. Furthermore, many VEHs do not generate an output voltage much larger than the threshold voltage of the rectifier diodes, thus resulting in significant energy loss during the rectification process. Due to these reasons, vibration energy harvesting so far has not been widely used for practical applications.

A number of methods have been proposed to broaden the VEH's operation bandwidth. One simple approach is to use multiple and independent spring-mass systems which have different resonant frequencies [162-164]. However, at every resonant frequency, only one proof mass is effectively utilized for energy harvesting. Another approach is based on resonant frequency

tuning. It can be categorized as passive or active tunings based on whether additional power is used [165]. Passive tuning by manually adjusting a movable mass or changing preload to the cantilever beam has been proposed and investigated [165-168]. Active tuning is typically realized by integrating additional actuators and can achieve real-time tuning [169, 170]. The tradeoff is a system with higher complexity and cost. Moreover, the actuators always consume power, which could be larger than the harvested power. Another popular approach is based on non-linear vibrations, such as Duffing oscillation[171-173]. For example, when the displacement is large, a double-clamped beam can enter the nonlinear Duffing oscillation region due to the stretching force in the beam [171]. Non-linear vibration can also be induced using bistable systems [174, 175]. However, the non-linear vibration only occurs under large vibration amplitude. VEH based on meander-shape piezoelectric cantilever has been studied for wide-band operation [176, 177]. Multi-mass multi-spring systems based on cascaded cantilevers have also been proposed and developed for wide band vibration operation [165, 178, 179]. For instance, a two-stage cascaded piezoelectric cantilever with two proof masses was investigated [178, 179]. The larger proof mass is placed on the first stage of the cantilever to ensure that the first two resonant modes are formed by the pure bending of the two piezoelectric segments.

In this chapter, a wideband and high-efficiency VEH based on a multi-stage folded asymmetric-gapped cantilever is proposed. The folded cantilever structure has been studied previously for vibration energy harvesting[180]. Wideband VEH based on a two-stage folded cantilever has been reported as well[181]. It is worth noting that the folded designs in [180] and [181] have shear bending modes which make it hard to predict the resonant modes and to harvest the energy effectively compared with pure bending. To illustrate this point, I simulated the PEH in Fig. 4 of [181] ($M_1=7.2\text{g}$, $M_2=16.8\text{g}$) as an example. Fig. 5.1 (a) shows the strain distribution

of the second resonant mode of this PEH. The shear bending on the main beam can be observed from the different stress polarities (blue vs. red). It can also be seen from the side view in Fig. 5.1 (b). Because the shear bending introduces both tensile/compress strain on the beam, multiple electrodes need to be used to cover tensile or compress areas separately to harvest all the energy. This will increase the complexity and cost of the whole system.

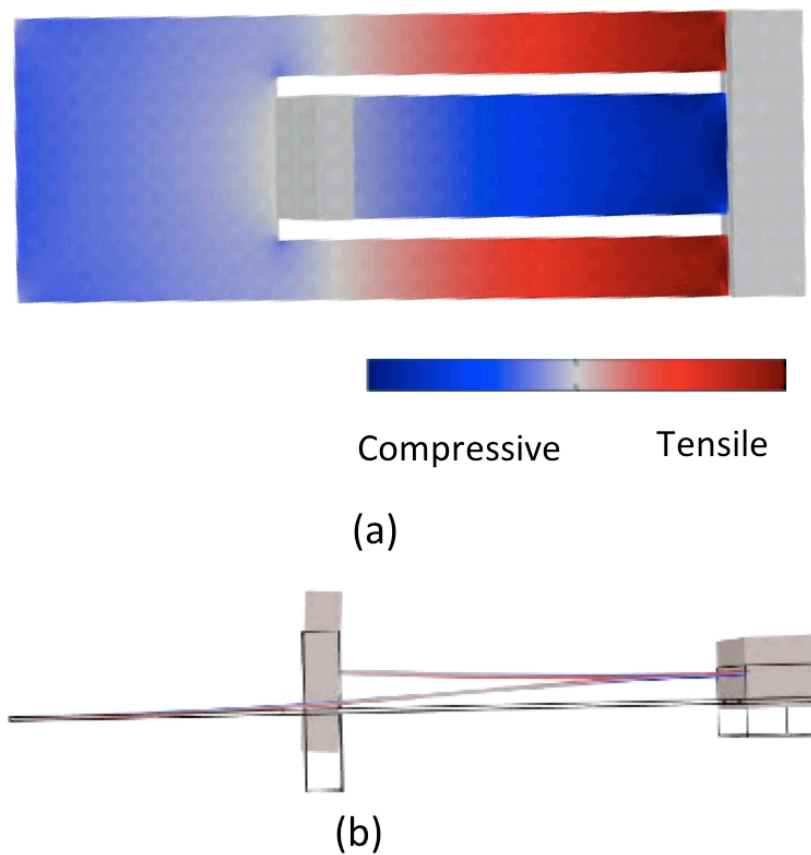


Figure 5.1 Simulation of the bending mode and strain distribution of the PEH model in paper [181] (Figure 4). (a) Top view of the second resonant mode; (b) Side view of the second resonant mode.

I reduced the system complexity and improved the energy efficiency of multi-degree-of-freedom folded structure for wideband energy harvesting, by suppressing the S-shape bending as well as using the asymmetric-gapped cantilever. As reported previously, the asymmetric-gapped cantilever maximizes the energy conversion efficiency by increasing the voltage sensitivity and concentrating the vibration energy on the piezoelectric layer [85, 182, 183]. Inheriting the advantage of the basic asymmetric-gapped cantilever, I further developed the folded asymmetric-gapped structure to enable wideband vibrating energy harvesting. This design allows the largest proof mass to be placed at the last stage of the folded cantilever structure, and further enables multiple resonant modes formed by pure bending of every stage, maximizing the energy harvesting capability.

5.2 Design

5.2.1 Structure

For proof of concept, we designed a three-stage folded asymmetric gapped structure which targets low frequency operation below 200 Hz within which there are abundant environmental vibrations. A schematic drawing of the device is presented in Fig. 5.2, and the detailed parameters of the design are listed in Table. 5.1. The overall size of the device is 5.1mm \times 120 mm \times 85 mm. The overall proof mass of stages I, II and III are 29g, 20g, and 50g, respectively. For every stage, the top piezoelectric layer, which is marked in red in Fig. 1, is separated by a gap from the bottom mechanical beam in order to increase the voltage sensitivity and thus improve the AC-DC conversion efficiency. Note that a large voltage output is required to overcome the threshold voltage of rectifier diodes. The bottom beams of every stage are divided into two beams placed apart from each other to suppress the undesirable torsional and lateral

modes.

Table 5.1 Parameters of the three-stage folded asymmetric-gapped cantilever structure investigated in this paper.

		Stage I	Stage II	Stage III
Piezoelectric layer	Dimension ($l \times w \times t$) (mm)	8.5×10 $\times 0.127$	8.5×5 $\times 0.127$	8.5×2.5 $\times 0.127$
	Material	Ceramic PZT (Lead zirconium titanate)		
	Density ($\times 10^3 \text{ kg/m}^3$)	7.8		
	Young's modulus (GPa)	66		
Bottom mechanical beam	Dimension ($l \times w \times t$) (mm)	$8.5 \times 8 \times 1$	$8.5 \times 8 \times 1$	$8.5 \times 8 \times 1$
	Material	Aluminum		
	Density ($\times 10^3 \text{ kg/m}^3$)	2.7		
	Young's modulus (GPa)	69		
Proof mass	Weight (g)	29	20	50
	Material	Aluminum		
	Density ($\times 10^3 \text{ kg/m}^3$)	2.7		

	Young's modulus (GPa)	69
--	-----------------------	----

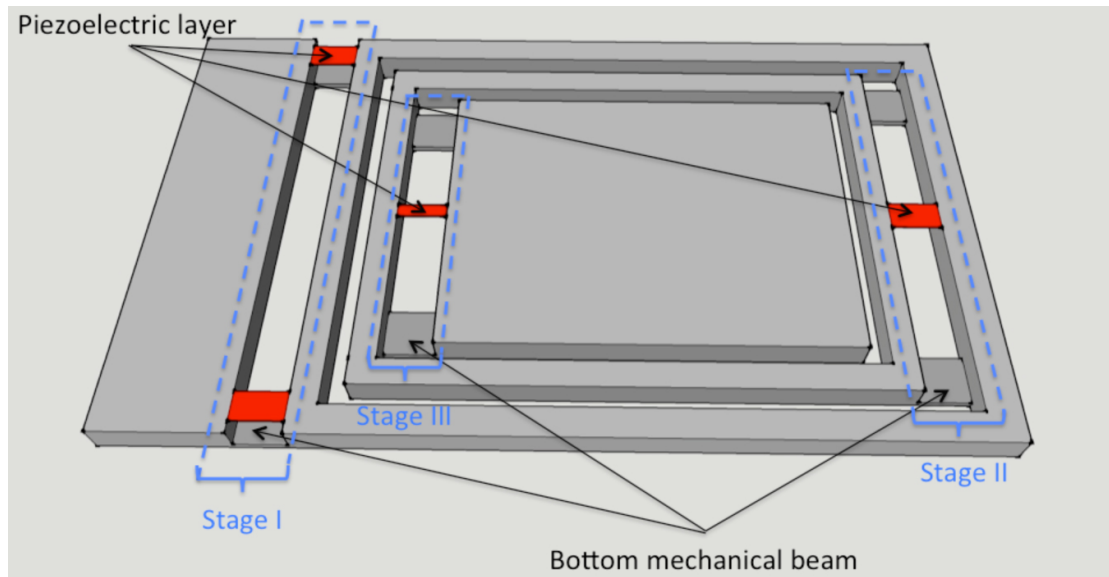
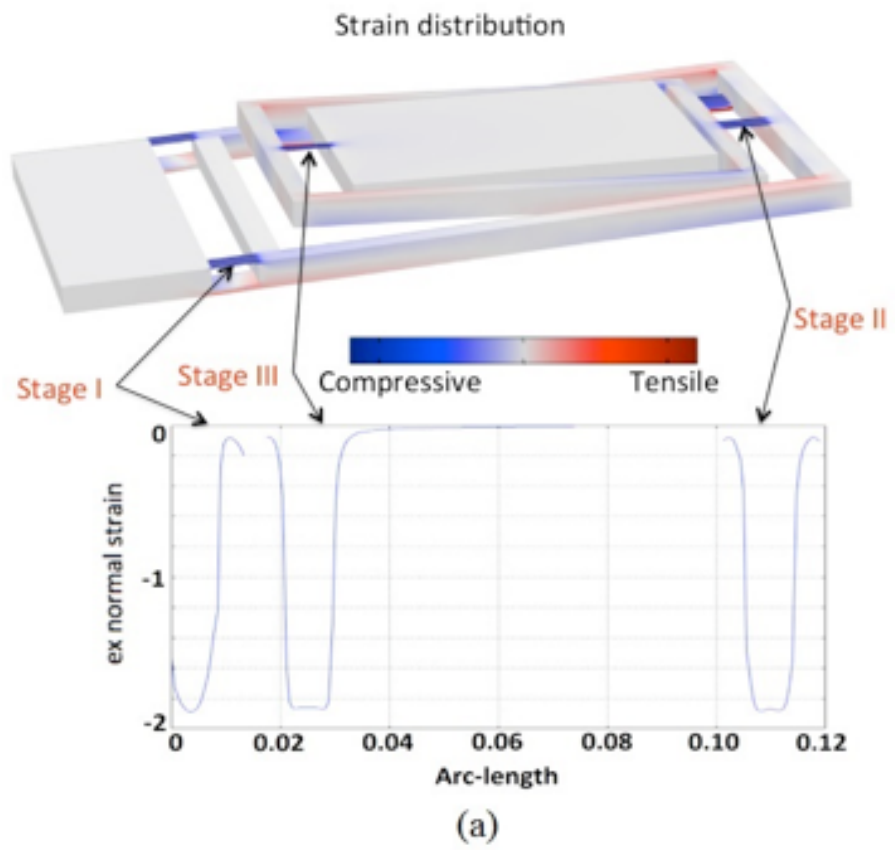


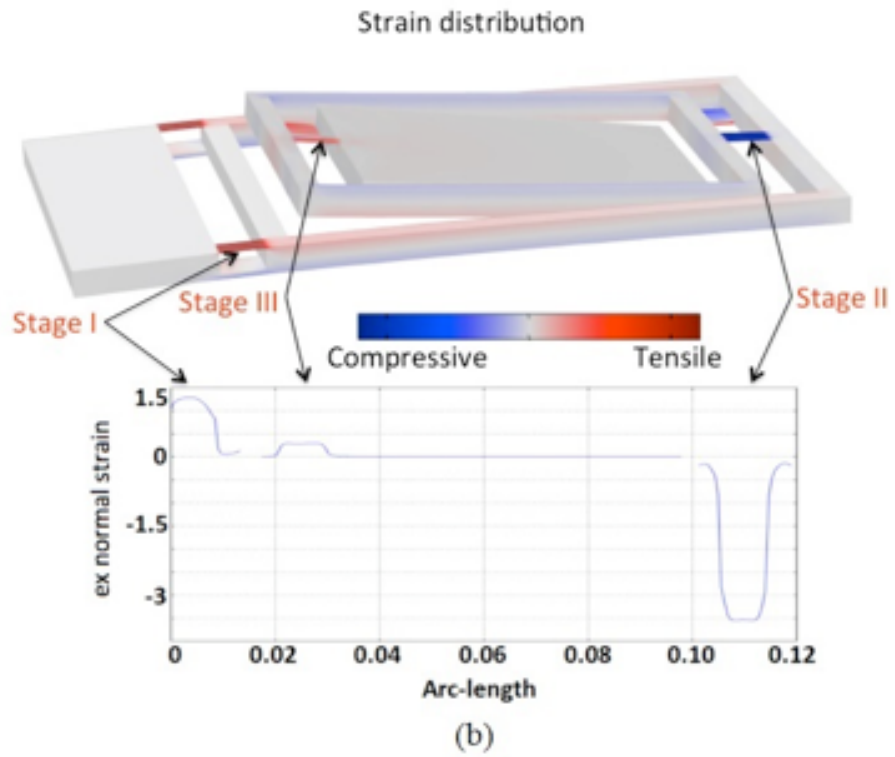
Figure 5.2 Schematic of the wideband VEH based on a three-stage folded asymmetric-gapped cantilever structure

5.2.2 FEA simulation

The finite element simulation was first carried out (COMSOL Multiphysics®) to study the vibration modes, the resonant frequencies and the strain distribution on the piezoelectric layers among three stages. The results of the first three resonant modes are shown in Fig. 5.3. The color in the mode shape illustrates the magnitude and polarity of the mechanical strain (red for tensile strain and blue for compressive strain). The first three short-circuit (open-circuit) resonant frequencies based on the simulation are 36.9 Hz (37.4 Hz), 69.9 Hz (70.7 Hz) and 131.6 Hz (132.2 Hz), respectively. In the first resonant mode shown in Fig. 5.3 (a), the three stages vibrate in the same phase (upward), and all the piezoelectric layer experience compressive strain

(indicated by the blue color). Our design also enables the strain to be almost equally distributed among the three piezoelectric stages. In the second mode shown in Fig. 5.3 (b), stages I and III vibrate in the same phase and are 180° apart from stage II. This phase information can also be observed by the different polarities of the mechanical strains (red vs. blue) experienced by the three stages. Stage II is dominant in this mode and the strain is mainly distributed on stage II. In the third mode shown in Fig. 5.3 (c), stages I and II vibrate in the same phase and are 180° apart from stage III. Stage III is dominant in this mode, and the strain is mainly distributed on stage III. In all three modes, every stage of the folded structure deflects in the form of pure bending which is the desired bending mode for effectively generating output voltage. Since the heaviest proof mass is placed at the last stage of the folded cantilever, it is effectively utilized to stretch/compress the piezoelectric layers. Other higher order modes typically lead to mechanical strains of opposite signs along the thickness or lateral directions of the piezoelectric layer, canceling generated charges or making the electrode design much more complicated.





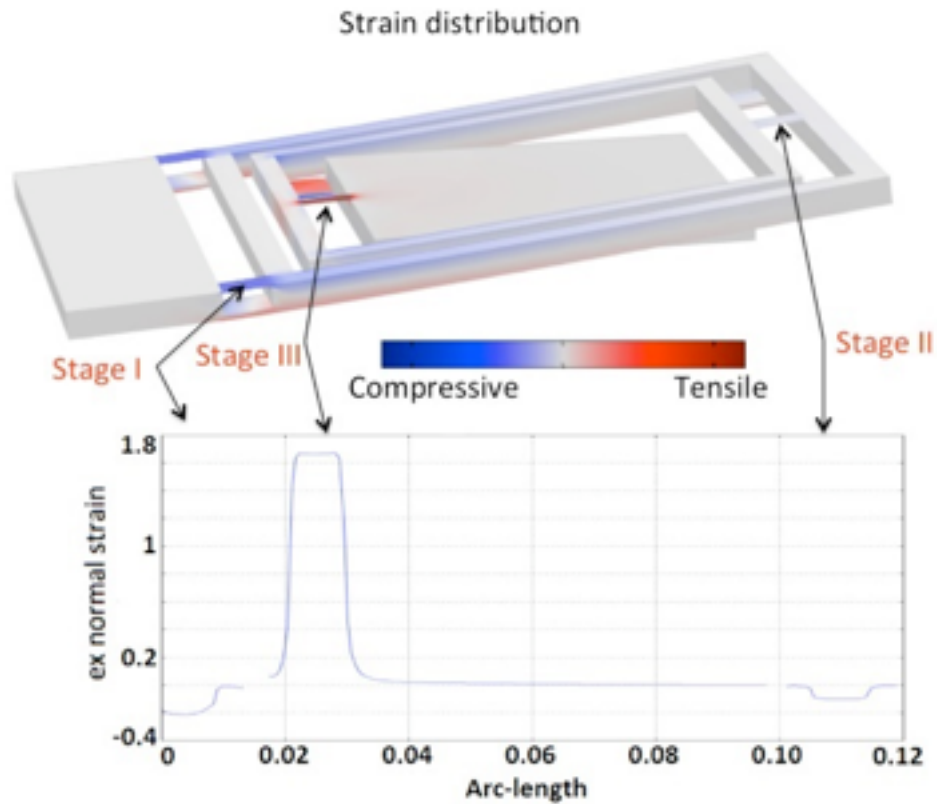


Figure 5.3 The simulation results of the first three resonant modes of the three-stage folded asymmetric gapped structure: (a) the first resonant mode; (b) the second resonant mode; and (c) the third resonant mode.

5.3 Characterization

A prototype device with the design parameters shown in Table 5.1 was constructed and characterized to verify the simulation results. An aluminum block was machined to form proof masses and bottom mechanical beams of the device. Ceramic PZT (Lead zirconium titanate) sheets (Piezo Systems, #PSI-5A4E), which function as energy conversion elements, were bonded above the mechanical beams as schematically shown in Fig. 5.2. The device was mounted on a mechanical shaker (Labworks, Inc ET-126B-1) together with a reference accelerometer

(Endevco, Model 4416B) to calibrate the acceleration. The open-circuit frequency responses of the three stages were recorded using a data acquisition board (National Instrument, USB 6210) as the vibration frequency swept from 15 Hz to 200 Hz. The first three open-circuit resonant frequencies are 35.4 Hz, 74.2 Hz and 126.4 Hz, respectively. The short-circuit resonant frequencies were also measured by loading the outputs of PZT sheets with three 1k Ω resistors. The first three short-circuit resonant frequencies are 34.5 Hz, 73.7 Hz and 124.9 Hz, respectively, slightly lower than the open-circuit values as expected. For both short-circuit and open-circuit cases, the measured resonant frequencies are within 10% error range of the simulation result. The dominant stages of every resonant mode are also consistent with the simulation. As shown in Fig. 5.4, in the first resonant mode, the three stages have almost equal voltage outputs. In the second resonant mode, stage II dominates, and has the largest output voltage, whereas in the third resonant mode, stage III displays the largest output voltage. As noticed, the first three resonant frequencies of the folded structure are fairly close to each other, which is highly desirable for wideband VEH. Moreover, the second and third modes exhibit reasonably high voltage sensitivities, allowing this device to harvest a reasonable amount of energy from the second and third resonant modes.

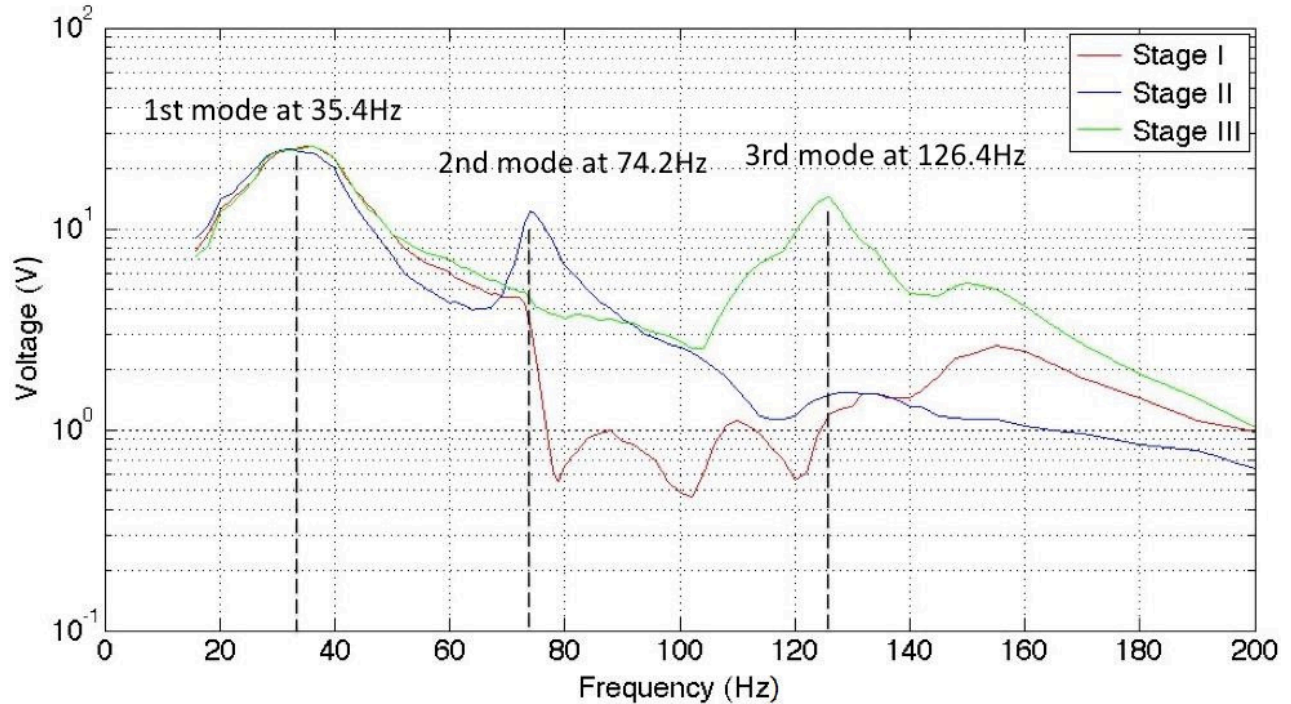


Figure 5.4 Frequency responses of the three stages of the folded cascaded structure.

5.4 Preliminary tests

The energy harvesting ability of the device was evaluated for a real building automation application: air conditioning system monitoring. In the experiment, the prototype was mounted on the air conditioning unit on the ceiling in our engineering lab as shown in Fig. 5.5. The vibration of the air conditioning unit was measured using a commercial accelerometer (Endevco, Model 4416B). The average vibration amplitude was below 0.1g (gravity), and its power spectrum density is plotted in Fig. 5.6. As we can observe from the spectrum, this air conditioning unit generates vibrations in a broad frequency band. There are a few main frequency components at about 30 Hz, 48Hz, 70Hz and 146Hz for this particular air conditioning unit. The red lines illustratively show the resonant peaks of the folded VEH at 34.5 Hz, 73.7 Hz and 124.9 Hz. While the proof-of-concept prototype is not particularly designed for this air

conditioning unit, it definitely demonstrates a great potential in matching up its multi-resonant frequencies to the vibration characteristics of this air conditioning unit to achieve the optimal wideband energy harvesting. Even for this prototype, the output voltage of the three piezoelectric stages still generated an average peak voltage over 3V as shown in the inset of Fig. 5.7. The three alternating current outputs were separately rectified by three bridge rectifiers and then combined to charge a 2200 μF capacitor. A sample charging curve is presented in Fig. 5.7. The average harvested power is estimated to be 1.1 μW . The power can be further increased by designing an optimized device which better matches the vibration characteristics of this air conditioning unit. It is also worth noting that the asymmetric-gapped structure contributes to the relatively high output voltage under the weak ambient vibration, i.e., 0.1g. It is very critical to have a large voltage (e.g., >1.4 V) to avoid significant power loss in diode rectifiers.

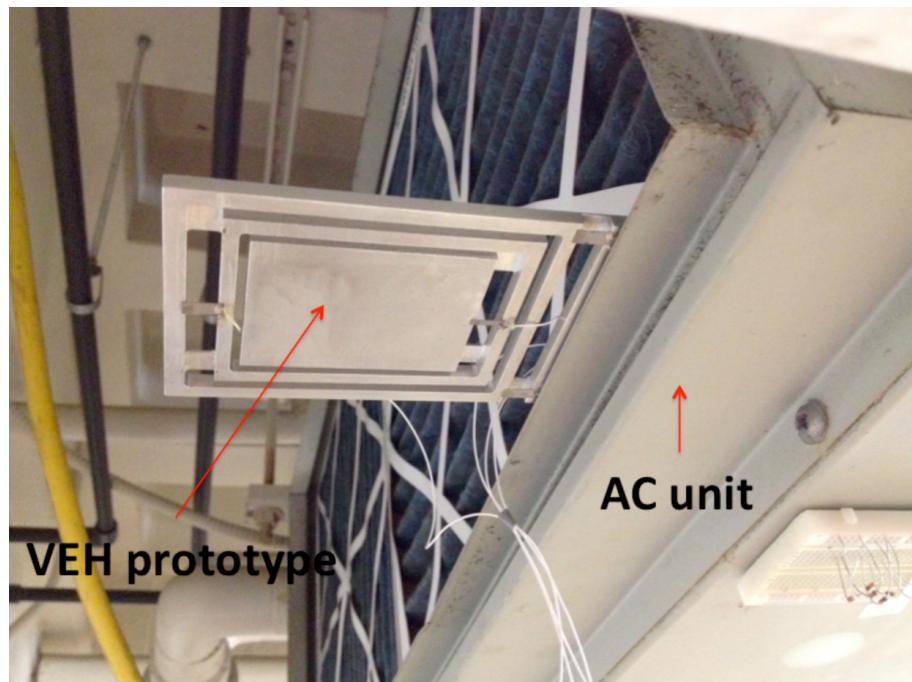


Figure 5.5 The VEH prototype mounted on the ceiling air conditioning unit.

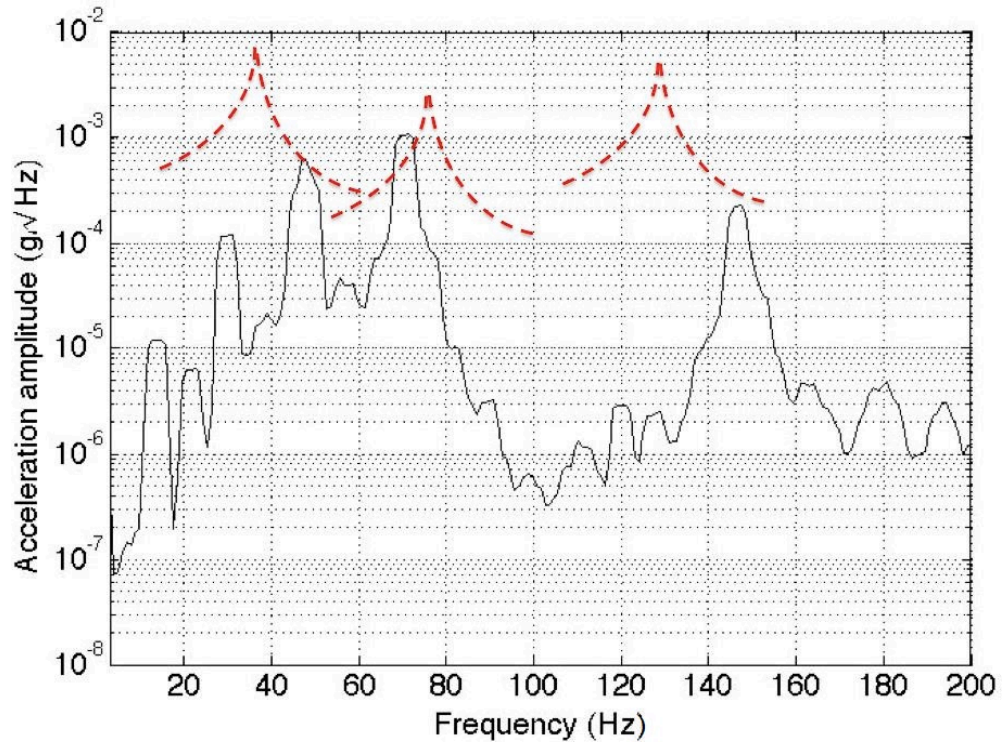


Figure 5.6 The vibration spectrum of the ceiling air conditioning unit

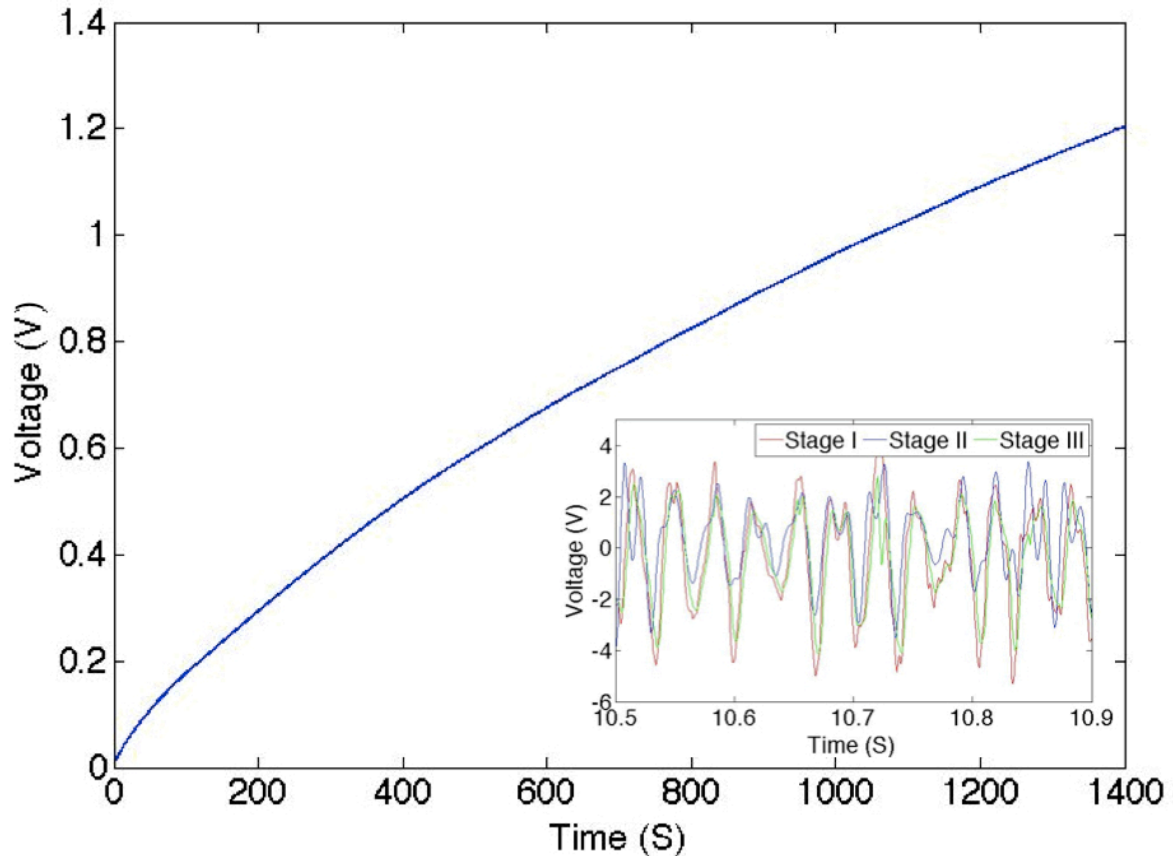


Figure 5.7 The output voltage of a 2200 μF capacitor charged by the prototype VEH under the vibration of a ceiling air conditioning unit. The inset plots representative output voltages of the piezoelectric layers in stages I, II and III before rectification.

5.5 Conclusion

While ambient vibrational energy is widespread, its wideband and time-varying nature as well as its weak amplitude in many applications make it a challenging task to generate enough power from vibration. This chapter reports the development of a wideband VEH based on a folded asymmetric-gapped cantilever structure. Compared with other multi-mass multi-spring

systems, in our design the largest proof mass can be placed at the last stage and simultaneously the first three resonant modes are constituted by pure bending, which is the most effective bending shape to generate electricity. Such a device demonstrated a rectified power of $1.1 \mu\text{W}$ under weak vibration ($\sim 0.1 \text{ g}$) of an air conditioning unit. It is worth noting that the VEH presented in this paper is for proof-of-concept purpose, and is not specifically designed for this air conditioning unit. With a targeted design to better match the resonant frequencies of the vibration source (e.g., air conditioning unit), the harvested power could be significantly increased. We believe the design proposed in this paper could be useful for powering medical implants and wireless sensors for structural health monitoring, machine monitoring, and geophysical monitoring.

CHAPTER 6 FUTURE WORK

6.1 Piezoelectric accelerometer

In the future work, more design aspects of the piezoelectric accelerometer will be studied. First, the selection of piezoelectric materials will be investigated. By comparing different piezoelectric material properties and selecting the feasible materials, the accelerometer performance could be further enhanced. Second, we will further investigate into the charge amplifier optimization. This including the feedback capacitance selection and input guarding issues which is very critical for amplifying a high impedance signal. Third, the improvement on the noise reduction will be investigated. Last but not the least, the mass loading effect for vibration sensing will be studied for better the signal coupling.

6.2 Cardio-respiratory sound monitoring

While the preliminary test shows promising result of cardio-respiratory sound monitoring in a noise-controlled environment. In the future, we will investigate the methods to reduce the artificial noise generated from clothes friction with the sensor surface or wire friction. This could possibly be achieved by adding a low friction coating on the package surface. What's more, by applying a reference sensor on the side, the common mode noise could be reduced by the noise cancellation technique.

Meanwhile, more clinical test will be carried out to further investigate the sensor's performance on heart failure patient. And the study of how to analyze and categorize different types of heart sound signal will also be carried out.

6.3 BCG monitoring and seismic sensing

In the previous study, we carried out some basic analytical analysis for the cascaded structure to prove of the concept that it has the potential to be used in low frequency sensing. Later, a more comprehensive analytical model for the cascaded structure should be further studied for design optimization. The BCG signal was successfully acquired by the prototype in a controlled environment. In the future, more work will be carried out on the characterization of the detailed information in the BCG signal. What's more, even the sensor has a low enough noise floor for BCG monitoring purpose, in order the utilize it in a more challenging environment such as for seismic sensing, the noise performance at low frequency range between 0.1 Hz and 10Hz needs to be further reduced.

6.4 Vibration enegy harvesting

It this thesis, the folded gapped structure has been developed for enabling multiple resonances in a relatively narrow bandwidth to mimic wide band vibration energy harvesting. Even though the FEA simulation matches the experimental result, it is still hard to predict the higher mode vibration such as the dominant stage and resonant frequencies. In order to better align the design with the vibration signature of the targeted source, more systemic study should be carried out in the future. Also, the prototype uses d_{31} mode of the piezoelectric material for energy harvesting. In the future, more work could be done to explore the d_{33} mode to achieve higher energy conversion efficiency since the d_{33} mode has a much higher piezoelectric coefficient. Moreover, besides the harvesting component, energy conversion and storage components as well as low power IC and wireless transmission technology all together plays critical role in building a high efficient and reliable wireless sensing node. Therefore, more work

could be done on the system level integration in the future.

6.5 *Other applications*

What's more, there are many other potential applications on physiological acoustic sensing worth investigation. For example, accelerometer-based physiological sound monitors can record heart sounds, seismocardiogram, ballistocardiogram, respiratory sound and gastrointestinal sounds. There are a number of challenges need to be addressed by collaborative effort of researchers from multiple disciplines. With the advances in sensors, signal processing algorithms, and a better understanding of the genesis of physiological sounds, the accelerometer-based acoustic monitoring system is expected to make more significant clinical impact, especially on the emerging mobile healthcare.

Other applications including the sensing beam design for the atomic force microscope, force sensing and time reference, etc., is also of great interests.

REFERENCE

1. Zou, Y., L. Tong, and G.P. Steven, *Vibration-based model-dependent damage (delamination) identification and health monitoring for composite structures - A review*. Journal of Sound and Vibration, 2000. **230**(2): p. 357-378.
2. Mcfadden, P.D. and J.D. Smith, *Vibration Monitoring of Rolling Element Bearings by the High-Frequency Resonance Technique - a Review*. Tribology International, 1984. **17**(1): p. 3-10.
3. Rowlands, A.V., *Accelerometer assessment of physical activity in children: An update*. Pediatric Exercise Science, 2007. **19**(3): p. 252-266.
4. Murphy, S.L., *Review of physical activity measurement using accelerometers in older adults: Considerations for research design and conduct*. Preventive Medicine, 2009. **48**(2): p. 108-114.
5. Ward, D.S., et al., *Accelerometer use in physical activity: Best practices and research recommendations (vol 37, pg S588, 2005)*. Medicine and Science in Sports and Exercise, 2006. **38**(3): p. 610-610.
6. Macdonald, G.A., *A Review of Low-Cost Accelerometers for Vehicle Dynamics*. Sensors and Actuators a-Physical, 1990. **21**(1-3): p. 303-307.
7. van Kampen, R.P. and R.F. Wolffenbuttel, *Modeling the mechanical behavior of bulk-micromachined silicon accelerometers*. Sensors and Actuators a-Physical, 1998. **64**(2): p. 137-150.

8. Tabibazar, M. and A. Garciavalenzuela, *Sensing Means and Sensor Shells - a New Method of Comparative-Study of Piezoelectric, Piezoresistive, Electrostatic, Magnetic, and Optical Sensors*. Sensors and Actuators a-Physical, 1995. **48**(2): p. 87-100.
9. Shieh, J., et al., *The selection of sensors*. Progress in Materials Science, 2001. **46**(3-4): p. 461-504.
10. Seidel, H. and L. Csepregi, *Design Optimization for Cantilever-Type Accelerometers*. Sensors and Actuators, 1984. **6**(2): p. 81-92.
11. Zheng, Q.L., Z. Wang, and Y. Xu, *Symmetric air-spaced cantilevers for strain sensing*. Sensors and Actuators a-Physical, 2008. **147**(1): p. 142-149.
12. Levinzon, F.A., *Ultra-Low-Noise Seismic Piezoelectric Accelerometer With Integral FET Amplifier*. Ieee Sensors Journal, 2012. **12**(6): p. 2262-2268.
13. Zou, Q., et al., *Single- and triaxis piezoelectric-bimorph accelerometers*. Journal of Microelectromechanical Systems, 2008. **17**(1): p. 45-57.
14. Hindrichsen, C.C., et al., *Circular Piezoelectric Accelerometer for High Band Width Application*. 2009 Ieee Sensors, Vols 1-3, 2009: p. 475-478.
15. Gabrielson, T.B., *Mechanical-Thermal Noise in Micromachined Acoustic and Vibration Sensors*. Ieee Transactions on Electron Devices, 1993. **40**(5): p. 903-909.
16. Sanchez, I. and H. Pasterkamp, *Tracheal sound spectra depend on body height*. American Review of Respiratory Disease, 1993. **148**(4): p. 1083-1087.
17. Vermarien, H. and E. Vanvollenhoven, *The recording of heart vibrations - a problem of vibration measurement on soft-tissue*. Medical & Biological Engineering & Computing, 1984. **22**(2): p. 168-178.

18. Vermarien, H. and E. Vanvollenhoven, *Quantification of the influence of mass and contact diameter of phonocardiographic transducers on high-frequency heart-sound recordings*. Acta Cardiologica, 1986. **41**(3): p. 237-243.
19. Zanartu, M., et al., *Air-Borne and Tissue-Borne Sensitivities of Bioacoustic Sensors Used on the Skin Surface*. Biomedical Engineering, IEEE Transactions on, 2009. **56**(2): p. 443-451.
20. Castiglioni, P., et al. *Wearable Seismocardiography*. in *Engineering in Medicine and Biology Society, 2007. EMBS 2007. 29th Annual International Conference of the IEEE*. 2007.
21. Di Rienzo, M., et al. *A wearable system for the seismocardiogram assessment in daily life conditions*. in *Engineering in Medicine and Biology Society, EMBC, 2011 Annual International Conference of the IEEE*. 2011.
22. Castiglioni, P., et al. *Cardiac sounds from a wearable device for sternal seismocardiography*. in *33rd Annual International Conference of the IEEE Engineering in Medicine and Biology Society, EMBS 2011, August 30, 2011 - September 3, 2011*. 2011. Boston, MA, United states: Institute of Electrical and Electronics Engineers Inc.
23. Di Rienzo, M., et al. *24h seismocardiogram monitoring in ambulant subjects*. in *Engineering in Medicine and Biology Society (EMBC), 2012 Annual International Conference of the IEEE*. 2012.
24. Bryant, D., et al. *Real-time implementation of a chest-worn accelerometer based heart monitoring system*. in *Circuits and Systems (MWSCAS), 2010 53rd IEEE International Midwest Symposium on*. 2010.

25. Pandia, K., et al. *Motion artifact cancellation to obtain heart sounds from a single chest-worn accelerometer*. in *2010 IEEE International Conference on Acoustics, Speech, and Signal Processing, ICASSP 2010, March 14, 2010 - March 19, 2010*. 2010. Dallas, TX, United states: Institute of Electrical and Electronics Engineers Inc.
26. Bombardini, T., et al., *Abnormal shortened diastolic time length at increasing heart rates in patients with abnormal exercise-induced increase in pulmonary artery pressure*. *Cardiovascular Ultrasound*, 2011. **9**.
27. Urbaszek, A., et al., *Hemodynamic Monitoring with an Implantable Pressure Monitor is Improved by Additional Detection of Heart Sounds*. *Biomedical Engineering-Biomedizinische Technik*, 2012. **57**.
28. Maki, H., et al. *A daily living activity remote monitoring system for solitary elderly people*. in *Engineering in Medicine and Biology Society, EMBC, 2011 Annual International Conference of the IEEE*. 2011.
29. He, D.D., E.S. Winokur, and C.G. Sodini, *A continuous, wearable, and wireless heart monitor using head ballistocardiogram (BCG) and head electrocardiogram (ECG)*, in *Engineering in Medicine and Biology Society, EMBC, 2011 Annual International Conference of the IEEE*. 2011. p. 4729-4732.
30. Imtiaz, M.S., et al. *Correlation between seismocardiogram and systolic blood pressure*. in *Electrical and Computer Engineering (CCECE), 2013 26th Annual IEEE Canadian Conference on*. 2013.
31. Erne, P., *Beyond auscultation - acoustic cardiography in the diagnosis and assessment of cardiac disease*. *Swiss Medical Weekly*, 2008. **138**(31-32): p. 439-452.

32. Przystup, P., et al. *A multisensor detector of a sleep apnea for using at home*. in *2013 6th International Conference on Human System Interactions, HSI 2013, June 6, 2013 - June 8, 2013*. 2013. Gdansk, Sopot, Poland: IEEE Computer Society.
33. Torres, A., et al. *Application of the empirical mode decomposition method to the analysis of respiratory mechanomyographic signals*. in *29th Annual International Conference of IEEE-EMBS, Engineering in Medicine and Biology Society, EMBC'07, August 23, 2007 - August 26, 2007*. 2007. Lyon, France: Inst. of Elec. and Elec. Eng. Computer Society.
34. Johansson, A., et al., *Pulse wave transit time for monitoring respiration rate*. *Medical and Biological Engineering and Computing*, 2006. **44**(6): p. 471-478.
35. Kraman, S.S., et al., *Effects of breathing pathways on tracheal sound spectral features*. *Respiration Physiology*, 1998. **111**(3): p. 295-300.
36. Gnitecki, J. and Z. Moussavi, *The fractality of lung sounds: A comparison of three waveform fractal dimension algorithms*. *Chaos, Solitons & Fractals*, 2005. **26**(4): p. 1065-1072.
37. Ahlstrom, C., et al., *Heart sound cancellation from lung sound recordings using recurrence time statistics and nonlinear prediction*. *Signal Processing Letters, IEEE*, 2005. **12**(12): p. 812-815.
38. Ahlstrom, C., et al., *A method for accurate localization of the first heart sound and possible applications*. *Physiological Measurement*, 2008. **29**(3): p. 417.
39. Flores-Tapia, D., Z.M.K. Moussavi, and G. Thomas, *Heart Sound Cancellation Based on Multiscale Products and Linear Prediction*. *Biomedical Engineering, IEEE Transactions on*, 2007. **54**(2): p. 234-243.

40. Gnitecki, J., Z. Moussavi, and H. Pasterkamp, *Diagnostic potential in state space parameters of lung sounds*. Medical & Biological Engineering & Computing, 2008. **46**(1): p. 93-99.
41. Elphick, H.E., et al., *Validity and reliability of acoustic analysis of respiratory sounds in infants*. Archives of Disease in Childhood, 2004. **89**(11): p. 1059-1063.
42. Shirazi, S.S. and Z.M.K. Moussavi, *Acoustical Modeling of Swallowing Mechanism*. Biomedical Engineering, IEEE Transactions on, 2011. **58**(1): p. 81-87.
43. Hasselstrom, L.J., et al., *Effects of intravenous bupivacaine on cardiovascular function and plasma catecholamine levels in humans*. Anesth Analg, 1984. **63**(12): p. 1053-8.
44. Carroll, D., M.G. Harris, and G. Cross, *Haemodynamic Adjustments to Mental Stress in Normotensives and Subjects with Mildly Elevated Blood Pressure*. Psychophysiology, 1991. **28**(4): p. 438-446.
45. Foldager, N. and F. Bonde-Petersen, *Human cardiovascular reactions to simulated hypovolaemia, modified by the opiate antagonist naloxone*. European Journal of Applied Physiology and Occupational Physiology, 1988. **57**(4): p. 507-513.
46. Ahlstrom, C., et al., *Noninvasive investigation of blood pressure changes using the pulse wave transit time: a novel approach in the monitoring of hemodialysis patients*. Journal of Artificial Organs, 2005. **8**(3): p. 192-197.
47. Brubakk, O., T.R. Pedersen, and K. Overskeid, *Noninvasive evaluation of the effect of timolol on left ventricular performance after myocardial infarction and the consequence for prognosis*. Journal of the American College of Cardiology, 1987. **9**(1): p. 155-160.
48. Elphick, H.E., et al., *When a "wheeze" is not a wheeze: acoustic analysis of breath sounds in infants*. European Respiratory Journal, 2000. **16**(4): p. 593-597.

49. Pressler, G.A., et al., *Detection of respiratory sounds at the external ear*. Ieee Transactions on Biomedical Engineering, 2004. **51**(12): p. 2089-2096.
50. Lee, J., et al., *A radial basis classifier for the automatic detection of aspiration in children with dysphagia*. Journal of Neuroengineering and Rehabilitation, 2006. **3**.
51. Bentur, L., et al., *Wheeze monitoring in children for assessment of nocturnal asthma and response to therapy*. European Respiratory Journal, 2003. **21**(4): p. 621-626.
52. Räsänen, J. and N. Gavriely, *Detection of porcine oleic acid-induced acute lung injury using pulmonary acoustics*. Journal of Applied Physiology, 2002. **93**(1): p. 51-57.
53. Fiz, J.A., et al., *Detection of wheezing during maximal forced exhalation in patients with obstructed airways*. CHEST Journal, 2002. **122**(1): p. 186-191.
54. Bentur, L., et al., *Adenosine bronchial provocation with computerized wheeze detection in young infants with prolonged cough*: Correlation with long-term follow-up*. CHEST Journal, 2004. **126**(4): p. 1060-1065.
55. Prodhan, P., et al., *Wheeze Detection in the Pediatric Intensive Care Unit: Comparison Among Physician, Nurses, Respiratory Therapists, and a Computerized Respiratory Sound Monitor*. Respiratory Care, 2008. **53**(10): p. 1304-1309.
56. Pasterkamp, H. and I. Sanchez, *Effect of gas density on respiratory sounds*. American Journal of Respiratory and Critical Care Medicine, 1996. **153**(3): p. 1087-1092.
57. Malmberg, L.P., L. Pesu, and A.R. Sovijärvi, *Significant differences in flow standardised breath sound spectra in patients with chronic obstructive pulmonary disease, stable asthma, and healthy lungs*. Thorax, 1995. **50**(12): p. 1285-1291.
58. Boner, A.L., et al., *Children with Nocturnal Asthma Wheeze Intermittently During Sleep*. Journal of Asthma, 2010. **47**(3): p. 290-294.

59. Räsänen, J., M.E. Nemergut, and N. Gavriely, *Effect of positive end-expiratory pressure on acoustic wave propagation in experimental porcine lung injury*. *Clinical Physiology and Functional Imaging*, 2014: p. n/a-n/a.
60. Hansen, P.B., et al., *Phonocardiography as a Monitor of Cardiac Performance During Anesthesia*. *Anesthesia & Analgesia*, 1989. **68**(3): p. 385-387.
61. DRUZGALSKI, C.K., R.L. DONNERBERG, and R.M. CAMPBELL, *Techniques of Recording Respiratory Sounds*. *Journal of Clinical Engineering*, 1980. **5**(4): p. 321-330.
62. Voon, W.-C., S.-H. Sheu, and Y.-Y. Hwang, *Doppler Study of Transmitted Transmitral A Wave in Patients with a Fourth Heart Sound*. *Echocardiography*, 1997. **14**(3): p. 243-249.
63. Orizio, C., R. Perini, and A. Veicsteinas, *Muscular sound and force relationship during isometric contraction in man*. *European Journal of Applied Physiology and Occupational Physiology*, 1989. **58**(5): p. 528-533.
64. Esposito, F., et al., *Time and frequency domain analysis of electromyogram and sound myogram in the elderly*. *European Journal of Applied Physiology and Occupational Physiology*, 1996. **73**(6): p. 503-510.
65. Miller, A., et al., *Spectral-analysis of arterial bruits (phonoangiography) - experimental validation*. *Circulation*, 1980. **61**(3): p. 515-520.
66. Pasterkamp, H., et al., *Measurement of respiratory acoustical signals - comparison of sensors*. *Chest*, 1993. **104**(5): p. 1518-1525.
67. Kraman, S.S., et al., *Comparison of lung sound transducers using a bioacoustic transducer testing system*. *J Appl Physiol*, 2006. **101**(2): p. 469-476.

68. Suzuki, A. and K. Nakayama. *The absolute sensitivity characteristics of lung-sound transducers coupled to chest wall*. in *Engineering in Medicine and Biology Society, 1998. Proceedings of the 20th Annual International Conference of the IEEE*. 1998.
69. Tavakolian, K., et al., *Precordial acceleration signals improve the performance of diastolic timed vibrations*. *Medical Engineering & Physics*, 2013. **35**(8): p. 1133-1140.
70. Salerno, D.M., et al., *Seismocardiographic changes associated with obstruction of coronary blood flow during balloon angioplasty*. *The American Journal of Cardiology*, 1991. **68**(2): p. 201-207.
71. Salerno, D.M. and J. Zanetti, *Seismocardiography - a new technique for recording cardiac vibrations - concept, method, and initial observations*. *Journal of Cardiovascular Technology*, 1990. **9**(2): p. 111-118.
72. Salerno, D.M. and J. Zanetti, *Seismocardiography for monitoring changes in left-ventricular function during ischemia*. *Chest*, 1991. **100**(4): p. 991-993.
73. Tavakolian, K., et al. *Comparative analysis of infrasonic cardiac signals*. in *36th Annual Conference of Computers in Cardiology, CinC 2009, September 13, 2009 - September 16, 2009*. 2009. Park City, UT, United states: IEEE Computer Society.
74. Rendon, D.B., et al. *Mapping the Human Body for Vibrations using an Accelerometer*. in *Engineering in Medicine and Biology Society, 2007. EMBS 2007. 29th Annual International Conference of the IEEE*. 2007.
75. Morillo, D.S., et al., *An Accelerometer-Based Device for Sleep Apnea Screening*. *Ieee Transactions on Information Technology in Biomedicine*, 2010. **14**(2): p. 491-499.

76. Prisk, G.K., et al., *Three-dimensional ballistocardiography and respiratory motion in sustained microgravity*. Aviation Space and Environmental Medicine, 2001. **72**(12): p. 1067-1074.
77. Bew, F.E., et al., *Pixie cardiography - accelerometer applications to phonocardiography and displacement cardiography in childhood*. British Heart Journal, 1971. **33**(5): p. 702-&.
78. Wodicka, G.R., et al., *Spectral characteristics of sound-transmission in the human respiratory system*. IEEE Transactions on Biomedical Engineering, 1990. **37**(12): p. 1130-1135.
79. Padmanabhan, V., J.L. Semmlow, and W. Welkowitz, *Accelerometer type cardiac transducer for detection of low-level heart sounds*. IEEE Transactions on Biomedical Engineering, 1993. **40**(1): p. 21-28.
80. Hu, Y. and Y. Xu, *An ultra-sensitive wearable accelerometer for continuous heart and lung sound monitoring*, in *Engineering in Medicine and Biology Society (EMBC), 2012 Annual International Conference of the IEEE*. 2012. p. 694-697.
81. Naeli, K. and O. Brand, *Cantilever sensor with stress-concentrating piezoresistor design*. 2005 Ieee Sensors, Vols 1 and 2, 2005: p. 592-595.
82. Kirchner, J., et al. *Enhancement of pulse contour analysis in the pulmonary artery by use of heart sounds*. in *Sensors, 2011 IEEE*. 2011.
83. Kawamura, Y., Y. Yokota, and F. Nogata. *Propagation Route Estimation of Heart Sound through Simultaneous Multi-site Recording on the Chest Wall*. in *Engineering in Medicine and Biology Society, 2007. EMBS 2007. 29th Annual International Conference of the IEEE*. 2007.

84. John, J., et al., *Microfabrication of 3D neural probes with combined electrical and chemical interfaces*. Journal of Micromechanics and Microengineering, 2011. **21**(10).
85. Zheng, Q.L. and Y. Xu, *Asymmetric air-spaced cantilevers for vibration energy harvesting*. Smart Materials & Structures, 2008. **17**(5).
86. Li, Y.F., et al., *Micromachined Piezoresistive Accelerometers Based on an Asymmetrically Gapped Cantilever*. Journal of Microelectromechanical Systems, 2011. **20**(1): p. 83-94.
87. Zheng, Q. and Y. Xu, *Vibration energy harvesting device based on asymmetric air-spaced cantilevers for tire pressure monitoring system*, in *The 9th International Workshop on Micro and Nanotechnology for Power Generation and Energy Conversion Applications*. 2009: Washington DC, USA.
88. Hu, Y.T., Q.L. Zheng, and Y. Xu, *High Performance Atomic Force Microscope Based on Air-spaced Piezoresistive Cantilevers*. 2010 IEEE SENSORS, 2010: p. 1390-1394.
89. Bao, M.H., *Micro Mechanical Transducers: Pressure Sensors, Accelerometers and Gyroscopes*. 2000: Elsevier Science.
90. Levinzon, F.A., *Fundamental noise limit of piezoelectric accelerometer*. Ieee Sensors Journal, 2004. **4**(1): p. 108-111.
91. Loudon, R. and R.L. Murphy, Jr., *Lung sounds*. The American review of respiratory disease, 1984. **130**(4): p. 663-73.
92. Gavriely, N. and D.W. Cugell, *Breath sounds sensors*, in *Breath sounds methodology*. 1995, CRC Press: Boca Raton, Florida. p. 31-47.

93. Pasterkamp, H., S.S. Kraman, and G.R. Wodicka, *Respiratory sounds - Advances beyond the stethoscope*. American Journal of Respiratory and Critical Care Medicine, 1997. **156**(3): p. 974-987.
94. Felner, J.M., *The First Heart Sound*, in *Clinical Methods: The History, Physical, and Laboratory Examinations*, H.W. Walker HK, Hurst JW, Editor. 1990, Butterworths: Boston.
95. Carlson, G.M., L. Green, and K.Z. Siejko, *Third heart sound activity index for heart failure monitoring*. 2006, Cardiac Pacemakers, Inc.
96. Ishmail, A.A., et al., *Interobserver agreement by auscultation in the presence of a third heart sound in patients with congestive heart failure*. Chest, 1987. **91**(6): p. 870-873.
97. Drazner, M.H., et al., *Prognostic importance of elevated jugular venous pressure and a third heart sound in patients with heart failure*. New England Journal of Medicine, 2001. **345**(8): p. 574-581.
98. Reed, T.R., N.E. Reed, and P. Fritzon, *Heart sound analysis for symptom detection and computer-aided diagnosis*. Simulation Modelling Practice and Theory, 2004. **12**(2): p. 129-146.
99. Semmlow, J. and K. Rahalkar, *Acoustic detection of coronary artery disease*. Annual Review of Biomedical Engineering, 2007. **9**: p. 449-469.
100. Akay, M., et al., *Application of the Arma Method to Acoustic Detection of Coronary-Artery Disease*. Medical & Biological Engineering & Computing, 1991. **29**(4): p. 365-372.
101. Aggio, S., et al., *Noninvasive estimation of the pulmonary systolic pressure from the spectral analysis of the second heart sound*. Acta Cardiol, 1990. **45**(3): p. 199-202.

102. Chen, D., et al., *Estimation of pulmonary artery pressure by spectral analysis of the second heart sound*. Am J Cardiol, 1996. **78**(7): p. 785-9.
103. Chen, J., et al., *Early detection of pulmonary hypertension with heart sounds analysis pilot study*. Stud Health Technol Inform, 2006. **122**: p. 112-6.
104. Zhang, X.Y., E. MacPherson, and Y.T. Hang, *Relations between the timing of the second heart sound and aortic blood pressure*. Ieee Transactions on Biomedical Engineering, 2008. **55**(4): p. 1291-1297.
105. Dennis, A., et al., *Noninvasive diagnosis of pulmonary hypertension using heart sound analysis*. Computers in Biology and Medicine, 2010. **40**(Compendex): p. 758-764.
106. Bartels, A. and D. Harder, *Non-invasive determination of systolic blood pressure by heart sound pattern analysis*. Clin Phys Physiol Meas, 1992. **13**(3): p. 249-56.
107. Theodor, M., et al. *Implantable accelerometer for determination of blood pressure*. in the *17th International Conference on Solid-State Sensors, Actuators and Microsystems (TRANSDUCERS & EUROSENSORS XXVII)*. 2013. Barcelona, Spain.
108. Kovacs, F., et al., *Computer method for perinatal screening of cardiac murmur using fetal phonocardiography*. Computers in Biology and Medicine, 2009. **39**(12): p. 1130-1136.
109. Kovács, F., et al., *Fetal phonocardiography—Past and future possibilities*. Computer Methods and Programs in Biomedicine, 2011. **104**(1): p. 19-25.
110. Varady, P., et al., *An advanced method in fetal phonocardiography*. Computer Methods and Programs in Biomedicine, 2003. **71**(3): p. 283-296.

111. Olesen, A.G. and J.A. Svare, *Decreased fetal movements: background, assessment, and clinical management*. Acta Obstetricia Et Gynecologica Scandinavica, 2004. **83**(9): p. 818-826.
112. Bekedam, D.J., et al., *Motor Behavior in the Growth Retarded Fetus*. Early Human Development, 1985. **12**(2): p. 155-165.
113. Mesbah, M., et al., *Accelerometer-based Fetal Movement Detection*. 2011 Annual International Conference of the Ieee Engineering in Medicine and Biology Society (Embc), 2011: p. 7877-7880.
114. Khlif, M.S., et al., *Time-Frequency Characterization of Tri-Axial Accelerometer Data for Fetal Movement Detection*. 2011 Ieee International Symposium on Signal Processing and Information Technology (Isspit), 2011: p. 466-471.
115. Liu, Y., C.M. Zhang, and Y.H. Peng, *Neural classification of lung sounds using wavelet packet coefficients energy*. Pricai 2006: Trends in Artificial Intelligence, Proceedings, 2006. **4099**: p. 278-287.
116. Baughman, R.P. and R.G. Loudon, *Lung sound analysis for continuous evaluation of airflow obstruction in asthma*. Chest. , 1985. **88**(3): p. 364-368.
117. Schreur, H.J., et al., *Lung sound intensity in patients with emphysema and in normal subjects at standardised airflows*. Thorax 1992. **47**: p.:674-679.
118. Malmberg, L.P., et al., *Changes in frequency spectra of breath sounds during histamine challenge test in adult asthmatics and healthy control subjects*. Chest, 1994. **105**(1): p. 122-131.

119. PASTERKAMP, H., S.S. KRAMAN, and G.R. WODICKA, *Respiratory Sounds-Advances Beyond the Stethoscope*. American Journal of Respiratory and Critical Care Medicine, 1997. **156**(3): p. 974-987.
120. Bucklin, C.L., M. Das, and S.L. Luo. *An inexpensive accelerometer-based sleep-apnea screening technique*. in *Aerospace and Electronics Conference (NAECON), Proceedings of the IEEE 2010 National*. 2010.
121. Wang, H. and L.Y. Wang. *Continuous Intro-Operative Respiratory Auscultation in Anesthesia*. in *IEEE Sensors 2003*. Toronto.
122. Haladjian, R., et al. *Computer-Aided Continuous Lung Sound Auscultation in Ventilated Patients*. in *A.S.A. Annual Conference*. 2004. Las Vegas.
123. Wang, H., et al. *Separation of Lung and Heart Sound for Anesthesia Diagnosis*. in *the 2006 WSEAS International Conference on Mathematical Biology and Ecology (MABE '06)*. 2006. Miami, Florida, USA.
124. Mann, J., et al. *Simultaneous Activity and Respiratory Monitoring Using an Accelerometer*. in *2011 International Conference on Body Sensor Networks (BSN)*. 2011.
125. Vannuccini, L., et al., *Capturing and preprocessing of respiratory sounds*. European Respiratory Review, 2000. **10**(77): p. 616-620.
126. Baughman, R.P. and R.G. Loudon, *Lung sound analysis for continuous evaluation of airflow obstruction in asthma*. Chest, 1985. **88**(3): p. 364-8.
127. Meslier, N., G. Charbonneau, and J.L. Racineux, *Wheezes*. The European respiratory journal, 1995. **8**(11): p. 1942-8.

128. Rietveld, S., et al., *Characteristics and diagnostic significance of spontaneous wheezing in children with asthma: results of continuous in vivo sound recording*. Journal of Asthma, 1999. **36**(4): p. 351-8.
129. Lenclud, C., et al., *Evaluation of nocturnal bronchoconstriction by all night tracheal sound monitoring*. Thorax, 1996. **51**(7): p. 694-8.
130. Bentur, L., et al., *Wheeze monitoring in children for assessment of nocturnal asthma and response to therapy*. The European respiratory journal, 2003. **21**(4): p. 621-6.
131. Krumpe, P.E. and J.M. Cummiskey, *Use of laryngeal sound recordings to monitor apnea*. The American review of respiratory disease, 1980. **122**(5): p. 797-801.
132. Werthammer, J., et al., *Apnea monitoring by acoustic detection of airflow*. Pediatrics, 1983. **71**(1): p. 53-5.
133. Earis, J.E. and B.M.G. Cheetham, *Future perspectives. for respiratory sound research*. European. Respiratory Review, 2000. **10**(77): p. 641-646.
134. Swallow, L.M., et al., *A piezoelectric fibre composite based energy harvesting device for potential wearable applications*. Smart Materials & Structures, 2008. **17**(2).
135. Mitcheson, P.D., *Energy Harvesting for Human Wearable and Implantable Bio-Sensors*. 2010 Annual International Conference of the Ieee Engineering in Medicine and Biology Society (Embc), 2010: p. 3432-3436.
136. Yoo, J., et al., *A 5.2 mW Self-Configured Wearable Body Sensor Network Controller and a 12 μ W Wirelessly Powered Sensor for a Continuous Health Monitoring System*. Ieee Journal of Solid-State Circuits, 2010. **45**(1): p. 178-188.
137. Madsen, D., et al., *Listening to bowel sounds: An evidence-based practice project*. American Journal of Nursing, 2005. **105**(12): p. 40-49.

138. Baid, H., *A critical review of auscultating bowel sounds*. British journal of nursing (Mark Allen Publishing), 2009. **18**(18): p. 1125-9.
139. Loh, N.C., M.A. Schmidt, and S.R. Manalis, *Sub-10 cm(3) interferometric accelerometer with nano-g resolution*. Journal of Microelectromechanical Systems, 2002. **11**(3): p. 182-187.
140. Levinzon, F.A. *Ultra-low-noise 10 V/g compact IEPE seismic accelerometer*. in *Proceedings of the 26th International Modal Analysis Conference*. 2008.
141. Homeijer, B., et al., *Hewlett Packard's Seismic Grade Mems Accelerometer*. 2011 Ieee 24th International Conference on Micro Electro Mechanical Systems (Mems), 2011: p. 585-588.
142. Katsikogiannis, P., E. Zervas, and G. Kaltsas, *A wireless sensor network for building structural health monitoring and seismic detection*. Physica Status Solidi C - Current Topics in Solid State Physics, Vol 5, No 12 2008, 2008. **5**(12): p. 3834-3838.
143. Huang, H., et al., *Molecular Electronic Transducer-Based Low-Frequency Accelerometer Fabricated With Post-CMOS Compatible Process Using Droplet as Sensing Body*. Ieee Electron Device Letters, 2013. **34**(10): p. 1304-1306.
144. Collette, C., et al., *Review: Inertial Sensors for Low-Frequency Seismic Vibration Measurement*. Bulletin of the Seismological Society of America, 2012. **102**(4): p. 1289-1300.
145. Milligan, D.J., B.D. Homeijer, and R.G. Walmsley, *An Ultra-Low Noise MEMS Accelerometer for Seismic Imaging*. 2011 Ieee Sensors, 2011: p. 1281-1284.
146. Bernstein, J., et al., *Low-noise MEMS vibration sensor for geophysical applications*. Journal of Microelectromechanical Systems, 1999. **8**(4): p. 433-438.

147. Pakhomov, A., et al., *Current seismic sensor issues for defense and security applications*. Sensors, and Command, Control, Communications, and Intelligence(C31) Technologies for Homeland Security and Homeland Defense Iii, Pts 1 and 2, 2004. **5403**: p. 576-581.
148. Speller, K.E. and D.L. Yu, *A low-noise MEMS accelerometer for unattended ground sensor applications*. Unattended/Unmanned Ground, Ocean, and Air Sensor Technologies and Applications Vi, 2004. **5417**: p. 63-72.
149. Scarborough, W.R. and S.A. Talbot, *Proposals for Ballistocardiographic Nomenclature and Conventions - Revised and Extended - Report of Committee on Ballistocardiographic Terminology*. Circulation, 1956. **14**(3): p. 435-450.
150. Vogt, E., D. MacQuarrie, and J.P. Neary, *Using ballistocardiography to measure cardiac performance: a brief review of its history and future significance*. Clinical Physiology and Functional Imaging, 2012. **32**(6): p. 415-420.
151. Starr, I., et al., *Studies on the estimation of cardiac output in man, and of abnormalities in cardiac function, from the heart's recoil and the blood's impacts; The ballistocardiogram*. American Journal of Physiology, 1939. **127**(1): p. 1-28.
152. Junnila, S., A. Akhbardeh, and A. Varri, *An Electromechanical Film Sensor Based Wireless Ballistocardiographic Chair: Implementation and Performance*. Journal of Signal Processing Systems for Signal Image and Video Technology, 2009. **57**(3): p. 305-320.
153. Inan, O.T., et al., *Robust ballistocardiogram acquisition for home monitoring*. Physiological Measurement, 2009. **30**(2): p. 169-185.

154. Hu, Y.T. and Y. Xu, *An Ultra-Sensitive Wearable Accelerometer for Continuous Heart and Lung Sound Monitoring*. 2012 Annual International Conference of the Ieee Engineering in Medicine and Biology Society (Embc), 2012: p. 694-697.
155. Wang, Z. and Y. Xu, *Vibration energy harvesting device based on air-spaced piezoelectric cantilevers*. Applied Physics Letters, 2007. **90**(26).
156. He, X. and S.O. Oyadiji, *Influence of adhesive characteristics on the transverse free vibration of single lap jointed cantilevered beams*. Journal of Materials Processing Technology, 2001. **119**(1-3): p. 366-373.
157. Barzilai, A., T. VanZandt, and T. Kenny, *Technique for measurement of the noise of a sensor in the presence of large background signals*. Review of Scientific Instruments, 1998. **69**(7): p. 2767-2772.
158. Inan, O.T., *Recent Advances in Cardiovascular Monitoring Using Ballistocardiography*. 2012 Annual International Conference of the Ieee Engineering in Medicine and Biology Society (Embc), 2012: p. 5038-5041.
159. Dock, W., *Ballistocardiography*. Lancet, 1976. **1**(7963): p. 809-809.
160. Alametsa, J., A. Palomaki, and J. Viik, *Short and longer term repeatability of ballistocardiography in a sitting position with EMFi sensor*. Medical & Biological Engineering & Computing, 2011. **49**(8): p. 881-889.
161. Trefny, Z.M., et al., *Quantitative Ballistocardiography (Q-BCG) for Measurement of Cardiovascular Dynamics*. Physiological Research, 2011. **60**(4): p. 617-625.
162. Ferrari, M., et al., *Piezoelectric multifrequency energy converter for power harvesting in autonomous microsystems*. Sensors and Actuators A-Physical, 2008. **142**(1): p. 329-335.

163. Sari, I., T. Balkan, and H. Kulah, *An electromagnetic micro power generator for wideband environmental vibrations*. Sensors and Actuators A: Physical, 2008. **145–146(0)**: p. 405-413.
164. Xue, H.A., Y.T. Hu, and Q.M. Wang, *Broadband piezoelectric energy harvesting devices using multiple bimorphs with different operating frequencies*. IEEE Transactions on Ultrasonics Ferroelectrics and Frequency Control, 2008. **55(9)**: p. 2104-2108.
165. Roundy, S., et al., *Improving power output for vibration-based energy scavengers*. IEEE Pervasive Computing, 2005. **4(1)**: p. 28-36.
166. Leland, E.S. and P.K. Wright, *Resonance tuning of piezoelectric vibration energy scavenging generators using compressive axial preload*. Smart Materials & Structures, 2006. **15(5)**: p. 1413-1420.
167. Eichhorn, C., F. Goldschmidtboeing, and P. Woias, *Bidirectional frequency tuning of a piezoelectric energy converter based on a cantilever beam*. Journal of Micromechanics and Microengineering, 2009. **19(9)**.
168. Wu, X., et al. *A frequency adjustable vibration energy harvester*. in *Proceedings of the Power MEMS Conference*. 2008. Sendai, Japan.
169. Lallart, M., S.R. Anton, and D.J. Inman, *Frequency Self-tuning Scheme for Broadband Vibration Energy Harvesting*. Journal of Intelligent Material Systems and Structures, 2010. **21(9)**: p. 897-906.
170. Challa, V.R., M.G. Prasad, and F.T. Fisher, *Towards an autonomous self-tuning vibration energy harvesting device for wireless sensor network applications*. Smart Materials & Structures, 2011. **20(2)**.

171. Hajati, A. and S.G. Kim, *Ultra-wide bandwidth piezoelectric energy harvesting*. Applied Physics Letters, 2011. **99**(8).
172. Erturk, A., J. Hoffmann, and D.J. Inman, *A piezomagnetoelastic structure for broadband vibration energy harvesting*. Applied Physics Letters, 2009. **94**(25).
173. Sebald, G., et al., *Experimental Duffing oscillator for broadband piezoelectric energy harvesting*. Smart Materials & Structures, 2011. **20**(10).
174. Ferrari, M., et al., *Improved Energy Harvesting from Wideband Vibrations by Nonlinear Piezoelectric Converters*. Procedia Chemistry, 2009. **1**(1): p. 1203-1206.
175. Jung, S.M. and K.S. Yun, *Energy-harvesting device with mechanical frequency-up conversion mechanism for increased power efficiency and wideband operation*. Applied Physics Letters, 2010. **96**(11).
176. Berdy, D.F., et al. *Increased-bandwidth, meandering vibration energy harvester*. in *2011 16th International Solid-State Sensors, Actuators and Microsystems Conference, TRANSDUCERS'11, June 5, 2011 - June 9, 2011*. 2011. Beijing, China: IEEE Computer Society.
177. Berdy, D.F., et al., *Wide-bandwidth, meandering vibration energy harvester with distributed circuit board inertial mass*. Sensors and Actuators a-Physical, 2012. **188**: p. 148-157.
178. Zhou, W.L., G.R. Penamalli, and L. Zuo, *An efficient vibration energy harvester with a multi-mode dynamic magnifier*. Smart Materials & Structures, 2012. **21**(1).
179. Lee, S., B.D. Youn, and B.C. Jung, *Robust segment-type energy harvester and its application to a wireless sensor*. Smart Materials and Structures, 2009. **18**(9).

180. Kim, J.E. and Y.Y. Kim, *Power enhancing by reversing mode sequence in tuned mass-spring unit attached vibration energy harvester*. AIP Advances, 2013. **3**(7): p. -.
181. Wu, H., et al., *A novel two-degrees-of-freedom piezoelectric energy harvester*. Journal of Intelligent Material Systems and Structures, 2012.
182. Wang, Z. and Y. Xu, *Vibration energy harvesting device based on air-spaced piezoelectric cantilevers*. Applied Physics Letters, 2007. **90**(26): p. 263512.
183. Li, Y., et al., *Micromachined piezoresistive accelerometers based on an asymmetrically gapped cantilever*. Journal of Microelectromechanical Systems, 2011. **20**(1): p. 83 - 94

ABSTRACT

HIGH-PERFORMANCE ACCELEROMETER BASED ON ASYMMETRIC-GAPPED CANTILEVERS FOR PHYSIOLOGICAL ACOUSTIC SENSING

by

YATING HU

August 2014

Advisor: Dr. Yong Xu

Major: Electrical Engineering

Degree: Doctor of Philosophy

Continuous or mobile monitoring of physiological sounds is expected to play important role in the emerging mobile healthcare field. Because of the miniature size, low cost, and easy installation, accelerometer is an excellent choice for continuous physiological acoustic signal monitoring. However, in order to capture the detailed information in the physiological signals for clinical diagnostic purpose, there are more demanding requirements on the sensitivity/noise performance of accelerometers. In this thesis, a unique piezoelectric accelerometer based on the asymmetric-gapped cantilever which exhibits significantly improved sensitivity is extensively studied. A meso-scale prototype is developed for capturing the high quality cardio and respiratory sounds on healthy people as well as on heart failure patients. A cascaded gapped cantilever based accelerometer is also explored for low frequency vibration sensing applications such as ballistocardiogram monitoring. Finally, to address the power issues of wireless sensors such as wireless wearable health monitors, a wide band vibration energy harvester based on a folded gapped cantilever is developed and demonstrated on a ceiling air condition unit.

AUTOBIOGRAPHICAL STATEMENT

YATING HU

Education

- Sep. 2008 ~ May. 2014 (expected), **Ph.D.**, Department of Electrical and Computer Engineering, Wayne State University, Detroit, MI, USA
- Sep. 2008 ~ May. 2011, **M.S.**, Department of Electrical and Computer Engineering, Wayne State University, Detroit, MI, USA

Publications

1. **Yating Hu**, et al., *A wide-band vibration energy harvester based on a folded asymmetric-gapped cantilever*, Applied Physics Letters 2014. 104: 053902
2. Yuefa Li, Qinglong Zheng, **Yating Hu**, et al., *Micromachined Piezoresistive Accelerometers Based on an Asymmetrically Gapped Cantilever*, Journal of Microelectromechanical Systems, 2011. 20(1): p.83-94.
3. **Yating Hu**, et al., *Bio-inspired 3-D Tactile Sensor for Minimally Invasive Surgery*, Journal of Microelectromechanical Systems, 2010. 19(6): p.1400-1408.
4. **Yating Hu** et al., *An Ultra-Sensitive Wearable Accelerometer for Continuous Heart and Lung Sound Monitoring*, 34th Annual International Conference of the IEEE Engineering in Medicine and Biology Society (EMBC'12), San Diego, California, USA, 2012.